

EFFECTS OF MULTI-ELECTRON CORRELATION ON
MULTIPHOTON IONIZATION AND HIGH-ORDER
HARMONIC GENERATION OF ATOMIC AND
MOLECULAR SYSTEMS IN INTENSE ULTRASHORT
LASER FIELDS

By

John Thomas Heslar

B.S. Chemistry

Northeastern State University 2001

Submitted to the Department of Chemistry and the Faculty of
Graduate School of the University of Kansas in partial fulfillment of
the requirements for the Degree of Doctor of Philosophy

Advisor:

Shih-I Chu

Committee members:

Thomas E. Cravens

Peter M. Hierl

Krzysztof Kuczera

Weizhang Huang

Date defended: May 2009

The Dissertation Committee for John Thomas Heslar certifies
that this is the approved version of the following dissertation:

EFFECTS OF MULTI-ELECTRON CORRELATION ON
MULTIPHOTON IONIZATION AND HIGH-ORDER
HARMONIC GENERATION OF ATOMIC AND
MOLECULAR SYSTEMS IN INTENSE ULTRASHORT
LASER FIELDS

Chairperson

Shih-I Chu

Committee:

Thomas E. Cravens

Peter M. Hierl

Krzysztof Kuczero

Weizhang Huang

Dated approved: May 2009

To the Loving Memory of Edward Ray Heslar

Table of Contents

Table of Contents	iv
List of Tables	vi
List of Figures	viii
Abstract	x
Acknowledgements	xiii
Introduction	1
1 Generalized Pseudospectral Method (GPS) for Bound and Resonance State Problems in Two-Centered Molecular Systems	7
1.1 Introduction	7
1.2 The Generalized Pseudospectral (GPS) Method for Bound State Eigenvalue Problems	9
1.3 Two-Centered Generalized Pseudospectral Method (GPS) for Molecular Systems	11
1.4 Conclusion	22
2 Time-Dependent Density-Functional Theory (TDDFT) for Molecular Processes in Strong Fields	23
2.1 Introduction	23
2.2 Time-Dependent Generalized Pseudospectral Method for Numerical Solution of TDDFT Equations	25
2.3 TDDFT Method for Diatomic Molecules	28
2.4 Dirichlet Boundary Conditions for the Hartree Potential in DFT Formalism	31

2.5	TDDFT for Intense-Field Multiphoton Processes	33
2.6	Conclusion	39
3	High-Order Harmonic Generation of Heteronuclear Diatomic Molecules in Intense Ultrashort Laser Fields: An All-Electron TDDFT Study	40
3.1	Introduction	40
3.2	Multiphoton Ionization of N ₂ and CO in Intense Laser Fields	42
3.3	Multielectron Effects in HHG Spectra of Diatomic Molecules	51
3.4	Conclusion	58
4	Ab Initio Study of High-Lying Doubly Excited States of Helium in Static Electric Fields	63
4.1	Introduction	63
4.2	Complex-Scaling Generalized Pseudospectral Method in Hyperspherical Coordinates	65
4.3	Determination of the Doubly Excited Autoionizing Resonances	72
4.4	Determination of the DC Field Effects on the Doubly Excited Resonance States	74
4.5	Conclusion	76
5	Ab Initio 6D Treatment of the Time-Evolution Dynamics for Two-Electron Systems in Few-Cycle XUV Laser Pulses	89
5.1	Introduction	89
5.2	Generalized Pseudospectral Method in Hyperspherical Coordinates	92
5.3	Time-Dependent Generalized Pseudospectral Approach in Hyperspherical Coordinates	102
5.4	Conclusion	112
	Bibliography	114

List of Tables

3.1	Comparison of the field-free molecular orbital energy levels of CO and N ₂ , calculated with the LB α potential, and the experimental ionization potentials (in a.u.).	43
3.2	HOMO energies of N ₂ and CO molecules in DC electric field (positive field direction is from C to O)	51
4.1	Energies and widths for doubly excited Rydberg states $^1S^e(2, n, (a, b))$ below the $N = 2$ threshold (in a.u.). Numbers in square brackets indicate powers of ten.	79
4.2	Energies and widths for doubly excited Rydberg states $^1P^o(2, n, (a, b, c))$ below the $N = 2$ threshold (in a.u.). Numbers in square brackets indicate powers of ten.	80
4.3	Energies and widths for doubly excited Rydberg states $^1D^e(2, n, (a, b, c))$ below the $N = 2$ threshold (in a.u.). Numbers in square brackets indicate powers of ten.	81
4.4	Energies and widths for doubly excited Rydberg states $^1F^o(2, n, (a, b, c))$ below the $N = 2$ threshold (in a.u.). Numbers in square brackets indicate powers of ten.	82
4.5	Field-perturbed resonant energies E_r and widths (in a.u.) for the $^1S^e$ $n = 10 - 20$ doubly excited Rydberg states below the $N=2$ threshold. Numbers in square brackets indicate powers of ten.	83

4.6	Field-perturbed resonant energies E_r and widths (in a.u.) for the $^1P^o$ $n = 10 - 20$ doubly excited Rydberg states below the $N=2$ threshold. Numbers in square brackets indicate powers of ten.	84
4.7	(continued) Field-perturbed resonant energies E_r and widths (in a.u.) for the $^1P^o$ $n = 10 - 20$ doubly excited Rydberg states below the $N=2$ threshold. Numbers in square brackets indicate powers of ten.	85
4.8	Field-perturbed resonant energies E_r and widths (in a.u.) for the $^1D^e$ $n = 10 - 20$ doubly excited Rydberg states below the $N=2$ threshold. Numbers in square brackets indicate powers of ten.	86
4.9	(continued) Field-perturbed resonant energies E_r and widths (in a.u.) for the $^1D^e$ $n = 10 - 20$ doubly excited Rydberg states below the $N=2$ threshold. Numbers in square brackets indicate powers of ten.	87
4.10	Given are resonant energies E_r and widths (in a.u.) for the $n = 10 - 20$ doubly excited Rydberg states below the $N=2$ threshold in a dc field of 84.4 kV/cm . Numbers in square brackets indicate powers of ten. $n(a, b)^*$ indicates the comparison with Mihelić and Žitnik [44].	88
5.1	Energies of the ground and low-lying excited states of the helium atom. No effect of finite nuclear mass is included in the present and literature values. All energies are given in a.u.	100
5.2	Comparison of the radial expectation and oscillator strengths of the helium atom. No effect of finite nuclear mass is included. All energies are given in a.u.	101

List of Figures

1.1	A typical grid structure of the spatial coordinates of a diatomic molecule obtained by the generalized pseudospectral (GPS) discretization technique.	13
2.1	Dirichlet boundary conditions for the Hartree potential (a) interior portion of the Hartree potential (b) boundary condition for the Hartree potential at $x = +1$ or $\xi = R_{max}$	32
3.1	Molecular orbital binding energies and orbital structures for N_2 and CO molecules.	47
3.2	The time-dependent population of electrons in different spin orbital's of CO and N_2 in 800 nm, \sin^2 pulse laser field, with 20 optical cycles in pulse duration. N_2 molecule (a) 5×10^{13} W/cm ² , (b) 1×10^{14} W/cm ² , CO molecule (c) 5×10^{13} W/cm ² , (d) 1×10^{14} W/cm ²	49
3.3	Comparison of the HHG power spectra of CO and N_2 , in 800 nm, 5×10^{13} W/cm ² \sin^2 pulse laser field.	52
3.4	Comparison of the HHG power spectra of CO and N_2 , in 800 nm, 1×10^{14} W/cm ² \sin^2 pulse laser field.	53
3.5	Time profiles for (a) N_2 and (b) CO. Laser intensity used is 5×10^{13} W/cm ² , wavelength used is 800 nm, with 20 optical cycles in pulse duration.	54

3.6	Individual orbital and total high-order harmonic generation power spectra of CO at the peak intensity 1×10^{14} W/cm ² with a laser frequency of 800 nm.	55
3.7	Orbital dipole moments of CO at the peak intensity 1×10^{14} W/cm ² with a laser frequency of 800 nm for 3 optical cycles (10 – 13). . . .	57
3.8	Orbital dipole moments (total, $3\sigma_g$, and $2\sigma_u$) of N ₂ at the peak intensity 1×10^{14} W/cm ² with a laser frequency of 800 nm for 20 optical cycles.	60
3.9	Individual and total orbital high-order harmonic generation power spectra of N ₂ at the peak intensity 1×10^{14} W/cm ² with a laser frequency of 800 nm.	61
3.10	Individual and orbital interference power spectra of N ₂ at the peak intensity 1×10^{14} W/cm ² with a laser frequency of 800 nm.	62
4.1	Potential curves of the helium atom for (a) $^1S^e$, (b) $^1P^o$, (c) $^1D^e$, and (d) $^1F^o$ manifolds.	71
4.2	Field-free energies and widths of doubly excited Rydberg states as a function of the principle quantum number n , in the energy region below the $N = 2$ threshold for different symmetries: (a) $^1S^e$ ($2, na$), (b) $^1S^e$ ($2, nb$), (c) $^1P^o$ ($2, na$), (d) $^1P^o$ ($2, nb$), (e) $^1D^e$ ($2, na$), and (f) $^1D^e$ ($2, nb$).	78
5.1	The time-dependent population of He in 800 nm, 1×10^{14} W/cm ² sin ² pulse laser field with 10 optical cycles in pulse duration.	108
5.2	The time-dependent survival probability of He (ground-state $1s^2$) in 800 nm, 1×10^{14} W/cm ² sin ² pulse laser field with 10 optical cycles in pulse duration.	109
5.3	The induced dipole moment of He in 800 nm, 1×10^{14} W/cm ² sin ² pulse laser field with 10 optical cycles in pulse duration.	110
5.4	Harmonic generation of He in 800 nm, 1×10^{14} W/cm ² sin ² pulse laser field with 10 optical cycles in pulse duration.	111

Abstract

The study of the electron correlation and quantum dynamics of many-electron atoms and molecules in the presence of intense external fields is a subject of much current importance in science and technology. While experimental breakthroughs constantly challenge theorists, the reverse is also true, with theorists suggesting new experimental paths and novel ways to reach exciting regimes where new physics can be explored. For example, we have recently developed *ab initio* methods and applications to study time dependent quantum dynamics of atoms and molecules which cannot be understood by traditional perturbation theories. Moreover, currently there exist no adequate methods capable of studying the dynamical role of the *individual* valence electron to the high-order harmonic generation (HHG) and multiphoton ionization (MPI) processes in strong fields. Such a study can provide insights regarding the detailed quantum dynamics and HHG mechanisms, as well as the optimal control of strong-field processes. To advance this strong-field atomic and molecular physics, this dissertation aims at the developing new theoretical formalisms and accurate computational methods for *ab initio* non-perturbative studies of atomic and molecular processes in intense laser fields. The new methods developed allow in-depth and precision studies of strong-field phenomena for multielectron systems.

In this dissertation we investigate the role of electron correlation in dynamics of multielectron systems subject to strong fields. We present a time-dependent density functional theory (TDDFT), with proper asymptotic long-range potential, for non-perturbative treatment of multiphoton processes of homonuclear and heteronuclear diatomic molecules in intense ultrashort laser fields. *A time-dependent two-center*

generalized pseudospectral method is presented for accurate and efficient treatment of the TDDFT equations in space and time. The procedure allows nonuniform and optimal spatial grid discretization of the Hamiltonian in prolate spheroidal coordinates and a split-operator scheme in the *energy representation* is extended for the time propagation of the individual molecular spin-orbital. The theory is applied to a detailed *all-electron* study of multiphoton ionization (MPI) and high-order harmonic generation (HHG) processes of N_2 and CO molecules in intense laser pulses. The results reveal intriguing and substantially different nonlinear optical response behaviors for N_2 and CO, despite the fact that CO has only a very small permanent dipole moment. In particular, we found that the MPI rate for CO is higher than that of N_2 . Furthermore, while laser excitation of the homonuclear N_2 molecule can generate only odd harmonics, both even and odd harmonics can be produced from the heteronuclear CO molecule.

Next, we present a complex-scaling (CS)-generalized pseudospectral (GPS) method in hyperspherical coordinates (HSC) for an accurate *ab initio* and accurate treatment of the electron structure and quantum dynamics of two-electron systems. The six-dimensional coupled hyperspherical adiabatic-channel equations are discretized and solved efficiently and accurately by means of the GPS method. The GPS method allows non-uniform and optimal spatial discretization of the two-electron Hamiltonian in HSC with the use of only a very modest number of grid points. The procedure is applied for the precision calculation of the energies and widths of doubly-excited Rydberg resonance states as well as the ionization rates of He atoms in an external electric field.

Lastly, we present a time-dependent generalized pseudospectral (TDGPS) approach in hyperspherical coordinates for fully *ab initio* nonperturbative treatment of multiphoton dynamics of atomic systems in intense laser fields. The laser-driven two-electron system is described by hyperspherical close coupling scheme. A novel 6D coupled *time-dependent generalized pseudospectral method* approach in *hyperspherical coordinates* are developed for single or double ionization without the use of the

conventional adiabatic channels.

In conclusion, the present dissertation provides new developments in both theoretical and computational techniques, as well as advancements in the essential understanding of strong-field atomic and molecular physics.

Acknowledgements

I would like to thank Prof. Shih-I Chu, my supervisor, for his guidance, constant support during my research and above all, his patience. I am also very thankful to Dr. Dmitry A. Telnov, Dr. Xiao-Min Tong, Dr. Zhongyuan Zhou, Dr. Juan Carrera and Sang-Kil Son for their constant, helpful, friendly support and encouragement during my studies at KU.

Of course, I am grateful to my family, my mother Mollie Heslar, and my father Edward Heslar for their patience, guidance, and *love*. They were the best parents a kid could ever wish for and they always let me make my own decisions (with a lot of guidance and support) in what the future would bring for me. Without them I never would have learned how to be a better person in life and this work would never have come into existence. Also, I am grateful to almost like family, my close friends that have went through the struggle with me, and have always been there for me, Michael Hale, Kristie Hale, Jim Hale, Bobbi Hale, Michael Santilli, Ryan Conley, and Nicky Hung.

Lawrence, Kansas
May 6, 2009

John Thomas Heslar

Introduction

Atomic, molecular, and optical (AMO) science demonstrates powerfully the ties of fundamental physics and chemistry to society. Its very name reflects three of 20th century physics' greatest advances: the establishment of the atom as a building block of matter; the development of quantum mechanics, which made it possible to understand the inner workings of atoms and molecules; and the invention of the laser, which changed everything from the way we think about light to the way we store and communicate information. The field encompasses the study of atoms, molecules, and light, including the discovery of related applications and techniques.

Recently we begin to observe the processes of nature as they play out over times shorter than a millionth of a billionth of a second (less than 1 femtosecond—that is, in the attosecond regime). This remarkable new capability is enabled by advances in ultrafast laser- and accelerator-based x-ray strobes, which can detect the motion of electrons in atoms and molecules. It will become also feasible to control physical phenomena on all of the timescales relevant to atomic and molecular physics, chemistry, biology, and materials science. These previously unavailable tools of quantum

control could help tailor new molecules for applications in health care, energy, and security.

New 21st-century tools also place us on the verge of the new discipline of quantum control. This development is enabled by key advances in laser technology, which let us generate light pulses whose shape, intensity, and color can be programmed with unprecedented flexibility. Our ability to control the positions, velocities, and relative spatial orientations of individual atoms and molecules has led to a broad array of precision measurement technologies and devices, leading to a wide range of experiments that reveal qualitatively new phenomena. A new capability to manipulate the inner workings of molecules is emerging: Lasers can now be used to control the outcome of selected chemical reactions. This control technology may ultimately lead to powerful tools for creating new molecules and materials tailored for applications in health care, nanoscience, environmental science, energy, and national security.

AMO experiments have reached such high levels of sophistication, precision, and accuracy that they are uniquely positioned to carry out the most demanding tests ever conducted of some of the most fundamental laws of nature. The grand challenge for theoretical chemist is to develop more rigorous approaches for probing atomic and molecular physics in strong fields to explain current experimental observations. Without the development, application and challenge of new theoretical ideas, atomic and molecular physics will eventually be reduced to a description of experimental

observations of physical events, supported only because of its intimate connections to technology.

The study of atomic and molecular processes in intense ultrashort laser fields is a subject of much current interest in science and technology. In particular, high-order harmonic generation (HHG) is one of the hottest topics in strong-field atomic and molecular physics today. To describe such strong-field processes using fully *ab initio* wave-function approach, it is necessary to solve the $(3n + 1)$ dimensional time-dependent Schrodinger equation (TDSE) in space and time, where n is the number of electrons. Today's computers are doubling in performance every year or two, but this is well beyond the capability of current supercomputer technology when $n > 2$. Even for the two-electron ($n = 2$) case, high-precision fully *ab initio* 6D study of the HHG of the He atoms was achieved only very recently. Due to the complexity of many-body processes in intense laser fields, most theoretical approaches in the past two decades adopt various approximations such as ADK (Ammosov-Delone-Krainov) model [68], strong field approximations [45], and single-active-electron (SAE) [37], which do not take into the account the detailed electron structure and electron correlation. Although such models may provide qualitative information in weak laser fields, their predictions are not reliable in stronger fields as seen in a number of recent experiments. In this thesis, we explore in great detail the development of fully *ab initio* and other more rigorous methods for investigation of atomic and molecular

physics in intense laser fields. For many-electron molecular ($n \geq 2$) systems, we have performed *self-interaction-free* time-dependent density functional theory (TDDFT) calculations for the non-perturbative treatment of multiphoton ionization (MPI) and HHG processes of heteronuclear and homonuclear diatomic molecules in intense laser fields. Here, we extend the TDDFT, with proper long range potentials, to the study of multi-electron heteronuclear and homonuclear diatomic molecules (N_2 and CO in particular) with an aim to explore the dynamical role and nonlinear response of individual electron spin orbital as well as the effect of asymmetry of the molecules to intense laser pulse fields, a subject of largely unexplored area of intense field AMO physics.

The major problem with DFT is that the exact functionals for exchange and correlation are not known except for the free electron gas, and must be approximated for the total energy functional. Development of fully *ab initio* methods is needed to describe the exchange and correlation energies exactly, without the use of DFT. Using the GPS method with our refined DFT approach, we can predict ionization potentials well within 3 to 5 % of experimental values [30]. New fully *ab initio* methods mean now we can have more accurate or nearly exact treatment of electron correlation of many-electron quantum systems in time-dependent fields which will be able to reproduce experimental values, where the exchange and correlation can be taken into account exactly.

Therefore, we have developed a fully *ab initio* wave function approach for non-perturbative treatment of two-electron atomic systems in static laser fields. The method is based on the extension of the TDGPS method to the three-body quantum systems in hyperspherical coordinates (HSC). Numerous theoretical investigations have improved our understanding of the e-e correlation and the determination of the autoionizing resonances of the double excited states of He in the last few decades [55]. In addition to fundamental interest, the energies, lifetimes, and oscillator strengths of these doubly excited resonance states are also of significance in astrophysics and plasma physics [23]. More recently there is considerable interest in the study of the effect of static electric fields on doubly excited states of helium atoms below $N = 2$ threshold [21, 22, 20, 51, 77, 44]. To advance this field, we present a new computational method, the complex-scaling generalized pseudospectral (CSGPS) method in hyperspherical coordinates (HSC), for efficient and accurate non-perturbative calculation of high-lying doubly excited states of He in the presence of weak and strong dc electric fields below $N = 2$ threshold. Comparison with available experimental data is made. In addition, we also present the energies and widths of field-free doubly excited resonance states of He for n up to 20 for the first time.

Even for the simplest two-electron atomic system, non-perturbative treatment for the single or double ionization also presents both practical and formal difficulties. A 6D coupled *time-dependent generalized pseudospectral* approach in *hyperspherical*

coordinates is developed for the ionization of helium without use of conventional adiabatic channels. This new method helps us understand the double ionization mechanism and explain experimental observations from an *ab initio* point of view. Also, due to the short time duration of the xuv pulses, the detailed theoretical description for this ionization process requires us to develop a fully *ab initio* time-dependent approach. In this work, we will present a TDGPS representation of the hyperspherical coordinates technique, in which most physics in the single and double photoionization can be comprehensively explored.

Our predicted results are in good agreement with available experimental data, providing new physical insights regarding the effect of electron correlation on multiphoton dynamics. However, much still remains to be explored, particularly fully *ab initio* 6D calculation of the H_2 molecule with use of our hyperspherical coordinates and polyatomic molecular systems with use of DFT and our generalized pseudospectral method. Further development of the TDGPS algorithm or other new algorithms for the treatment of *multi-center* molecular dynamics in intense laser fields, with optimal and *nonuniform* spatial grid discretization around each nuclear center, is the next challenge. Once this bottleneck can be resolved, it will open up a whole range of exciting highly nonlinear optical new phenomena and attosecond strong-field AMO processes to be explored.

Chapter 1

Generalized Pseudospectral Method (GPS) for Bound and Resonance State Problems in Two-Centered Molecular Systems

1.1 Introduction

For atomic and molecular structure calculations involving the Coulomb potential, one typical problem associated with commonly used equal-spacing grid methods is the Coulomb singularity at $r = 0$ and the longrange nature of the potential. Generally one truncates the semi-infinite $(0, \infty)$ domain into finite domain $[rmin, rmax]$ to avoid the Coulomb singularity at the origin and the infinite domain. For this purpose, $rmin$ must be chosen sufficiently small and $rmax$ sufficiently large. This results in the need of a large number of grid points. Further, extreme care must be exercised to ensure the wave functions obtained from such discretization is of sufficient accuracy for

performing reliable high-order harmonic generation calculations. The first step is to map the semi-infinite domain $[0, \infty]$ or $[0, rmax]$ into the finite domain $[-1, 1]$ using a non-linear mapping $r = r(x)$, followed by the Legendre pseudospectral discretization. This allows for denser grids near the origin, leading to more accurate eigenvalues and eigenfunctions and the use of a considerably smaller number of grid points than those of the equal-spacing grid methods.

Here we extend a generalized pseudospectral (GPS) method for optimal discretization of the radial and angular coordinates to overcome some of the above mentioned problems. The GPS method has been recently applied to the study of heteronuclear diatomic molecules in intense laser fields [30].

We present a new two-center generalized pseudospectral method for numerical integration of the Schrödinger equation which is computationally efficient and capable of providing more accurate solutions to the wave function for reliable study of multiphoton processes in molecular systems. A detailed derivation of the GPS method, molecular Hamiltonian and molecular Schrödinger equation is given in prolate spheroidal coordinates.

1.2 The Generalized Pseudospectral (GPS) Method for Bound State Eigenvalue Problems

The central part of the pseudospectral method is to approximate the exact function $f(x)$ defined on the interval $[-1, 1]$ by N th-order polynomial $f_N(x)$,

$$f(x) \cong f_N(x) = \sum_{i=0}^N f(x_i)g_i(x), \quad (1.2.1)$$

and requires the approximation to be *exact* at the *mesh points* x_i :

$$f_N(x_i) = f(x_i). \quad (1.2.2)$$

In the case of the Legendre pseudospectral method which will be employed here, $x_0 = -1$, $x_N = 1$, and x_i (for $i = 1, \dots, N-1$) are the mesh points determined by the roots of the first derivative of the Legendre polynomial $P_N(x)$ with respect to x , namely,

$$P'_N(x_i) = 0. \quad (1.2.3)$$

In Eq. (1.2.1), $g_i(x)$ are the cardinal functions defined by

$$g_i(x) = -\frac{1}{N(N+1)P_N(x_i)} \frac{(1-x^2)P'_N(x)}{x-x_i} \quad (1.2.4)$$

and which satisfy the unique property

$$g_i(x_{i'}) = \delta_{i'i}. \quad (1.2.5)$$

Consider the 1D eigenvalue problem for the radial Shrödinger equation [60, 8, 4, 5] defined on the semi-infinite axis $[0, \infty]$ with Dirichlet boundary conditions:

$$\hat{H}(r)\psi(r) = E\psi(r), \quad \psi(0) = \psi(\infty) = 0, \quad (1.2.6)$$

where

$$\hat{H}(r) = -\frac{1}{2} \frac{d^2}{dr^2} + V(r). \quad (1.2.7)$$

For atomic and molecular structure and dynamics calculations involving the Coulomb potential, one major problem with the grid methods is the Coulomb singularity at $r = 0$ and the long-range nature of the interaction. Here, we map the semi-infinite domain $r \in [0, \infty]$ into the finite domain $x \in [-1, 1]$ using the mapping transformation

$$r = r(x), \quad (1.2.8)$$

and then use the Legendre pseudospectral discretization techniques. Then the following algebraic mapping:

$$r = r(x) = L \frac{1+x}{1-x+\alpha}, \quad (1.2.9)$$

where L is the mapping parameter. Generally the introduction of nonlinear mapping can lead to an asymmetric or a generalized eigenvalue problem. Such undesirable

features can be avoided by the following symmetrization procedure. Thus by introducing

$$\psi(r(x)) = \sqrt{r'(x)}f(x), \quad (1.2.10)$$

we obtain the following transformed Hamiltonian, leading to a *symmetric* eigenvalue problem (in atomic units):

$$\hat{H}(x) = -\frac{1}{2} \frac{1}{r'(x)} \frac{d^2}{dx^2} \frac{1}{r'(x)} + V(r(x)) \quad (1.2.11)$$

We next present a generalized pseudospectral method with prolate spheroidal coordinates for accurately calculating the bound and resonance states of diatomic molecules. This technique is based on the extension of the generalized pseudospectral method.

1.3 Two-Centered Generalized Pseudospectral Method (GPS) for Molecular Systems

To introduce the concept of a two-centered GPS method we show the simplest case, the field free one-electron Hamiltonian for the H_2^+ molecule, in atomic units, can be written as

$$\hat{H}_0 = -\frac{1}{2}\nabla^2 - \frac{Z_1}{|\mathbf{r} - \mathbf{R}_1|} - \frac{Z_2}{|\mathbf{r} - \mathbf{R}_2|} \quad (1.3.1)$$

where \mathbf{r} is the electronic coordinate, and $\mathbf{R}_1 = (0, 0, -a)$ and $\mathbf{R}_2 = (0, 0, b)$ are the

foci of the two nuclei in Cartesian coordinates. Z_1 and Z_2 are the effective charges of the nuclei. The internuclear separation R is equal to $(a + b)$. Now consider the bare electronic Hamiltonian in prolate spheroidal coordinates (ξ, η, ϕ) , $1 \leq \xi < \infty$, $-1 \leq \eta \leq 1$, $0 \leq \phi \leq 2\pi$, where x , y , and z are transformed from Cartesian coordinates to prolate spheroidal (shown in Fig. 1.1), namely,

$$x = \frac{(a+b)}{2} \sqrt{(\xi^2 - 1)(1 - \eta^2)} \cos \phi, \quad (1.3.2a)$$

$$y = \frac{(a+b)}{2} \sqrt{(\xi^2 - 1)(1 - \eta^2)} \sin \phi, \quad (1.3.2b)$$

$$z = \frac{(a+b)}{2} \xi \eta. \quad (1.3.2c)$$

Equation (1.3.1) can be recasted into the following form:

$$\hat{H}_0 = -\frac{1}{2a'^2} \frac{1}{(\xi^2 - \eta^2)} \left[\frac{\partial}{\partial \xi} (\xi^2 - 1) \frac{\partial}{\partial \xi} + \frac{\partial}{\partial \eta} (1 - \eta^2) \frac{\partial}{\partial \eta} + \frac{(\xi^2 - \eta^2)}{(\xi^2 - 1)(1 - \eta^2)} \frac{\partial^2}{\partial \phi^2} \right] - \frac{Z_1(\xi - \eta)}{a(\xi^2 - \eta^2)} - \frac{Z_2(\xi + \eta)}{a(\xi^2 - \eta^2)}, \quad (1.3.3)$$

where $a' = (a+b)/2$, and a and b are the two nuclei positions. Due to axial symmetry

of the system, the solutions of the static Shrödinger equation

$$\hat{H}\Psi = E\Psi, \quad (1.3.4)$$

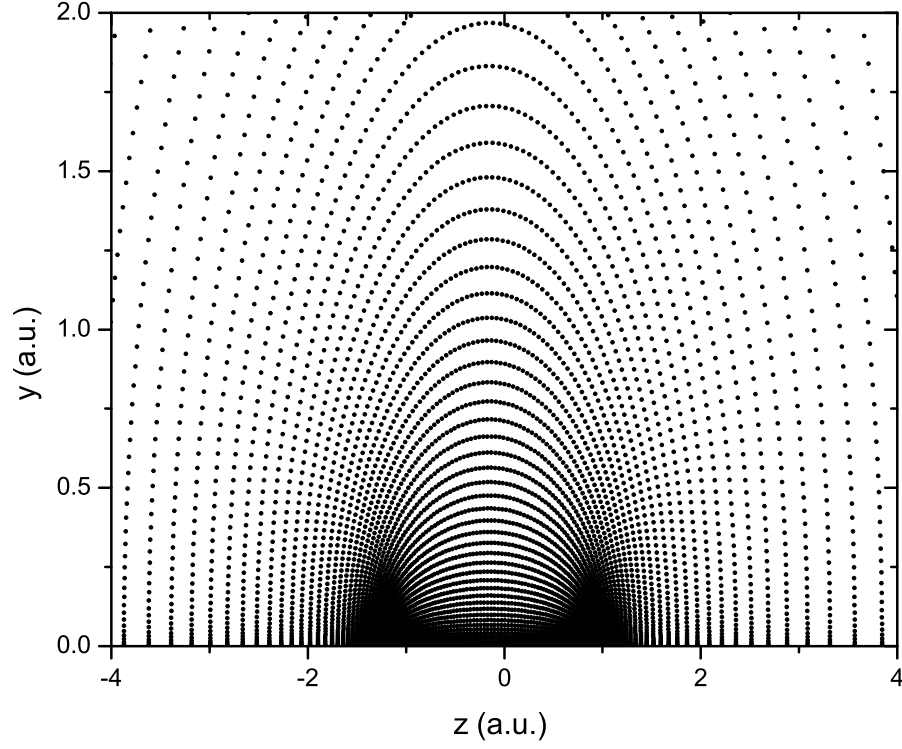


Figure 1.1: A typical grid structure of the spatial coordinates of a diatomic molecule obtained by the generalized pseudospectral (GPS) discretization technique.

take the form

$$\Psi(\xi, \eta, \varphi) = \Phi(\xi, \eta)e^{iM\varphi}, \quad (M = 0, \pm 1, \pm 2, \dots). \quad (1.3.5)$$

Because of the axial symmetry with respect to the z -axis, the projection M of the angular momentum on the z -axis is conserved.

In the pseudospectral method, we expand $\Phi(\xi, \eta)$ by $\Phi_{N_\xi, N_\eta}(\xi, \eta)$, the polynomials of order N_ξ and N_η in ξ and η , respectively,

$$\Phi(\xi, \eta) \simeq \Phi_{N_\xi, N_\eta}(\xi, \eta) = \sum_{i=0, j=0}^{N_\xi, N_\eta} \phi(\xi_i, \eta_j) g_i[x(\xi)] g_j[y(\eta)], \quad (1.3.6)$$

and further require the approximation to be exact, i.e., $\Phi_{N_\xi, N_\eta}(\xi_i, \eta_j) = \phi(\xi_i, \eta_j) \equiv \phi_{ij}$,

where $\{x(\xi_i)\}$ and $\{y(\eta_j)\}$ are the two sets of collocation points to be described below.

In Eq. (1.3.6), $g_i(x)$ and $g_j(y)$ are the cardinal functions [73, 76] defined as

$$g_i(x) = \frac{-1}{N_x(N_x + 1)P_{N_x}(x_i)} \cdot \frac{(1 - x^2)P'_{N_x}(x)}{x - x_i} \quad (1.3.7)$$

$$g_j(y) = \frac{-1}{N_y(N_y + 1)P_{N_y}(y_j)} \cdot \frac{(1 - y^2)P'_{N_y}(y)}{y - y_j} \quad (1.3.8)$$

In the case of the Legendre pseudospectral method [73, 76], which we will use throughout, the boundary points are $x_0 = y_0 = -1$ and $x_{N_\xi} = y_{N_\eta} = 1$. $x_i (i = 1, \dots, N_\xi - 1)$ and $y_j (j = 1, \dots, N_\eta - 1)$ are the collocation points determined, respectively, by the roots of the Legendre polynomial P_{N_ξ} with respect to x and P_{N_η} with respect to y , namely,

$$P_{N_\xi}(x_i) - P_{N_\xi+1}(x_i) = 0, \quad (1.3.9)$$

$$P_{N_\eta}(y_j) = 0. \quad (1.3.10)$$

It follows that the cardinal functions possess the following unique properties:

$$g_i(x_{i'}) = \delta_{i'i}, \quad (1.3.11)$$

$$g_j(y_{j'}) = \delta_{j'j}. \quad (1.3.12)$$

We shall use the following mapping transformations for the coordinates *pseudoradial* ξ and *pseudoangular* η :

$$\eta(y) = y, \quad -1 \leq y \leq 1, \quad (1.3.13)$$

$$\xi(x) = 1 + L \frac{1+x}{1-x+\alpha}, \quad -1 \leq x \leq 1, \quad (1.3.14)$$

$$\xi'(x) = \frac{d\xi}{dx} = 2L \frac{1+\alpha}{(1-x+\alpha)^2}, \quad (1.3.15)$$

L being the mapping parameter. The variables x and y are discretized using Legendre-Gauss-Radau for x_i and Legendre-Gauss scheme for y_j . The sets of collocation points are determined by Eqs. (1.3.9) and (1.3.10). Having constructed the mesh structure, we define a set of discrete weights

$$w_i^x = \frac{1}{(N_\xi + 1)^2} \frac{1+x_i}{[P_{N_\xi}(x_i)]^2}, \quad (1.3.16)$$

$$w_j^y = \frac{1}{(1-y_j^2)[P'_{N_\eta}(y_j)]^2}, \quad (1.3.17)$$

and a pair of discrete matrices d^x and d^y , which generate approximate integrals and partial derivatives on the mesh according to the relations (where F is a function of x and y):

$$\int_{-1}^1 F(x, y) dx = \sum_{i=1}^{N_x+1} w_i^x F(x_i, y), \quad (1.3.18)$$

$$\int_{-1}^1 F(x, y) dy = \sum_{j=1}^{N_y} w_j^y F(x, y_j), \quad (1.3.19)$$

$$\int_{-1}^1 \int_{-1}^1 F(x, y) dx dy = \sum_{i=1}^{N_x+1} \sum_{j=1}^{N_y} w_i^x w_j^y F_{ij}, \quad (1.3.20)$$

and

$$\frac{dF}{dx}(x_i, y) = \sum_{i'=1}^{N_x+1} D_{ii'}^x F(x_{i'}, y), \quad (1.3.21)$$

$$\frac{dF}{dy}(x, y_j) = \sum_{j'=1}^{N_y} D_{jj'}^y F(x, y_{j'}), \quad (1.3.22)$$

where

$$D_{ii'}^x = d_{ii'}^x \frac{(1 + x_{i'})P_{N_\xi}(x_i)}{(1 + x_i)P_{N_\xi}(x_{i'})}, \quad (1.3.23)$$

$$D_{jj'}^y = d_{jj'}^y \frac{P'_{N_\eta}(y_j)}{P'_{N_\eta}(y_{j'})}, \quad (1.3.24)$$

and the derivative matrices

$$d_{ii'}^x = \frac{1}{x_i - x_{i'}} (i \neq i'), \quad d_{ii}^x = \frac{1}{2(1 + x_i)}, \quad (1.3.25)$$

$$d_{N_\xi+1, N_\xi+1}^x = \frac{1}{4} N_\xi (N_\xi + 2),$$

$$d_{jj'}^y = \frac{1}{y_j - y_{j'}} (j \neq j'), \quad d_{jj}^y = \frac{y_j}{1 - y_j^2}. \quad (1.3.26)$$

Direct pseudospectral discretization of the Hamiltonian in Eq. (1.3.3) leads to an

asymmetric eigenvalue problem. To symmetrize the Hamiltonian discretization, we

consider the alternate but equivalent form of the Shrödinger equation

$$\frac{\delta \int d^3\mathbf{r} \psi^* (\hat{H} - E) \psi}{\delta \psi^*} = 0. \quad (1.3.27)$$

First, we will solve the unperturbed eigenvalue problem and obtain the eigenvalues and eigenfunctions:

$$\left[-\frac{1}{2}\nabla^2 + U(\xi, \eta)\right]\Psi(\xi, \eta, \varphi) = E\Psi(\xi, \eta, \varphi). \quad (1.3.28)$$

Here the kinetic energy operator in prolate spheroidal coordinates reads as:

$$-\frac{1}{2}\nabla^2 = -\frac{1}{2a'^2} \frac{1}{(\xi^2 - \eta^2)} \left[\frac{\partial}{\partial \xi} (\xi^2 - 1) \frac{\partial}{\partial \xi} + \frac{\partial}{\partial \eta} (1 - \eta^2) \frac{\partial}{\partial \eta} + \frac{(\xi^2 - \eta^2)}{(\xi^2 - 1)(1 - \eta^2)} \frac{\partial^2}{\partial \phi^2} \right], \quad (1.3.29)$$

and the coulomb interaction with the nuclei is as follows:

$$U(\xi, \eta) = -\frac{Z_1(\xi - \eta)}{a(\xi^2 - \eta^2)} - \frac{Z_2(\xi + \eta)}{a(\xi^2 - \eta^2)}. \quad (1.3.30)$$

The volume element:

$$dxdydz = a'^3(\xi^2 - \eta^2)d\xi d\eta d\phi. \quad (1.3.31)$$

Since the wave function $\Psi(\xi, \eta, \varphi)$ can be represented in separable form (Eq. 1.3.5),

and separate eigenvalue problems for different $|m|$ are obtained [58],

$$\begin{aligned} -\frac{1}{2a'^2} \frac{1}{(\xi^2 - \eta^2)} \left[\frac{\partial}{\partial \xi} (\xi^2 - 1) \frac{\partial}{\partial \xi} + \frac{\partial}{\partial \eta} (1 - \eta^2) \frac{\partial}{\partial \eta} - \frac{m^2}{\xi^2 - 1} - \frac{m^2}{1 - \eta^2} \right] \Phi_m \\ - \frac{Z_1(\xi - \eta)}{a(\xi^2 - \eta^2)} \Phi_m - \frac{Z_2(\xi + \eta)}{a(\xi^2 - \eta^2)} \Phi_m = E\Phi_m. \end{aligned} \quad (1.3.32)$$

To solve Eq. (1.3.32), we first convert to equivalent variational forms, different for

even and odd m . We have

$$\begin{aligned} \delta \left\{ \frac{1}{2a'^2} \int_1^\infty d\xi \int_{-1}^1 d\eta \left[(\xi^2 - 1) \frac{\partial \Phi_m^*}{\partial \xi} \frac{\partial \Phi_m}{\partial \xi} + (1 - \eta^2) \frac{\partial \Phi_m^*}{\partial \eta} \frac{\partial \Phi_m}{\partial \eta} \right. \right. \\ \left. \left. + \left(\frac{m^2}{\xi^2 - 1} + \frac{m^2}{1 - \eta^2} \right) \Phi_m^* \Phi_m \right] - \frac{1}{a'} \int_1^\infty d\xi \int_{-1}^1 d\eta (Z_1(\xi - \eta) + Z_2(\xi + \eta)) \Phi_m^* \Phi_m \right. \\ \left. - E \int_1^\infty d\xi \int_{-1}^1 d\eta (\xi^2 - \eta^2) \Phi_m^* \Phi_m \right\} = 0 \end{aligned} \quad (1.3.33)$$

for even $|m|$ and

$$\begin{aligned} \delta \left\{ -\frac{1}{a'} \int_1^\infty d\xi \int_{-1}^1 d\eta (Z_1(\xi - \eta) + Z_2(\xi + \eta)) \Phi_m^* \Phi_m + \frac{1}{2a'^2} \int_1^\infty d\xi \int_{-1}^1 d\eta \right. \\ \times \left[\frac{(\xi^2 - 1)^2}{\xi^2} \frac{\partial}{\partial \xi} \left(\frac{\xi}{\sqrt{\xi^2 - 1}} \Phi_m^* \right) \frac{\partial}{\partial \xi} \left(\frac{\xi}{\sqrt{\xi^2 - 1}} \Phi_m \right) \right. \\ \left. + (1 - \eta^2)^2 \frac{\partial}{\partial \eta} \left(\frac{1}{\sqrt{1 - \eta^2}} \Phi_m^* \right) \frac{\partial}{\partial \eta} \left(\frac{1}{\sqrt{1 - \eta^2}} \Phi_m \right) \right. \\ \left. + \left(\frac{m^2 - 1}{\xi^2 - 1} + \frac{m^2 - 1}{1 - \eta^2} + 2 + \frac{2}{\xi^2} \right) \Phi_m^* \Phi_m \right] - E \int_1^\infty d\xi \int_{-1}^1 d\eta (\xi^2 - \eta^2) \Phi_m^* \Phi_m \right\} = 0 \end{aligned} \quad (1.3.34)$$

for odd $|m|$. This is done to ensure accurate numerical solutions of the Shrödinger equation (differential equations) for both *even* and *odd* projections of angular momentum.

The matrix eigenvalue problems which appear after the discretization of Eq. (1.3.32) can be written can be written as follows for even m values,

$$\sum i'j' \left[T_{ij,i'j'}^e - \left(\frac{Z_1(\xi_i - \eta_j)}{a(\xi_i^2 - \eta_j^2)} - \frac{Z_2(\xi_i + \eta_j)}{a(\xi_i^2 - \eta_j^2)} \right) \delta_{ii'} \delta_{jj'} \right] \Phi_{m;i'j'} = E \Phi_{m;i'j'}, \quad (1.3.35)$$

and odd m values,

$$\begin{aligned} & \sum i'j' \left[T_{ij,i'j'}^o - \left(\frac{Z_1(\xi_i - \eta_j)}{a(\xi_i^2 - \eta_j^2)} - \frac{Z_2(\xi_i + \eta_j)}{a(\xi_i^2 - \eta_j^2)} + \frac{1 + \xi_i^{-2}}{a^2(\xi_i^2 - \eta_j^2)} \right) \delta_{ii'} \delta_{jj'} \right] \Phi_{m;i'j'} \\ & = E \Phi_{m;i'j'}, \end{aligned} \quad (1.3.36)$$

respectively. Next, we construct the kinetic energy matrices $T_{ij,i'j'}^{e,o}$ for *even* m values,

$$\begin{aligned} T_{ij,i'j'}^e &= \frac{1}{2a'^2} \left[\delta_{jj'} \frac{\eta_j'}{(1 - y_j^2)} \sum_{k=1}^{N_x} \frac{1}{\xi_k'} \frac{(\xi_k^2 - 1)}{(1 - x_k^2)} D_{ki}^{(x)} D_{ki'}^{(x)} \right. \\ & \quad \left. + \delta_{ii'} \frac{\xi_i'}{(1 - x_i^2)} \sum_{k=1}^{N_y} \frac{1}{\eta_k'} \frac{(1 - \eta_k^2)}{(1 - y_k^2)} D_{kj}^{(y)} D_{kj'}^{(y)} \right] \\ & \quad \times \sqrt{\frac{(1 - x_i^2)(1 - y_j^2)}{\xi_i' \eta_j' (\xi_i^2 - \eta_j^2)}} \sqrt{\frac{(1 - x_{i'}^2)(1 - y_{j'}^2)}{\xi_{i'}' \eta_{j'}' (\xi_{i'}^2 - \eta_{j'}^2)}} + \delta_{ii'} \delta_{jj'} \frac{1}{2a'^2} \frac{m^2}{(1 - \eta_j^2)(\xi_i^2 - 1)}, \end{aligned} \quad (1.3.37)$$

and *odd* m values,

$$\begin{aligned} T_{ij,i'j'}^o &= \frac{1}{2a'^2} \frac{1}{\sqrt{(\xi_i^2 - \eta_j^2)(\xi_{i'}^2 - \eta_{j'}^2)}} \\ & \quad \times \left\{ \delta_{jj'} \sqrt{\frac{(1 - x_i^2)(1 - x_{i'}^2) \xi_i^2 \xi_{i'}^2}{\xi_i' \xi_{i'}' (\xi_i^2 - 1)(\xi_{i'}^2 - 1)}} \sum_{k=1}^{N_x} \frac{1}{\xi_k'} \frac{(\xi_k^2 - 1)^2}{\xi_k^2 (1 - x_k^2)} D_{ki}^{(x)} D_{ki'}^{(x)} \right. \\ & \quad + \delta_{ii'} \sqrt{\frac{(1 - y_j^2)(1 - y_{j'}^2)}{\eta_j' \eta_{j'}' (1 - \eta_j^2)(1 - \eta_{j'}^2)}} \sum_{k=1}^{N_y} \frac{1}{\eta_k'} \frac{(1 - \eta_k^2)^2}{(1 - y_k^2)} D_{kj}^{(y)} D_{kj'}^{(y)} + \delta_{ii'} \delta_{jj'} \left(\frac{2}{\eta_i^2} \right. \\ & \quad \left. \left. + 2 + \frac{m^2 - 1}{2a^2(\xi_i^2 - 1)(1 - \eta_j^2)} \right) \right\}, \end{aligned} \quad (1.3.38)$$

respectively. The kinetic energy matrices in Eqs. (1.3.37) and (1.3.38) were derived from a set of equations that give direct solution to the operator for the kinetic energy, given by

$$\begin{aligned} \langle \Theta \left| -\frac{1}{2}\nabla^2 \right| \Phi \rangle &= 2\pi a'^3 \int_1^\infty d\xi \int_{-1}^1 d\eta \frac{1}{2a'^2} \left[(\xi^2 - 1) \frac{\partial \Theta^*}{\partial \xi} \frac{\partial \Phi}{\partial \xi} \right. \\ &\quad \left. + (1 - \eta^2) \frac{\partial \Theta^*}{\partial \eta} \frac{\partial \Phi}{\partial \eta} + \frac{M^2}{(\xi^2 - 1)(1 - \eta^2)} \Theta^* \Phi \right]. \end{aligned} \quad (1.3.39)$$

In Eq. (1.3.39) the matrix elements derivatives for the pseudoradial and pseudoangular must be derived from the following set of equations:

$$(\xi^2 - 1) \frac{\partial \Theta^*}{\partial \xi} \frac{\partial \Phi}{\partial \xi} = \sum_{i=1}^{N_x} \frac{\xi'_i}{(1 - x_i^2)} (\xi_i^2 - 1) \sum_{k=1} \frac{1}{\xi'_i} D_{ik} \Theta_k \sum_{l=1} \frac{1}{\xi'_i} D_{il} \Phi_l, \quad (1.3.40)$$

where

$$\frac{\partial}{\partial \xi} = \frac{\partial x}{\partial \xi} \frac{\partial}{\partial x} = \frac{1}{\xi'} \frac{\partial}{\partial x}. \quad (1.3.41)$$

The integration matrix for Eqs. (1.3.33), (1.3.34), and (1.3.39) takes the form,

$$\int dr \Theta^* \Phi = 2\pi a'^3 \sum_{i=1}^{N_x} \sum_{j=1}^{N_y} \Theta_{ij}^* \Phi_{ij} (\xi_i^2 - \eta_j^2) \frac{\xi'_i}{(1 - x_i^2)} \frac{\eta'_j}{(1 - y_j^2)}. \quad (1.3.42)$$

The matrix element derivatives in the Hamiltonian, Eq. (1.3.32) are constructed below that define Eqs. (1.3.37-1.3.38), which are represented by

$$\frac{\partial}{\partial \xi} (\xi^2 - 1) \frac{\partial}{\partial \xi} = - \sum_{k=1}^{N_x} (\xi^2 - 1) \mathbf{D}_{ki}^{(x)} \mathbf{D}_{ki}^{(x)}, \quad (1.3.43)$$

$$(\xi^2 - 1) \frac{\partial}{\partial \xi} = \frac{1}{2} \{ (\xi_i^2 - 1) \mathbf{D}_{ii'}^{(x)} - (\xi_{i'}^2 - 1) \mathbf{D}_{i'i}^{(x)} \}, \quad (1.3.44)$$

where

$$\mathbf{D}_{ii'} = \sqrt{\frac{1 - x_{i'}^2}{1 - x_i^2}} \frac{D_{ii'}^{(x)}}{\sqrt{\xi'_i \xi'_{i'}}}. \quad (1.3.45)$$

To solve Eq. (1.3.32) for *odd* projections of the angular momentum $|m|$, more work needs to be done to ensure the *exact* eigenfunctions are calculated at the nuclei. This is done by a factor of $(\xi - 1)^{|m|/2}(1 - \eta)^{|m|/2}$ being multiplied by the wave function Φ . This form of the wave function already takes place in Eqs. (1.3.34) and (1.3.38). We will now show the case for $|m| = 1$, which is a π symmetry for a diatomic molecule. The new wavefunction takes the form:

$$\Phi = \frac{\Psi}{\sqrt{(\xi^2 - 1)(1 - \eta^2)}}. \quad (1.3.46)$$

So the new wave function is some factor f times Ψ ($\Phi = f\Psi$) and the derivative of the function f :

$$\frac{\partial f}{\partial \xi} = -\frac{\xi}{\xi^2 - 1}f. \quad (1.3.47)$$

The pseudoradial (ξ) derivative for Eq. (1.3.46), which is the *odd* angular momentum $|m|$ wave function is given by

$$\frac{\partial}{\partial \xi}(\xi^2 - 1)\frac{\partial \Phi}{\partial \xi} = f \left(\frac{1}{\xi^2 - 1}\Psi + (\xi^2 - 1)\frac{\partial^2 \Psi}{\partial \xi^2} \right), \quad (1.3.48)$$

and similar the pseudoangular (η) wave function derivative is given by

$$\frac{\partial}{\partial \eta}(1 - \eta^2)\frac{\partial \Phi}{\partial \eta} = f \left(\frac{1}{1 - \eta^2}\Psi + (1 - \eta^2)\frac{\partial^2 \Psi}{\partial \eta^2} \right), \quad (1.3.49)$$

respectively. The derivatives with respect to the mesh x , and y have the following

form:

$$\frac{\partial \Phi}{\partial x} = \frac{\partial \Psi}{\partial x} - \frac{\xi \xi'}{\xi^2 - 1} \Psi \quad (1.3.50)$$

$$\frac{\partial \Phi}{\partial y} = \frac{\partial \Psi}{\partial y} + \frac{\eta \eta'}{\eta^2 - 1} \Psi \quad (1.3.51)$$

Now that we have shown the following forms of the Legendre-Gauss-Radau quadratures and derivatives of the pseudoradial (ξ) and pseudoangular (η) coordinates it is straightforward to construct Eqs. (1.3.32)-(1.3.39). This procedure is for accurate and efficient determination of electronic structure calculations of two-center molecular systems.

1.4 Conclusion

In this chapter, we presented a new GPS method detailed derivation for the discretization of two-center molecular systems with the use of prolate spheroidal coordinates. This procedure is for accurate and efficient determination of electronic structure and dynamic calculations of two-center molecular systems. The extension of the GPS method can be applied to any diatomic molecular systems (homonuclear or heteronuclear) to study electron structure and accurate wave functions for the study of dynamics such as HHG and other multiphoton processes in intense laser fields. Extensions of the present method which are currently in work include the addition of the nuclear vibrational degree of freedom and three-center molecular systems.

Chapter 2

Time-Dependent Density-Functional Theory (TDDFT) for Molecular Processes in Strong Fields

2.1 Introduction

Since the fundamental work of Hohenberg and Kohn [31] and Kohn and Sham [36], the density-functional theory (DFT) has undergone significant theoretical and computational advances in recent years. DFT has become a widely used formalism for electronic-structure calculations of ground-state properties of atoms, molecules, and solids [47, 18]. In the Kohn-Sham DFT formalism [36], the electron density is decomposed into a set of orbitals, leading to a set of one-electron like Schrödinger-like equations to be solved self-consistently. The Kohn-Sham equations are structurally

similar to the Hartree-Fock equations, but include, in principle, exactly the many-body effects through a *local* exchange-correlation (xc) potential [61]. Thus DFT is computational much less expensive than traditional *ab initio* many-electron wavefunction approaches and this accounts for its great success in large systems.

Here, we extend the TDDFT, with proper long range potentials [6], to the study of multi-electron heteronuclear diatomic molecules (homonuclear and heteronuclear) with an aim to explore the dynamical role and nonlinear response of individual electron spin orbital as well as the effect of asymmetry of the molecules to intense laser pulse fields, a subject of largely unexplored area of intense field AMO physics. We describe the TDDFT formalism in great detail for the general treatment of the multiphoton dynamics of heteronuclear and homonuclear diatomic molecular systems. Then we outline a generalized pseudospectral (GPS) method for *nonuniform* and optimal spatial discretization of the two-center molecular systems. Finally, we present a time-dependent GPS method for efficient and accurate solution of TDDFT equations in space and time. The method can be applied to the nonperturbative investigation of multiphoton ionization (MPI) and high harmonic generation (HHG) for any diatomic system in intense linearly polarized laser pulses.

2.2 Time-Dependent Generalized Pseudospectral Method for Numerical Solution of TDDFT Equations

Time dependent density functional theory (TDDFT) is based on the existence of the one-to-one correspondence between the time-dependent electron density and time-dependent potential. We consider the quantum action integral

$$A = \int_{t_0}^{t_f} dt \left\langle \Psi(t) \left| i \frac{\partial}{\partial t} - \hat{H}(t) \right| \Psi(t) \right\rangle, \quad (2.2.1)$$

where within the single determinant approximation, the total N -electron wave function $\Psi(t)$ can be expressed as

$$\Psi(t) = \frac{1}{\sqrt{N!}} \det[\psi_1 \cdot \psi_2 \cdots \psi_N], \quad (2.2.2)$$

and the total electron density at time t is determined by the set of occupied single-electron Kohn-Sham spin-orbital wave functions $\psi_{i\sigma}$ as

$$\begin{aligned} \rho(\mathbf{r}, t) &= \sum_{\sigma} \sum_{i=1}^{N_{\sigma}} \psi_{i\sigma}^* \psi_{i\sigma} \\ &= \sum_{\sigma} \sum_{i=1}^{N_{\sigma}} \rho_{i\sigma}(\mathbf{r}, t) = \rho_{\uparrow}(\mathbf{r}, t) + \rho_{\downarrow}(\mathbf{r}, t). \end{aligned} \quad (2.2.3)$$

We choose the set of spin orbitals $\{\psi_{i\sigma}(\mathbf{r}, t)\}$ which render the total action functional $A[\rho]$ *stationary* [71, 62, 63]. From the Euler equation

$$\frac{\delta A[\rho(\mathbf{r}, t)]}{\delta \rho_\sigma(\mathbf{r}, t)} = 0, \quad (2.2.4)$$

we get (in atomic units)

$$i \frac{\partial}{\partial t} \psi_{i\sigma}(\mathbf{r}, t) = \hat{H}(\mathbf{r}, t) \psi_{i\sigma}(\mathbf{r}, t) = \left[-\frac{1}{2} \nabla^2 + v_{\text{eff},\sigma}(\mathbf{r}, t) \right] \psi_{i\sigma}(\mathbf{r}, t), \quad (2.2.5)$$

$$i = 1, 2, \dots, N_\sigma,$$

where $N_\sigma (= N_\uparrow \text{ or } N_\downarrow)$ is the total number of electrons for a given spin σ . The total number of electrons in the system is $N = \sum_\sigma N_\sigma$. The time-dependent effective potential $v_{\text{eff},\sigma}(\mathbf{r}, t)$ is a functional of the electron spin-densities $\rho_\sigma(\mathbf{r}, t)$ given by

$$v_{\text{eff},\sigma}([\rho]; \mathbf{r}, t) = v_{\text{H}}(\mathbf{r}, t) + v_{\text{ext}}(\mathbf{r}, t) + v_{\text{xc},\sigma}(\mathbf{r}, t), \quad (2.2.6)$$

where $v_{\text{H}}(\mathbf{r}, t)$ is the Hartree potential

$$v_{\text{H}}(\mathbf{r}, t) = \int \frac{\rho(\mathbf{r}', t)}{|\mathbf{r} - \mathbf{r}'|} d^3\mathbf{r}'. \quad (2.2.7)$$

The "external" potential $v_{\text{ext}}(\mathbf{r}, t)$ is due to the interaction of the electron with the external laser field and the nuclei. In the case of a diatomic molecule in a linearly polarized external laser field, we have

$$v_{\text{ext}}(\mathbf{r}, t) = -\frac{Z_1}{|\mathbf{r} - \mathbf{R}_1|} - \frac{Z_2}{|\mathbf{r} - \mathbf{R}_2|} + \mathbf{E}(t) \cdot \mathbf{r} \sin \omega t. \quad (2.2.8)$$

Eq. (2.2.8) discretized in prolate spheroidal coordinates is given by

$$v_{\text{ext}}(\xi, \eta, t) = -\frac{Z_1(\xi - \eta)}{a(\xi^2 - \eta^2)} - \frac{Z_2(\xi + \eta)}{a(\xi^2 - \eta^2)} + \frac{(a + b)}{2}\mathbf{E}(t) \cdot \xi\eta \sin \omega t, \quad (2.2.9)$$

where $\mathbf{R}_1 = (0, 0, -a)$ and $\mathbf{R}_2 = (0, 0, b)$ are the foci of the two nuclei in Cartesian coordinates and Z_1 and Z_2 are the effective charges of the nuclei, respectively. \mathbf{r} is the electronic coordinate, $E(t)$ the electric field amplitude. The internuclear separation R is equal to $(a + b)/2$. $v_{\text{xc},\sigma}(\mathbf{r}, t)$ is the time-dependent exchange-correlation (xc) potential. Since the exact form of $v_{\text{xc},\sigma}(\mathbf{r}, t)$ is unknown, the *adiabatic* approximation is often used [71, 65, 30, 10, 11]

$$v_{\text{xc},\sigma}(\mathbf{r}, t) = v_{\text{xc},\sigma}[\rho_\sigma]|_{\rho_\sigma=\rho_\sigma(\mathbf{r},t)}. \quad (2.2.10)$$

Note that if the conventional *explicit* xc energy functional forms taken from local spin density approximation (LSDA) or generalized gradient approximation (GGA) [47, 18] are used, the corresponding xc potential $v_{\text{xc},\sigma}(\mathbf{r}, t)$ will not possess the correct long-range asymptotic $(-1/r)$ behavior [61]. Here, we adopt the improved LB potential [52], $v_{\text{xc},\sigma}^{\text{LB}\alpha}$, which contains two empirical parameters α and β and has the following form, in the adiabatic approximation,

$$v_{\text{xc},\sigma}^{\text{LB}\alpha}(\mathbf{r}, t) = \alpha v_{\text{x},\sigma}^{\text{LSDA}}(\mathbf{r}, t) + v_{\text{c},\sigma}^{\text{LSDA}}(\mathbf{r}, t) - \frac{\beta x_\sigma^2(\mathbf{r}, t) \rho_\sigma^{1/3}(\mathbf{r}, t)}{1 + 3\beta x_\sigma(\mathbf{r}, t) \ln\{x_\sigma(\mathbf{r}, t) + [x_\sigma^2(\mathbf{r}, t) + 1]^{1/2}\}}. \quad (2.2.11)$$

Here, ρ_σ is the electron density with spin σ , and we use $\alpha = 1.19$ and $\beta = 0.01$

[11, 30]. The first two terms in Eq. (2.2.11), $v_{x,\sigma}^{\text{LSDA}}$ and $v_{c,\sigma}^{\text{LSDA}}$ are the LSDA exchange and correlation potentials that do *not* have the correct asymptotic behavior. The last term in Eq. (2.2.11) is the nonlocal gradient correction with $x_\sigma(\mathbf{r}) = |\nabla\rho_\sigma(\mathbf{r})|/\rho_\sigma^{4/3}(\mathbf{r})$, which ensures the proper long-range asymptotic potential $v_{xc,\sigma}^{\text{LB}\alpha} \rightarrow -1/r$ as $r \rightarrow \infty$. For the time-independent case, this exchange-correlation LB α potential has been found to be reliable for atomic and molecular DFT calculations.

2.3 TDDFT Method for Diatomic Molecules

The central theme of the TDDFT involves a set of time-dependent one-electron Schrödinger-like Kohn-Sham (KS) equations [36] for N -electron atomic or molecular systems, outlined in Eq. (2.2.5). In Eq. (2.2.5), $\hat{H}_0(\mathbf{r})$ is the field-free Hamiltonian for a diatomic molecule, which in atomic units, can be written as

$$\hat{H}_0(\mathbf{r}) = -\frac{1}{2}\nabla^2 - \frac{Z_1}{|\mathbf{R}_1 - \mathbf{r}|} - \frac{Z_2}{|\mathbf{R}_2 - \mathbf{r}|} + v_{\text{H}}(\mathbf{r}) + v_{xc,\sigma}(\mathbf{r}). \quad (2.3.1)$$

In chapter 1 the GPS method with use of the prolate spheroidal coordinates was used to discretize the electronic Hamiltonian. There we described the *even* and *odd* projections of angular momentum, and the different forms of the Hamiltonian $\hat{H}_0^{e,o}(\xi, \eta, \varphi)$ for each of these angular momentum m and orbital σ , which has the following form:

$$\begin{aligned} \hat{H}_0^e(\xi, \eta, \varphi) = & -\frac{1}{2a'^2} \frac{1}{(\xi^2 - \eta^2)} \left[\frac{\partial}{\partial \xi}(\xi^2 - 1) \frac{\partial}{\partial \xi} + \frac{\partial}{\partial \eta}(1 - \eta^2) \frac{\partial}{\partial \eta} + \frac{m^2}{(1 - \eta^2)(\xi^2 - 1)} \right] \\ & - \frac{Z_1(\xi - \eta)}{a(\xi^2 - \eta^2)} - \frac{Z_2(\xi + \eta)}{a(\xi^2 - \eta^2)} + v_H(\xi, \eta) + v_{xc,\sigma}(\xi, \eta), \end{aligned} \quad (2.3.2)$$

for *even* m and

$$\begin{aligned} \hat{H}_0^o(\xi, \eta, \varphi) = & -\frac{1}{2a'^2} \frac{1}{(\xi^2 - \eta^2)} \left[\frac{\partial}{\partial \xi}(\xi^2 - 1) \frac{\partial}{\partial \xi} + \frac{\partial}{\partial \eta}(1 - \eta^2) \frac{\partial}{\partial \eta} + \frac{2}{\eta^2} + 2 \right. \\ & \left. + \frac{m^2 - 1}{2a^2(\xi^2 - 1)(1 - \eta^2)} \right] \\ & + v_H(\xi, \eta) + v_{xc,\sigma}(\xi, \eta), \end{aligned} \quad (2.3.3)$$

for *odd* m , respectively. Now we consider *nonuniform* and optimal grid discretization of the spatial coordinates by means of the two-center *generalized pseudospectral* (GPS) technique, again explained in chapter 1 with great detail. We shall use the following mapping transformations for the coordinates ξ and η :

$$\eta(y) = y, \quad -1 \leq y \leq 1, \quad (2.3.4)$$

$$\xi(x) = 1 + L \frac{1+x}{1-x}, \quad -1 \leq x \leq 1, \quad (2.3.5)$$

L being the mapping parameter. The variables x and y are discretized using the Legendre-Gauss-Radau abscissas x_i and y_j as the collocation points. The Legendre-Gauss-Radau quadrature can be written as follows:

$$\int d^3r \Phi^2 = 2\pi a^3 \sum_{i=1}^{N_\xi} \sum_{j=1}^{N_\eta} \phi_{ij}^2, \quad (2.3.6)$$

where N_ξ and N_η are the numbers of collocation points x_i and y_j , respectively. The values of ϕ_{ij} are related to the function Φ at the collocation points x_i and y_j ,

$$\Phi(\xi(x_i), \eta(y_j)) = \sqrt{\frac{(1-x_i^2)(1-y_j^2)}{\xi_i' \eta_j' (\xi_i^2 - \eta_j^2)}} P'_{N_\xi}(x_i) P'_{N_\eta}(y_j) \phi_{ij}. \quad (2.3.7)$$

In Eq. (2.3.7), the primes denote the derivatives of the functions with respect to their arguments. The discretized electronic Hamiltonian for Eqs. (2.3.2) and (2.3.3) is a matrix of order $N_\xi N_\eta \times N_\xi N_\eta$ which acts on the vector $\{\phi_{ij}\}$, the matrix elements being

$$\begin{aligned} H_{ij,i'j'}^e = & \frac{1}{2a'^2} \left[\delta_{jj'} \frac{\eta_j'}{(1-y_j^2)} \sum_{k=1}^{N_x} \frac{1}{\xi_k'} \frac{(\xi_k^2 - 1)}{(1-x_k^2)} D_{ki}^{(x)} D_{ki'}^{(x)} \right. \\ & \left. + \delta_{ii'} \frac{\xi_i'}{(1-x_i^2)} \sum_{k=1}^{N_y} \frac{1}{\eta_k'} \frac{(1-\eta_k^2)}{(1-y_k^2)} D_{kj}^{(y)} D_{kj'}^{(y)} \right] \\ & \times \sqrt{\frac{(1-x_i^2)(1-y_j^2)}{\xi_i' \eta_j' (\xi_i^2 - \eta_j^2)}} \sqrt{\frac{(1-x_{i'}^2)(1-y_{j'}^2)}{\xi_{i'}' \eta_{j'}' (\xi_{i'}^2 - \eta_{j'}^2)}} + \delta_{ii'} \delta_{jj'} \left[\frac{1}{2a'^2} \frac{m^2}{(1-\eta_j^2)(\xi_i^2 - 1)} \right. \\ & \left. - \frac{Z_1(\xi_i - \eta_j)}{a(\xi_i^2 - \eta_j^2)} - \frac{Z_2(\xi_i + \eta_j)}{a(\xi_i^2 - \eta_j^2)} + v_H(\xi_i, \eta_j) + v_{xc,\sigma}(\xi_i, \eta_j) \right], \end{aligned} \quad (2.3.8)$$

for *even* m and

$$\begin{aligned} H_{ij,i'j'}^o = & \frac{1}{2a'^2} \left[\delta_{jj'} \frac{\eta_j'}{(1-y_j^2)} \sum_{k=1}^{N_x} \frac{1}{\xi_k'} \frac{(\xi_k^2 - 1)}{(1-x_k^2)} D_{ki}^{(x)} D_{ki'}^{(x)} \right. \\ & \left. + \delta_{ii'} \frac{\xi_i'}{(1-x_i^2)} \sum_{k=1}^{N_y} \frac{1}{\eta_k'} \frac{(1-\eta_k^2)}{(1-y_k^2)} D_{kj}^{(y)} D_{kj'}^{(y)} \right] \sqrt{\frac{(1-x_i^2)(1-y_j^2)}{\xi_i' \eta_j' (\xi_i^2 - \eta_j^2)}} \\ & \times \sqrt{\frac{(1-x_{i'}^2)(1-y_{j'}^2)}{\xi_{i'}' \eta_{j'}' (\xi_{i'}^2 - \eta_{j'}^2)}} + \delta_{ii'} \delta_{jj'} \left[+ \frac{2}{\eta_j^2} + 2 + \frac{m^2 - 1}{2a^2(\xi_i^2 - 1)(1-\eta_j^2)} \right. \\ & \left. - \frac{Z_1(\xi_i - \eta_j)}{a(\xi_i^2 - \eta_j^2)} - \frac{Z_2(\xi_i + \eta_j)}{a(\xi_i^2 - \eta_j^2)} + v_H(\xi_i, \eta_j) + v_{xc,\sigma}(\xi_i, \eta_j) \right], \end{aligned} \quad (2.3.9)$$

for *odd* m . The first derivative matrices $D_{ii}^{(x)}$, $D_{jj}^{(y)}$ have simple analytical expressions in the pseudospectral method; a detailed construction is given in chapter 1. Next we will show in detail how one would solve the Hartree potential $v_H(\xi_i, \eta_j)$ in the DFT method, and the boundary conditions for this potential.

2.4 Dirichlet Boundary Conditions for the Hartree Potential in DFT Formulism

When solving the Poisson equation for the potential $v_H(\xi, \eta)$:

$$\nabla^2 V = -4\pi\rho(\mathbf{r}), \quad (2.4.1)$$

where

$$V = v_H(\mathbf{r}) = \int d^3\mathbf{r}' \frac{\rho(\mathbf{r}')}{|\mathbf{r} - \mathbf{r}'|}, \quad (2.4.2)$$

one must specify the boundary conditions for V . We know that the correct potential must behave like Z/r as $r \rightarrow \infty$ where $Z = \int \rho(\mathbf{r})d\mathbf{r}$ (the total charge). Then for $R_{max} = \infty$ ($x = +1$ and $\xi = R_{max} = \infty$) the boundary condition is $V = 0$ (it is not explicitly imposed since the numerical solution satisfies it anyway). For finite R_{max} , we need to impose $V(R_{max}) = Z/R_{max}$. In prolate spheroidal coordinates, we express \mathbf{r} through ξ and η ; in that case for $\xi = \xi_{max}$ ($\xi(x = +1)$) the boundary

condition $V(R_{max}) = Z/R_{max}$ will depend on η since R_{max} now depends on η . In prolate spheroidal coordinates the potential V for a diatomic molecule on the boundary $V(R_{max}, \eta)$ has the following form:

$$V(R_{max}, \eta) = \frac{(Z_1 + Z_2)R_{max}}{a(R_{max}^2 - \eta^2)}. \quad (2.4.3)$$

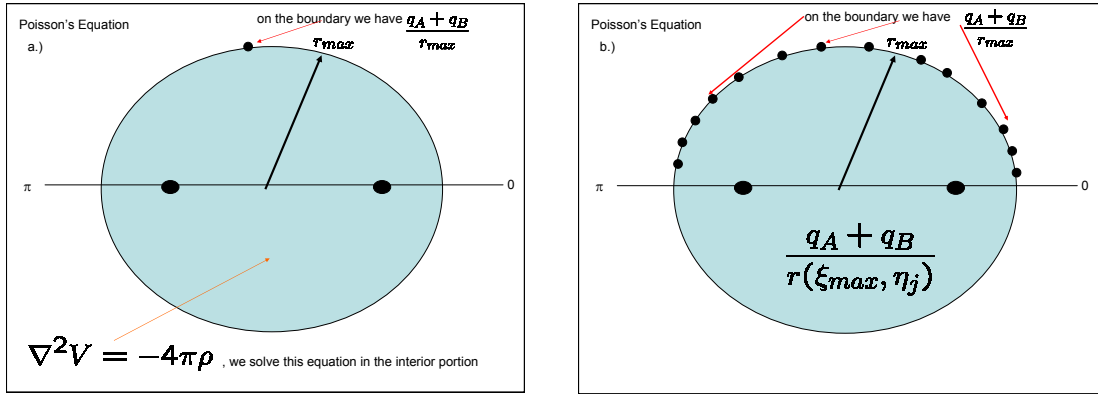


Figure 2.1: Dirichlet boundary conditions for the Hartree potential (a) interior portion of the Hartree potential (b) boundary condition for the Hartree potential at $x = +1$ or $\xi = R_{max}$.

The boundary problem for the potential at R_{max} needs to be only calculated once (Fig. 2.1(b)), and inside the boundary $V(r < R_{max})$ is calculated with the new updated density $\rho(r)$ (Fig. 2.1(a)) for time-independent or $\rho(r, t)$ for time-dependent calculations by use of Eq. (2.4.1). Using Eq. (2.4.1) and knowing $\nabla^2(\xi, \eta)$ and its matrix inverse the potential V is solved by the following expression:

$$V(\mathbf{r}) = -4\pi\{\nabla^2\}^{-1}\rho(\mathbf{r}), \quad (2.4.4)$$

where

$$\{\nabla^2\}^{-1}\nabla^2 = I. \quad (2.4.5)$$

Therefor, once we discretize $\nabla^2(\xi, \eta)$ once and solve the updated density $\rho(\xi, \eta)$ self-consistent, then Eq. (2.4.4) is also solved self-consistent with the updated density.

2.5 TDDFT for Intense-Field Multiphoton Processes

Now that we have shown explicit representation of the Hartree potential and the Hamiltonian, Eqs. (2.3.2) and (2.3.3) have been diagonalized and we have solved the time-independent DFT formulism in a self-consistent manner. We now have the diatomic molecules electronic structure (eigenvalues and eigenvectors) which now can be propagated in time using Eq. (2.2.5). In this section, we outline the time-dependent generalized pseudospectral (TDGPS) procedure for the solution of the set of time-dependent equations for two-center molecular systems. The TDGPS is extended for accurate and efficient non-perturbative treatment of multiple high-order harmonic generation (HHG) of diatomic molecules in intense laser fields. The advantage of this

method is that it allows nonuniform and optimal spatial grid discretization (denser mesh near each nucleus and sparser mesh at larger electron-nucleus separations). This improves greatly both the accuracy and the efficiency of the electronic structure and time-dependent calculations. The commonly used procedures for the time propagation of the Schrödinger equation employ *equal-spacing* spatial-grid discretization [39]. For processes such as HHG, accurate time-dependent wave functions are required to achieve convergence since the intensity of various harmonic peaks can span a range of many orders of magnitude. High precision accuracy is generally more difficult to achieve by the equal-spacing spatial-grid-discretization time-dependent techniques. The TDGPS method consist of the following two basic steps. (i) A two-center GPS technique [58] is used for optimal grid discretization of the pseudoradial (ξ) and pseudoangular (η) coordinates. The number of grid points required is generally considerably smaller than those used by the equal-spacing discretization methods. Yet higher accuracy in wave functions and therefore HHG spectra can be achieved, since the physically more important short-range regime is treated accurately by this method. (ii) A split-operator technique in the *energy* representation is introduced for efficient time propagation of the wave functions. In this work, we extend this procedure to the numerical solution of the two-centered systems in the time-dependent equations.

Consider the solution of the time-dependent one-electron Kohn-Sham-like equation [36] for N -electron molecular systems in linearly polarized laser fields,

$$i\frac{\partial}{\partial t}\psi_{i\sigma}(\xi, \eta, \varphi, t) = \hat{H}\psi_{i\sigma}(\xi, \eta, \varphi, t) = \left[\hat{H}_0(\xi, \eta, \varphi) + \hat{V}(\xi, \eta, t) \right] \psi_{i\sigma}(\xi, \eta, \varphi, t), \quad (2.5.1)$$

$$i = 1, 2, \dots, N_\sigma,$$

where σ is the spin index. Here \hat{H}_0 is the time-independent Hamiltonian at $t = 0$, and \hat{V} includes the electron-laser field interaction:

$$\begin{aligned} \hat{H}_0(\xi, \eta, \varphi) = & -\frac{1}{2a'^2} \frac{1}{(\xi^2 - \eta^2)} \left[\frac{\partial}{\partial \xi}(\xi^2 - 1) \frac{\partial}{\partial \xi} + \frac{\partial}{\partial \eta}(1 - \eta^2) \frac{\partial}{\partial \eta} - \frac{m^2}{\xi^2 - 1} - \frac{m^2}{1 - \eta^2} \right] \\ & - \frac{Z_1(\xi - \eta)}{a(\xi^2 - \eta^2)} - \frac{Z_2(\xi + \eta)}{a(\xi^2 - \eta^2)}, \end{aligned} \quad (2.5.2)$$

We will show the electron-laser field interaction term $V(\xi, \eta, t)$, which includes other residual time-dependent terms in $v_{\text{eff},\sigma}([\rho]; \xi, \eta, t)$:

$$\begin{aligned} V(\xi, \eta, t) = & \frac{(a + b)}{2} E(t) \cdot \xi \eta \sin \omega t + (v_{\text{H}}(\xi, \eta, t) - v_{\text{H}}(\xi, \eta, 0)) \\ & + (v_{\text{xc},\sigma}(\xi, \eta, t) - v_{\text{xc},\sigma}(\xi, \eta, 0)), \end{aligned} \quad (2.5.3)$$

where $v_{\text{H}}(\xi, \eta, 0)$ and $v_{\text{xc},\sigma}(\xi, \eta, 0)$ are the time-independent potentials ($t = 0$). Here $\mathbf{E}(t)$ is the electric field which is parallel to the internuclear ($\hat{\mathbf{z}}$) axis, and $E(t) = Ff(t)$, where $f(t)$ is the envelope function of the laser pulse. We shall extend the second-order split-operator technique in prolate spheroidal coordinates and in the *energy* representation for propagation of the molecular Schrödinger equation:

$$\begin{aligned} \psi_{i\sigma}(\xi, \eta, \varphi, t + \Delta t) \simeq & \exp(-i\hat{H}_0(\xi, \eta, \varphi)\Delta t/2) \cdot \exp(-iV_\sigma(\xi, \eta, \Delta t/2)\Delta t) \\ & \times \exp(-i\hat{H}_0(\xi, \eta, \varphi)\Delta t/2)\psi_{i\sigma}(\xi, \eta, \varphi, t) + \mathcal{O}(\Delta t^3). \end{aligned} \quad (2.5.4)$$

The use of the *energy* representation in Eq. (2.5.4) allows for the elimination of the undesirable fast-oscillating *high-energy* components and speeds up considerably in time propagation [60].

To pursue the time propagation of the wave function from t to $t + \Delta t$ is achieved by three steps: (i) First the wave function $\psi_{i\sigma}(\xi, \eta, \varphi, t)$ is propagated for a half-time step $\Delta t/2$ in the energy space spanned by $\hat{H}_0(\xi, \eta, \varphi)$. For this we construct the time-*independent* evolution operator

$$\exp(-i\hat{H}_0(\xi, \eta, \varphi)\Delta t/2) \equiv \hat{S}, \quad (2.5.5)$$

by means of GPS discretization and solution of the field-free Hamiltonian, Eq. (1.3.32):

$$H_0(\xi, \eta, \varphi)\chi_k(\xi, \eta, \varphi) = \epsilon_k\chi_k(\xi, \eta, \varphi). \quad (2.5.6)$$

Then the S -matrix can be constructed as

$$S_{ij,i'j'} = \sum_k \chi_k(\xi_i, \eta_j, \varphi)\chi_k^*(\xi_{i'}, \eta_{j'}, \varphi) \exp(-i\epsilon_k\Delta t/2). \quad (2.5.7)$$

Note that S is a complex symmetric matrix and needs to be constructed only once.

Thus the time propagation in the energy space,

$$\exp(-i\hat{H}_0(\xi, \eta, \varphi)\Delta t/2)\psi_{i\sigma}(\xi, \eta, \varphi, t) \equiv \hat{S}\psi_{i\sigma}(\xi, \eta, \varphi, t) \equiv \psi_{i\sigma}^{(1)}(\xi, \eta, \varphi, t), \quad (2.5.8)$$

is reduced to the matrix-vector product [$\mathcal{O}(N^2)$ operation] which can be performed

efficiently using the basic linear algebra subroutines (BLAS). (ii) Then the wave function $\psi_{i\sigma}^{(1)}(\xi, \eta, \varphi, t)$ is propagated for a time step Δt under the influence of the molecule-field coupling:

$$\exp(-iV_{\sigma}(\xi, \eta, \Delta t/2)\Delta t)\psi_{i\sigma}^{(1)}(\xi, \eta, \varphi, t) \equiv \psi_{i\sigma}^{(2)}(\xi, \eta, \varphi, t). \quad (2.5.9)$$

Since $\exp(-iV_{\sigma}(\xi, \eta, \Delta t/2))$ is a diagonal matrix in the coordinate representation, this is a fast step as far as the CPU time is concerned. (iii) Finally, the wave function $\psi_{i\sigma}^{(2)}(\xi, \eta, \varphi, t)$ is propagated another half-time step $\Delta t/2$:

$$\hat{S}\psi_{i\sigma}^{(2)}(\xi, \eta, \varphi, t) = \psi_{i\sigma}(\xi, \eta, \varphi, t + \Delta t). \quad (2.5.10)$$

This completes one time propagation step in Eq. (2.5.4). After the time-dependent single electron wave functions $\{\psi_{i\sigma}\}$ are obtained, the total electron density $\rho(\mathbf{r}, t)$ can be determined.

Once the time-dependent wave functions and the time-dependent electron densities are obtained, we can calculate the time-dependent (multiphoton) ionization probability of an individual spin-orbital according to

$$P_{i,\sigma} = 1 - N_{i,\sigma}(t), \quad (2.5.11)$$

where

$$N_{i,\sigma}(t) = \langle \psi_{i,\sigma}(t) | \psi_{i,\sigma}(t) \rangle, \quad (2.5.12)$$

is the time-dependent population (survival probability) of the $i\sigma$ -th spin-orbital. After the time-dependent single-electron wave functions $\{\psi_{i\sigma}\}$ are obtained, the induced dipole moment and dipole acceleration can now be expressed for the molecular system, respectively as

$$\begin{aligned} d(t) &= \int z\rho(\mathbf{r}, t)d\mathbf{r} = \sum_{i\sigma} n_{i\sigma} \langle \psi_{i\sigma}(\xi, \eta, \varphi, t) | z | \psi_{i\sigma}(\xi, \eta, \varphi, t) \rangle \\ &= \frac{(a+b)}{2} \langle \psi_{i\sigma}(\xi, \eta, \varphi, t) | \xi\eta | \psi_{i\sigma}(\xi, \eta, \varphi, t) \rangle, \end{aligned} \quad (2.5.13)$$

and

$$\begin{aligned} d_A(t) &= \sum_{i\sigma} n_{i\sigma} \left\langle \psi_{i\sigma}(\xi, \eta, \varphi, t) \left| -\frac{\partial V_\sigma(\xi, \eta, t)}{\partial z} + \frac{\mathbf{E}(t) \cdot \mathbf{r} \sin(\omega t)}{z} \right| \psi_{i\sigma}(\xi, \eta, \varphi, t) \right\rangle \\ &= \sum_{i\sigma} \left\langle \psi_{i\sigma}(\xi, \eta, \varphi, t) \left| -\frac{z}{r^3} + \mathbf{E}(t) \sin(\omega t) \right| \psi_{i\sigma}(\xi, \eta, \varphi, t) \right\rangle, \end{aligned} \quad (2.5.14)$$

where $n_{i\sigma}$ is its electron occupation number. The corresponding HHG power spectrum can now be obtained by the Fourier transformation of the respective time-dependent dipole moment and dipole acceleration:

$$P(\omega) = \left| \frac{1}{t_f - t_i} \int_{t_i}^{t_f} d(t) e^{-i\omega t} dt \right|^2 = |d(\omega)|^2, \quad (2.5.15)$$

$$P_A(\omega) = \left| \frac{1}{t_f - t_i} \frac{1}{\omega^2} \int_{t_i}^{t_f} d_A(t) e^{-i\omega t} dt \right|^2 = |d_A(\omega)|^2. \quad (2.5.16)$$

The power spectra $P(\omega)$ and $P_A(\omega)$ should be the same if the wave function $\psi_{i\sigma}(\xi, \eta, \varphi, t)$ is fully converged. In the presence of either periodic fields or continuous wave (cw)

lasers, one can further obtain the time-independent n th-order harmonic generation emission rate by means of the expression

$$\Gamma_n = \frac{4\omega_0^3 n^3}{3c^3} P(n\omega_0), \quad (2.5.17)$$

or

$$\Gamma_n = \frac{4\omega_0^3 n^3}{3c^3} P_A(n\omega_0), \quad (2.5.18)$$

where ω_0 is the fundamental frequency of the laser field.

2.6 Conclusion

In this chapter, we presented a detailed procedure for diatomic molecules in intense laser fields by means of a TDDFT with correct asymptotic long-range ($-1/r$) potential to ensure individual spin-orbital has the proper ionization potential. We consider only the case that the molecular axis is aligned with the laser beam direction. This is justified based on the recent experimental development of the laser molecular alignment techniques [40, 54, 48, 49]. Much remains to be explored in this fascinating and largely unexplored area of strong-field molecular physics. Finally, the nuclear degree of freedom has not been taken into account so far. This is justified for ultrashort laser pulse excitation.

Chapter 3

High-Order Harmonic Generation of Heteronuclear Diatomic Molecules in Intense Ultrashort Laser Fields: An All-Electron TDDFT Study

3.1 Introduction

The study of atomic and molecular processes in intense ultrashort laser fields is a subject of much current interest in science and technology [2]. In particular, high-order harmonic generation (HHG) is one of the hottest topics in strong-field atomic and molecular physics today, which is closely related to the recent development of attosecond laser pulses [1, 70, 28] as well as the frequency comb technology [25, 34, 7]. To describe such strong-field processes using fully *ab initio* wave-function approach, it is necessary to solve the $(3n+1)$ dimensional time-dependent Schrödinger

equation (TDSE) in space and time, where n is the number of electrons. This is well beyond the capability of current supercomputer technology when $n > 2$. Even for the two-electron ($n = 2$) case, high-precision fully *ab initio* 6D study of the HHG of the He atoms was achieved only very recently [26]. For many-electron molecular ($n \geq 2$) systems, we have recently performed *self-interaction-free* time-dependent density functional theory (TDDFT) calculations for the nonperturbative treatment of multiphoton ionization (MPI) and HHG processes of homonuclear diatomic molecules H_2 [10], N_2 [11, 30], O_2 , and F_2 [13] in intense laser fields.

We extend the TDDFT, with proper long range potentials, to the study of multi-electron heteronuclear diatomic molecules (CO in particular) with an aim to explore the dynamical role and nonlinear response of individual electron spin orbital as well as the effect of asymmetry of the molecules to intense laser pulse fields, a subject of largely unexplored area of intense field AMO physics. In our previous studies of the MPI of homonuclear diatomic molecules N_2 , O_2 , and F_2 , we found that the highest occupied molecular orbital (HOMO) is not necessary the dominant channel responding to the strong-field molecular ionization [13]. Furthermore the ac Stark shift of individual MO and the detailed molecular electronic structure need to be taken into account for a proper and quantitative treatment of the intense AMO processes. In the case of F_2 , for example, while the HOMO is $1\pi_g$, the dominant MO channel to ionization in strong fields turns out to be the $3\sigma_g$ in intense laser fields [13].

Approximate models such as ADK [68] and Keldysh [45] etc., which consider only the HOMO contributing to the molecular ionization and neglect the ac Stark effect, predicted the ionization suppression of F_2 , in disagreement with the experimental observation [16, 74]. In this chapter, we further explore the effect of the asymmetry of the molecules to MPI and HHG. We found that the heteronuclear diatomic molecules can contribute the generation of even harmonics, in addition to the odd harmonics seen in the atomic and homonuclear diatomic cases. Furthermore, we found that there is only one dominant (short-trajectory) rescattering event within each optical cycle. This is different from that seen in the atomic and homonuclear diatomic cases, where two dominant electron rescattering events, one from the short- and the other from the long-trajectory, occur within each optical cycle. Comparing the MPI and HHG behavior of CO with N_2 , it reveals quite dramatic difference in their strong-field nonlinear responses, despite the fact that CO has only a very small (field-free) permanent dipole moment.

3.2 Multiphoton Ionization of N_2 and CO in Intense Laser Fields

The ground-state electronic configurations is

$$1\sigma_g^2 1\sigma_u^2 2\sigma_g^2 2\sigma_u^2 1\pi_u^4 3\sigma_g^2,$$

for N_2 and

$$1\sigma^2 2\sigma^2 3\sigma^2 4\sigma^2 1\pi^4 5\sigma^2,$$

for CO, respectively. N_2 and CO are isoelectronic molecules, both having 14 electrons and triple bonds. Since the CO molecule has unequal nuclear charges, its ground electronic state possesses a permanent dipole moment, calculated here to be 0.149 Debye. The corresponding experimental value is 0.112 Debye [46]. Furthermore, there is no concept of gerade and ungerade orbital's for CO (or any other heteronuclear diatomic molecule) since the inversion symmetry of the potential is broken. Table 3.1 lists the MO energies calculated with the $\text{LB}\alpha$ potential, using 50 grid points in ξ and 30 grid points in η . The agreement of the calculated valence MO energies with the experimental data is well within 0.01 a.u.

Table 3.1: Comparison of the field-free molecular orbital energy levels of CO and N_2 , calculated with the $\text{LB}\alpha$ potential, and the experimental ionization potentials (in a.u.).

CO						
Orbital	1σ	2σ	3σ	4σ	1π	5σ
Expt. [53]	19.9367	10.8742	1.3964	0.7239	0.6247	0.5144
$\text{LB}\alpha$	19.6142	10.6556	1.2549	0.7071	0.6276	0.5086
N_2						
Orbital	$1\sigma_g$	$1\sigma_u$	$2\sigma_g$	$2\sigma_u$	$1\pi_u$	$3\sigma_g$
Expt. [33, 27, 69]	15.0492	15.0492	1.3708	0.6883	0.6233	0.5726
$\text{LB}\alpha$	14.7962	14.7950	1.2162	0.6786	0.6199	0.5682

Next, we outline the time-dependent generalized pseudospectral (TDGPS) procedure for the solution of the set of time-dependent equations, Eq. (2.2.5), for the CO and N₂ molecules. The advantage of this method is that it allows nonuniform and optimal spatial grid discretization (denser mesh near each nucleus and sparser mesh at larger electron-nucleus separations). This improves greatly both the accuracy and the efficiency of the electronic structure and time-dependent calculations. The commonly used procedures for the time propagation of the Schrödinger or TDDFT equation employ *equal-spacing* spatial-grid discretization [39]. For processes such as HHG, accurate time-dependent wave functions are required to achieve convergence since the intensity of various harmonic peaks can span a range of many orders of magnitude. High precision accuracy is generally more difficult to achieve by the equal-spacing spatial-grid-discretization time-dependent techniques. The TDGPS method consist of the following two basic steps. (i) A two-center GPS technique [57, 58, 30] is used for optimal grid discretization of the pseudoradial (ξ) and pseudoangular (η) coordinates. The number of grid points required is generally considerably smaller than those used by the equal-spacing discretization methods. Yet higher accuracy in wave functions and therefore HHG spectra can be achieved, since the physically more important short-range regime is treated accurately by this method. The TDGPS method also has been recently applied successfully to the non-Hermitian Floquet studies of the hydrogen molecular ion H₂⁺ in strong fields [57]. (ii) A split-operator technique in

the *energy* representation is introduced for efficient time propagation of the wave functions. In this work, we extend this procedure to the numerical solution of the two-centered systems in the time-dependent equations.

Consider now the solution of the TDDFT equation, Eq. (2.2.5), recasted into the following form:

$$i \frac{\partial}{\partial t} \psi_{i\sigma}(\mathbf{r}, t) = \hat{H}(\mathbf{r}, t) \psi_{i\sigma}(\mathbf{r}, t) = [\hat{H}_0(\mathbf{r}) + \hat{V}(\mathbf{r}, t)] \psi_{i\sigma}(\mathbf{r}, t), \quad (3.2.1)$$

$$i = 1, 2, \dots, N_\sigma.$$

where \hat{H}_0 is the time-independent Hamiltonian whose matrix elements are given in Eqs. (2.3.8-2.3.9), and $\hat{V}(\mathbf{r}, t)$ includes the electron-laser field interaction and other residual time-dependent terms in $v_{\text{eff},\sigma}([\rho]; \mathbf{r}, t)$:

$$\hat{V}(\mathbf{r}, t) = (\mathbf{E}(t) \cdot \mathbf{r}) \sin \omega t + (v_{\text{H}}(\mathbf{r}, t) - v_{\text{H}}(\mathbf{r}, 0)) + (v_{\text{xc},\sigma}(\mathbf{r}, t) - v_{\text{xc},\sigma}(\mathbf{r}, 0)). \quad (3.2.2)$$

Here $\mathbf{E}(t)$ is the electric field parallel to the internuclear ($\hat{\mathbf{z}}$) axis, and $E(t) = Ff(t)$, where $f(t)$ is the envelope function of the laser pulse. We shall extend the second-order split-operator technique in prolate spheroidal coordinates and in the *energy* representation [60, 30] for the propagation of individual spin-orbital

$$\psi_{i\sigma}(\mathbf{r}, t + \Delta t) \simeq e^{-i\hat{V}(\mathbf{r}, t)\Delta t/2} e^{-i\hat{H}_0(\mathbf{r})\Delta t} e^{-i\hat{V}(\mathbf{r}, t)\Delta t/2} \psi_{i\sigma}(\mathbf{r}, t) + O(\Delta t^3). \quad (3.2.3)$$

Note that such an expression is different from the conventional split-operator techniques [29, 32], where \hat{H}_0 is usually chosen to be the kinetic-energy operator and \hat{V}

the remaining Hamiltonian depending on the spatial coordinates only. The use of the *energy* representation in Eq. (3.2.3) allows the explicit *elimination* of the undesirable fast-oscillating *high-energy* components and speeds up considerably the time propagation [60, 12, 10, 11, 30]. After the time-dependent single electron wave functions $\{\psi_{i\sigma}\}$ are obtained, the total electron density $\rho(\mathbf{r}, t)$ can be determined.

The time-dependent induced dipole moment can now be calculated as

$$d(t) = \int z\rho(\mathbf{r}, t)d\mathbf{r} = \sum_{i\sigma} d_{i\sigma}(t), \quad (3.2.4)$$

where

$$d_{i\sigma}(t) = n_{i\sigma} \langle \psi_{i\sigma}(\mathbf{r}, t) | z | \psi_{i\sigma}(\mathbf{r}, t) \rangle, \quad (3.2.5)$$

is the induced dipole moment of the $i\sigma$ -th spin orbital, and $n_{i\sigma}$ is its electron occupation number. The power spectrum of the HHG is then acquired by taking the Fourier transform of the total time-dependent induced dipole moment $d(t)$:

$$P(\omega) = \frac{4\omega^4}{3c^3} \left| \frac{1}{t_f - t_i} \int_{t_i}^{t_f} d(t) e^{-i\omega t} dt \right|^2. \quad (3.2.6)$$

Here c is the speed of light, and $P(\omega)$ has the meaning of the energy emitted per unit time at the particular photon frequency ω .

Once the time-dependent wave functions and the time-dependent electron densities are obtained, we can calculate the time-dependent (multiphoton) ionization probability of an individual spin-orbital according to

$$P_{i,\sigma} = 1 - N_{i,\sigma}(t), \quad (3.2.7)$$

where

$$N_{i,\sigma}(t) = \langle \psi_{i,\sigma}(t) | \psi_{i,\sigma}(t) \rangle, \quad (3.2.8)$$

is the time-dependent population (survival probability) of the $i\sigma$ -th spin-orbital.

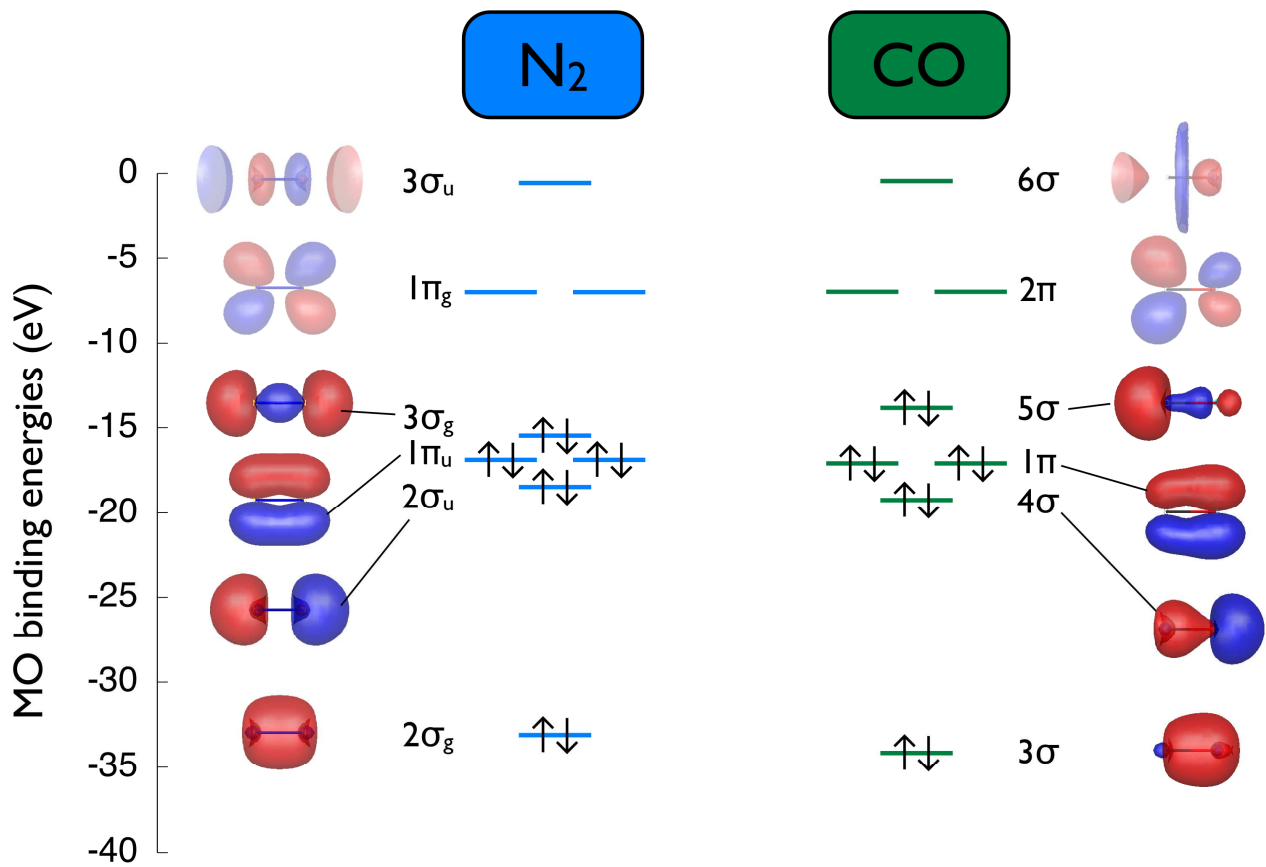


Figure 3.1: Molecular orbital binding energies and orbital structures for N_2 and CO molecules.

Figure 5.1 presents the time-dependent population of individual spin orbital, as defined in Eq. (3.2.8). The slope of the decay of the electron population in time determines the ionization rate. The laser (electric) field is assumed to be parallel to the internuclear axis, and the internuclear distance for the CO ($R_e = 2.132 a_0$) and N₂ ($R_e = 2.072 a_0$) molecules is fixed at its equilibrium distance R_e . Results for two laser intensities (5×10^{13} W/cm² and 1×10^{14} W/cm²) and a wavelength of 800 nm, 20-optical-cycle laser pulse are shown for CO and N₂.

The orbital structure and ionization potentials of the two molecules under consideration are close to each other (Fig. 3.1). That is why one can expect similar behavior in the laser field with the same wavelength and intensity. The multiphoton ionization in the laser field is dominated by HOMO, that is $3\sigma_g$ in N₂ and 5σ in CO. As one can see from Figs. 5.1(a) and 5.1(c), at lower intensity 5×10^{13} W/cm², the HOMO survival probabilities of N₂ and CO are close to each other. However, at higher intensities, the difference becomes more pronounced, at the intensity 1×10^{14} W/cm², the ionization probability of CO is much larger than that of N₂ (Figs. 5.1(b) and 5.1(d)). The explanation of the phenomenon can be as follows. In intense low-frequency laser fields, the multiphoton ionization occurs mainly in the tunneling regime. In this picture, the ionization takes place in the DC field with slowly varying amplitude from zero to its peak value. The width of the potential barrier depends on the field strength;

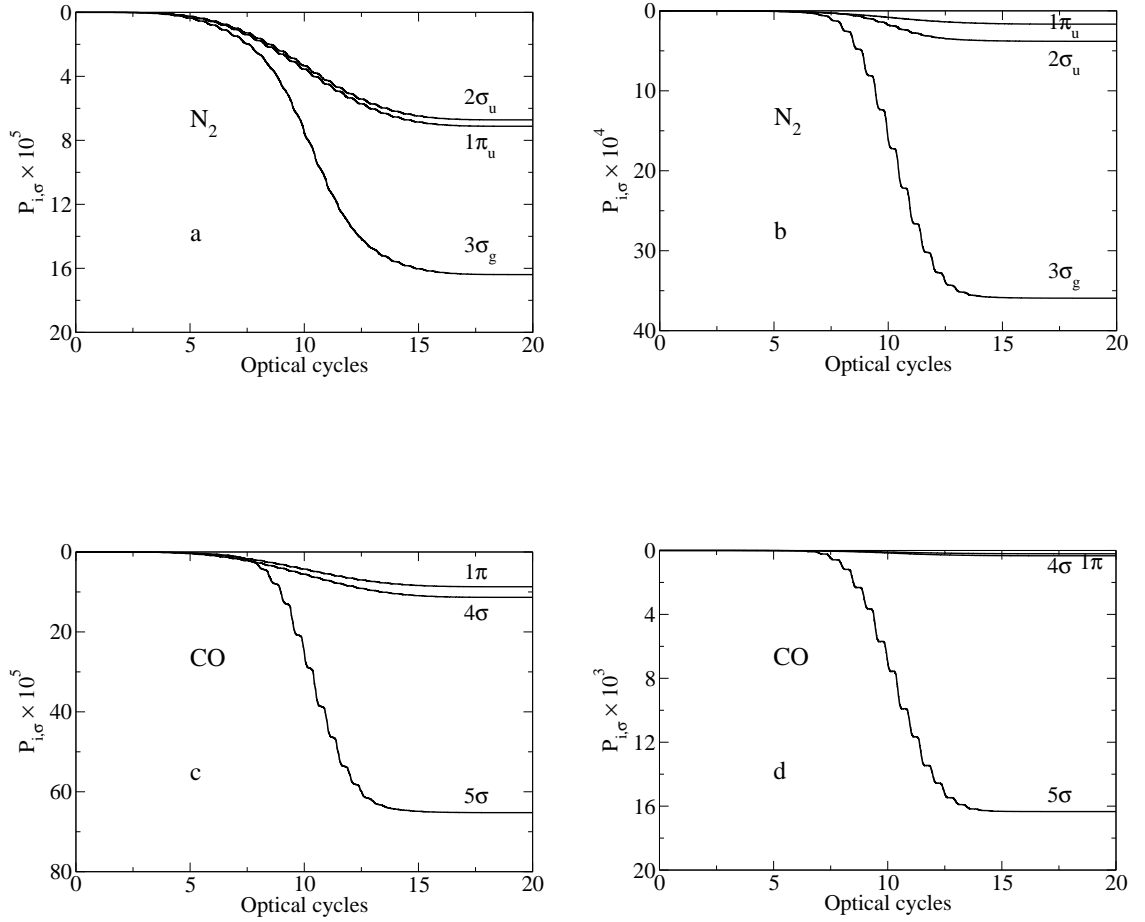


Figure 3.2: The time-dependent population of electrons in different spin orbital's of CO and N_2 in 800 nm, \sin^2 pulse laser field, with 20 optical cycles in pulse duration. N_2 molecule (a) $5 \times 10^{13} \text{ W/cm}^2$, (b) $1 \times 10^{14} \text{ W/cm}^2$, CO molecule (c) $5 \times 10^{13} \text{ W/cm}^2$, (d) $1 \times 10^{14} \text{ W/cm}^2$.

the stronger the field, the narrower the barrier. Thus the ionization occurs mainly at the peak values of the field strength. The probability of the tunneling ionization is very sensitive with respect to the HOMO energy. However, in the external field this energy is changed due to the Stark shift. The nitrogen molecule is symmetric with respect to inversion, that is why the Stark shift in the DC field is quadratic in the field strength and its value is quite small. On the contrary, the carbon monoxide molecule has a permanent dipole moment, and the DC Stark shift is linear in the field strength; at the peak values of the field, the HOMO energy can differ significantly from its unperturbed value. We have performed the self-consistent DFT calculations of N_2 and CO in the DC electric field parallel to the molecular axis to see how large the Stark shift can change the ionization potential of the molecule. On Table 3.2 we show the HOMO energies computed at the field strength 0.7549×10^{-2} a.u. which corresponds to the intensity 2×10^{12} W/cm². As one can see, even in the field as weak as 2×10^{12} W/cm², the shift of the HOMO energy in CO molecule is large. The shift depends on the direction of the external field with respect to the position of the carbon and oxygen nuclei. In one direction the energy level becomes higher, and in the other direction it becomes lower than the unperturbed level. Decrease of the binding energy will result in the enhanced ionization. In intense low-frequency laser fields, this effect can be responsible for the enhancement of ionization of CO molecule as compared with N_2 .

Table 3.2: HOMO energies of N₂ and CO molecules in DC electric field (positive field direction is from C to O)

Electric field (a.u.)	N ₂ HOMO energy (a.u.)	CO HOMO energy (a.u.)
0	-0.5682	-0.5086
0.7549×10^{-2}	-0.5681	-0.5149
-0.7549×10^{-2}	-0.5681	-0.5026

3.3 Multielectron Effects in HHG Spectra of Diatomic Molecules

In figures 5.2–5.3 we present the high-order harmonic generation (HHG) power spectra (HHG power, Eq. (3.2.6)) for the laser field intensities 5×10^{13} W/cm², and 1×10^{14} W/cm². An important difference between the N₂ and CO spectra is that the latter contain even as well as odd harmonics. Generation of even harmonics is forbidden in systems with inversion symmetry, such as atoms and homonuclear diatomic molecules. This selection rule does not apply to the heteronuclear molecules with no inversion center (CO). From Figs. 5.2–5.3, one can see that in general HHG is more efficient in CO than in N₂. However, for higher harmonics (17 and above) the N₂ spectra become dominant at the same laser intensity. As the laser intensity increases, the maximum in the power spectra is shifted towards higher harmonics.

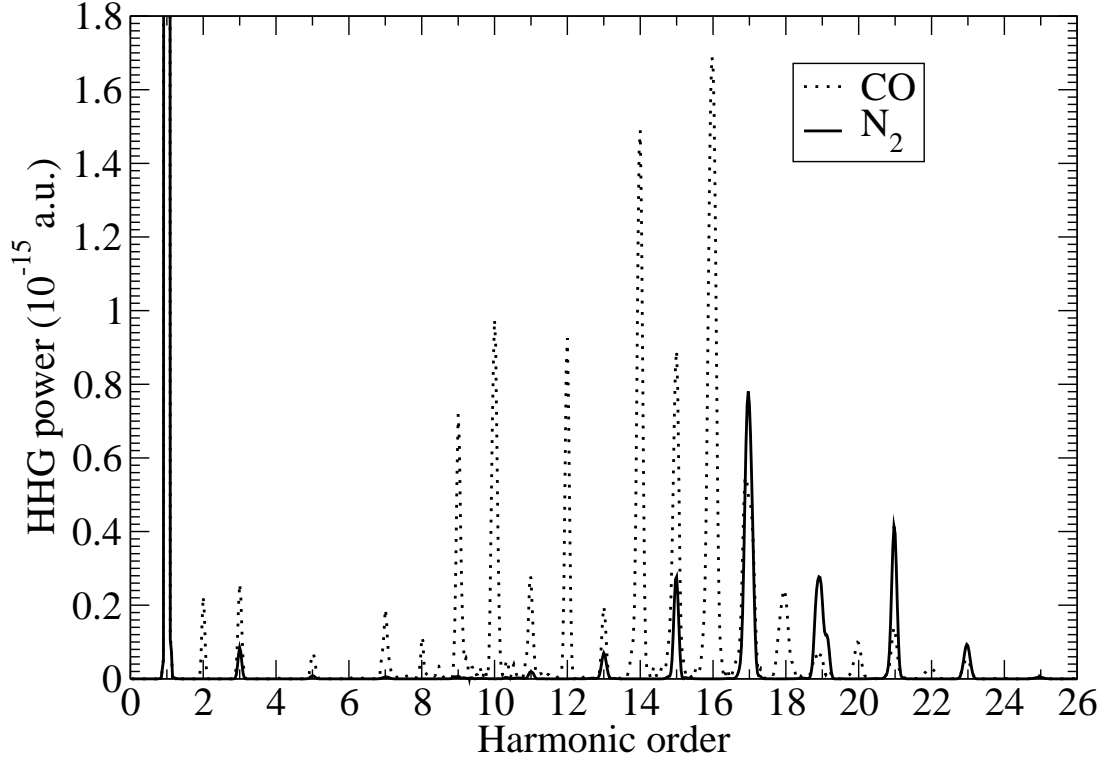


Figure 3.3: Comparison of the HHG power spectra of CO and N₂, in 800 nm, 5×10^{13} W/cm² sin² pulse laser field.

To investigate the detailed spectral and temporal structure of HHG for homonuclear and heteronuclear systems, we perform the time-frequency analysis by means of the wavelet transform of the total induced dipole moment $d(t)$ [64, 10, 30, 8, 4],

$$d_{\omega}(t) = \int d(t) \sqrt{\frac{\omega}{\tau}} e^{i\omega(t-t_0)} e^{-(\omega(t-t_0))^2/2\tau^2} dt. \quad (3.3.1)$$

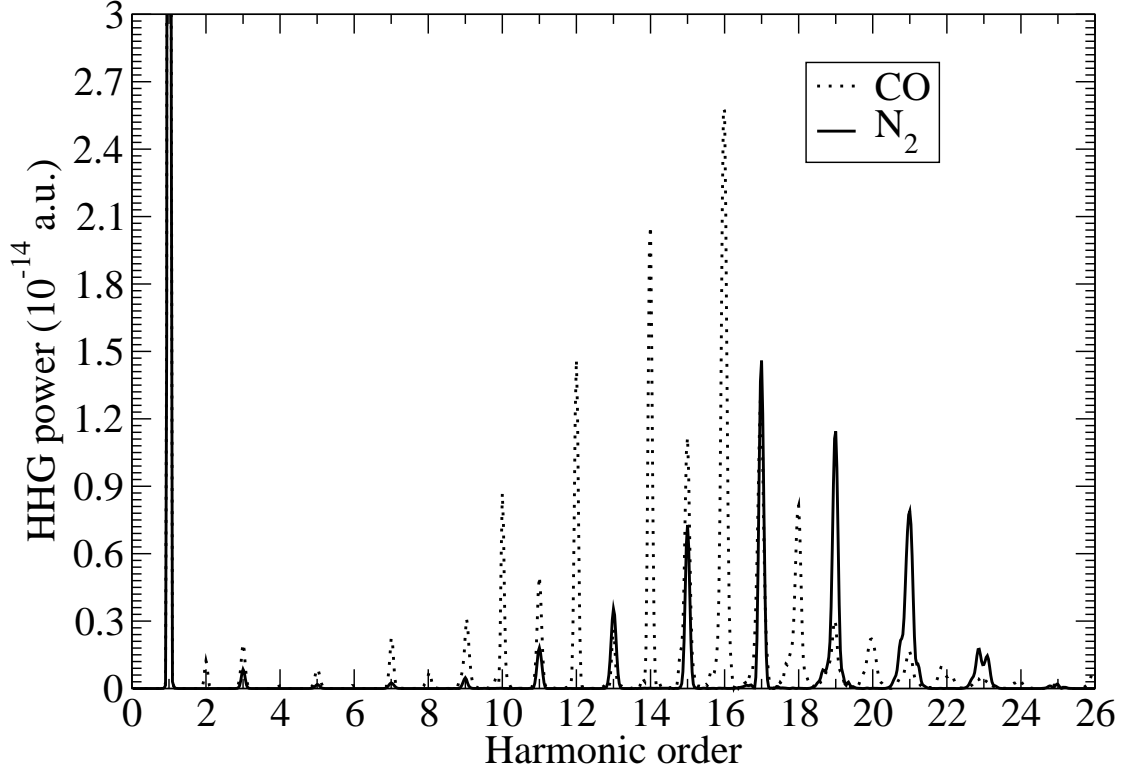


Figure 3.4: Comparison of the HHG power spectra of CO and N₂, in 800 nm, 1×10^{14} W/cm² sin² pulse laser field.

The parameter $\tau = 15$ is chosen to perform the wavelet transformation in the following study.

The peak emission times, t_e , represent the instance when the maxima of the dipole time profile occur, and semiclassically are interpreted as the electron-ion recollision times [64, 30]. For the case of the N₂ molecule, the time profiles of the 19th to 25th harmonic orders are shown in Fig. 5.4(a).

There are two emissions occurring at each optical cycle, and the most prominent bursts take place at the center of the laser field envelope. The time profiles of the

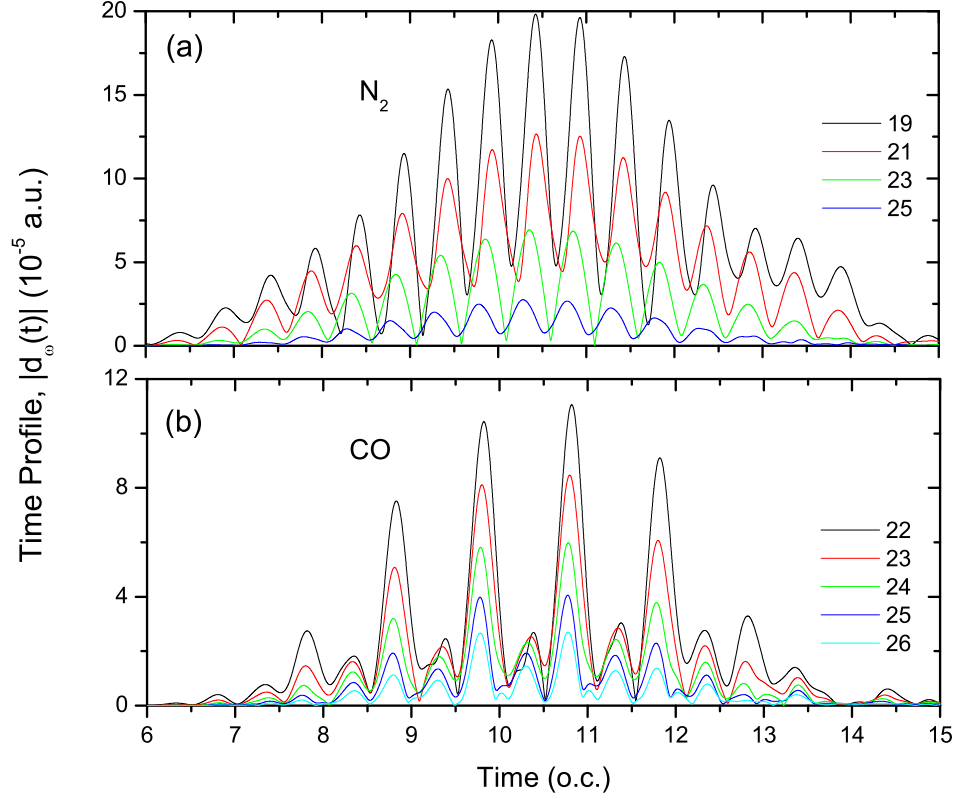


Figure 3.5: Time profiles for (a) N_2 and (b) CO . Laser intensity used is $5 \times 10^{13} \text{ W/cm}^2$, wavelength used is 800 nm, with 20 optical cycles in pulse duration.

superimposed harmonics are rather uniform among themselves implicating that the harmonics are partially synchronized. More importantly for the CO molecule, a distinct feature possibly characteristic of all heteronuclear diatomic systems is observed in Fig. 5.4(b) for the harmonic orders 22^{th} to 26^{th} . The number of dominant emissions per optical cycle is now limited to only one. This finding is in contrast with results normally obtained in the HHG for atoms and homogeneous molecules in which two

bursts per optical cycle are observed. The spectral profiles are as uniform as those obtained for N_2 , though the CO harmonics appear to be more synchronized than those of N_2 . For the CO molecule, the highest occupied molecular orbital (HOMO) (5σ) is dominant for the whole HHG spectrum Fig. 3.6; other orbitals contribute much less.

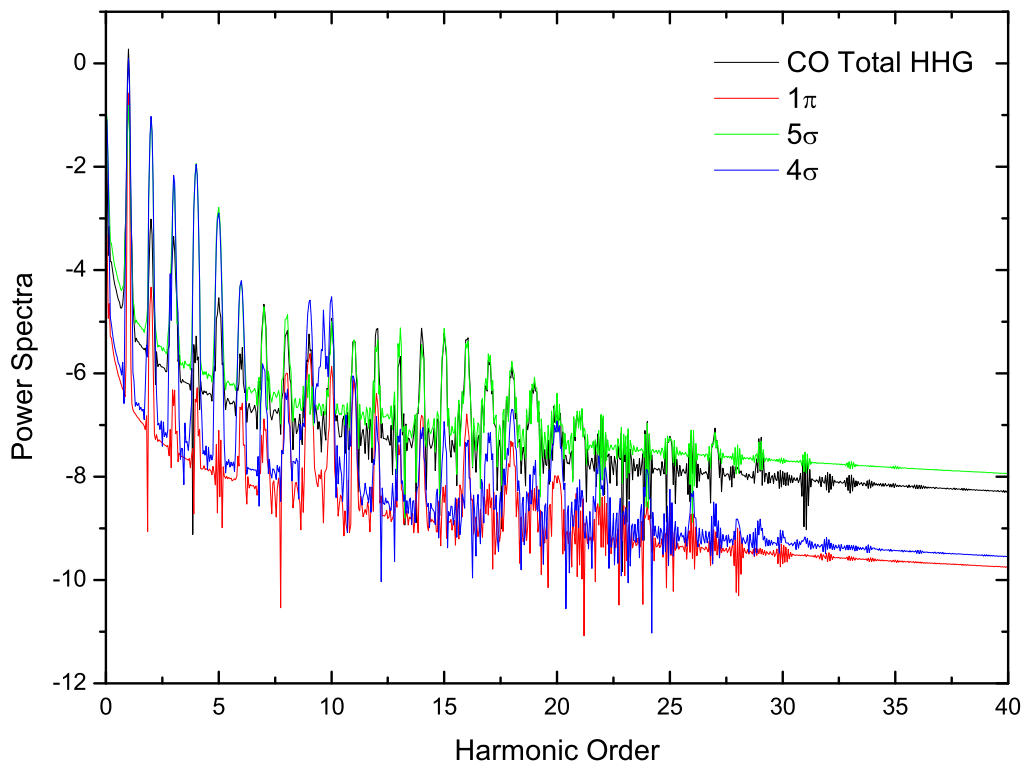


Figure 3.6: Individual orbital and total high-order harmonic generation power spectra of CO at the peak intensity $1 \times 10^{14} \text{ W/cm}^2$ with a laser frequency of 800 nm. .

The distinct harmonic peaks are seen up to the order 30, then we can see just a smooth background distribution. In CO, the 5σ dipole is +1.57 which is much larger than any of the other orbitals. The density for the 5σ (and 2σ) is localized on the carbon atom, all other orbitals the density is localized on the oxygen atom. Looking at the orbital dipole's for the CO molecule Fig. 3.7, we can see that all other orbitals that are localized on the oxygen are in phase and 5σ (carbon) is out of phase in time.

The N_2 molecule has a dipole amplitude that follows the trend:

$$d_{2\sigma_g} < d_{1\pi_u} < d_{total} < d_{3\sigma_g} < d_{2\sigma_u}$$

The orbital dipole moments $2\sigma_g$, $1\pi_u$, and $2\sigma_u$ are oscillating as that of the total dipole, the $3\sigma_g$ (out of phase). So when we look at the two orbital dipole amplitudes $2\sigma_u$ and $3\sigma_g$ with similar amplitudes, they oscillate in time with different sign, canceling each other out Fig. 3.8, leading to a smaller dipole.

The behavior of the HHG spectrum Fig. 3.9 for N_2 is quite different. The HOMO ($3\sigma_g$) is dominant in the middle part of the spectrum (again up to the order 31).

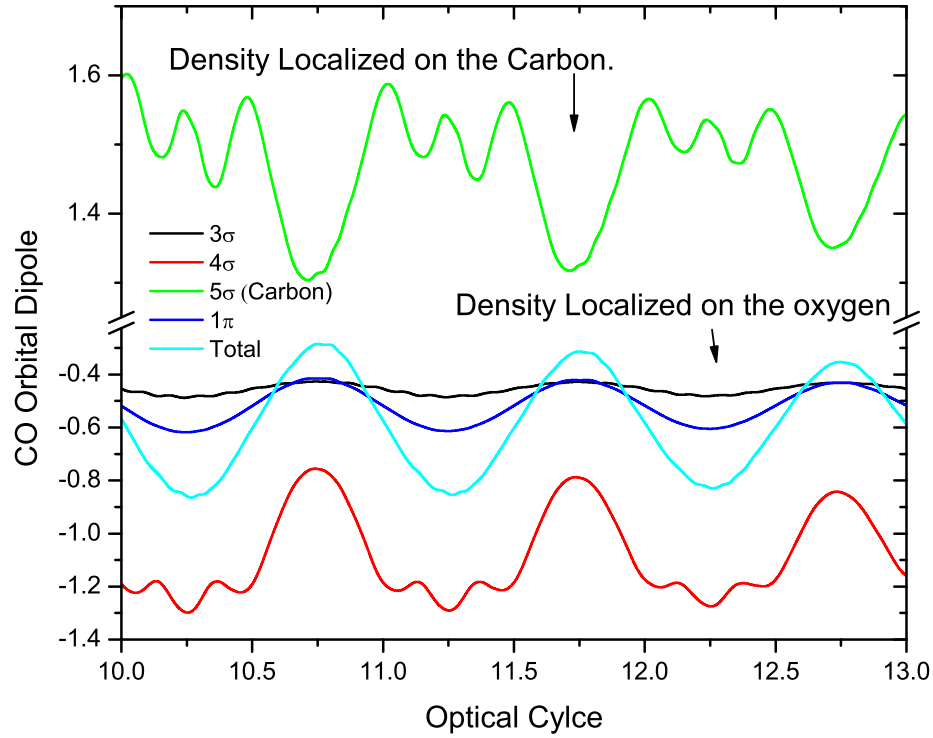


Figure 3.7: Orbital dipole moments of CO at the peak intensity $1 \times 10^{14} \text{ W/cm}^2$ with a laser frequency of 800 nm for 3 optical cycles (10 – 13).

However, starting the 33th harmonic, the $2\sigma_u$ orbital has a comparable contribution which interferes destructively with that of $3\sigma_g$.

Thus the result of interference is much lower than both of the single orbital spectra. Then this two-orbital spectrum becomes comparable in magnitude with the $2\sigma_g$ -only HHG (shown in Fig 3.10). Again, the destructive interference takes place, and the

result is much lower than any of the single orbital contributions.

We can say that the long HHG spectrum of N_2 is a collective multielectron effect. Destructive interference of orbital contributions makes the resulting spectrum lower in amplitude with distinct harmonic peaks up to the order 47. Note that single orbital HHG do not have distinct peaks, just a smooth background, so the peaks in the high harmonic part of the total HHG spectra are the pure multielectron interference effect. We think this happens to N_2 and does not happen to CO, because of the broken g-u symmetry in CO such a full interference is not possible. The induced dipole moment of the HOMO 5σ (CO) is so large that no other orbital can make a comparable contribution.

3.4 Conclusion

In this chapter, we present a detailed comparison of the very high-order nonlinear optical response of the homonuclear N_2 and heteronuclear CO diatomic molecules in intense ultrashort laser fields by means of a TDDFT with correct asymptotic long-range $(-1/r)$ potential to ensure individual spin-orbital has the proper ionization potential. We consider only the case that the molecular axis is aligned with the laser beam direction. This is justified based on the recent experimental development of

the laser molecular alignment techniques [40, 54, 48, 49]. We found that although CO has only a very small permanent dipole moment, qualitatively different nonlinear optical responses are predicted for CO and N₂. First, the MPI rate for the heteronuclear diatomic CO molecules is larger than that for the N₂ homonuclear diatomic molecules. Second, while the laser excitation of the N₂ molecules can generate only odd harmonics, both even and odd harmonics can be produced for the CO case. To our knowledge, this is the first *all-electron* TDDFT study of the generation of even harmonics for the heteronuclear diatomic molecules. In this connection, we note that the even-order harmonics were also predicted in an earlier study of the HHG of a one-dimensional model HD with unequal nuclear mass [38]. In this model, even-order harmonics can be produced only by means of the breakdown of the Born-Oppenheimer approximation. However, in our *ab initio* 3D study of CO with unequal nuclear mass and charge, even-order harmonics can still be produced when the internuclear separation is fixed. Third, from our wavelet time-frequency analysis, we found that there are two dominant rescattering (and harmonic emission) events within each optical cycle for the N₂ molecules, while there is only one dominant rescattering event for the CO molecules. Much remains to be explored in this fascinating and largely unexplored area of strong-field molecular physics. Finally, the nuclear degree of freedom has not been taken into account so far. This is justified for ultrashort laser pulse excitation. Research in this direction will be pursued in the future.

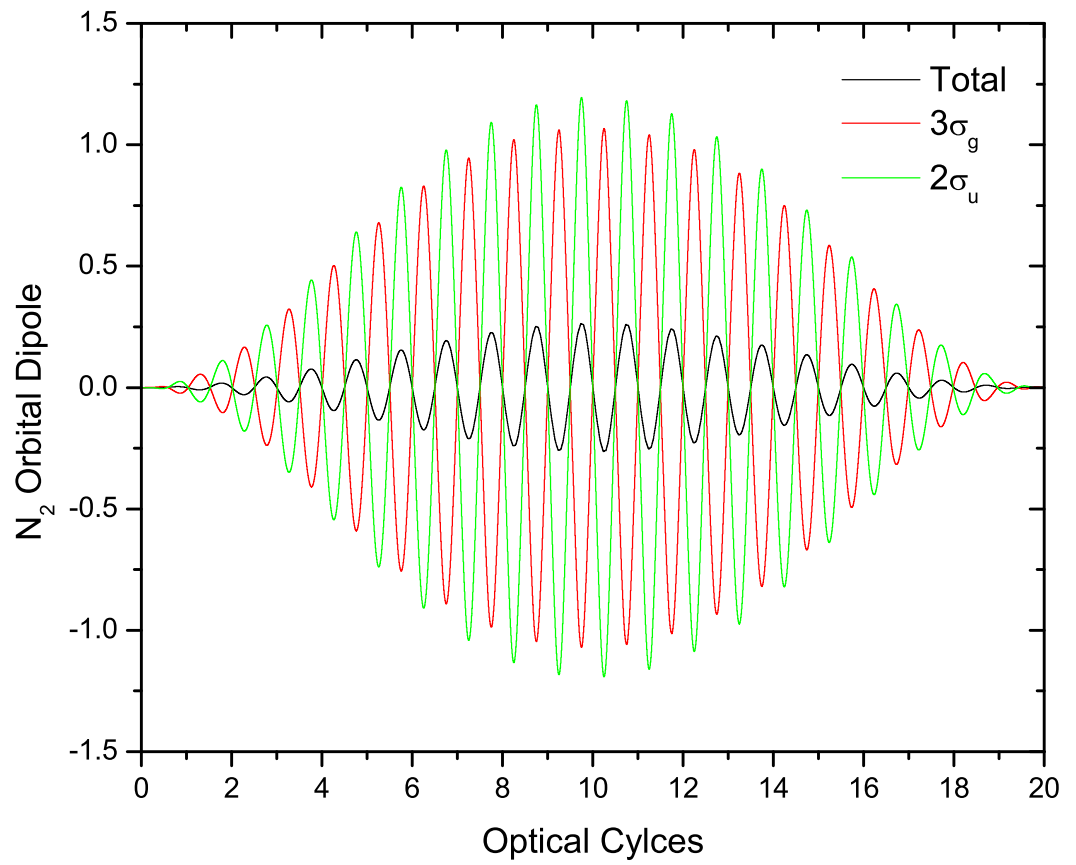


Figure 3.8: Orbital dipole moments (total, $3\sigma_g$, and $2\sigma_u$) of N_2 at the peak intensity $1 \times 10^{14} \text{ W/cm}^2$ with a laser frequency of 800 nm for 20 optical cycles.

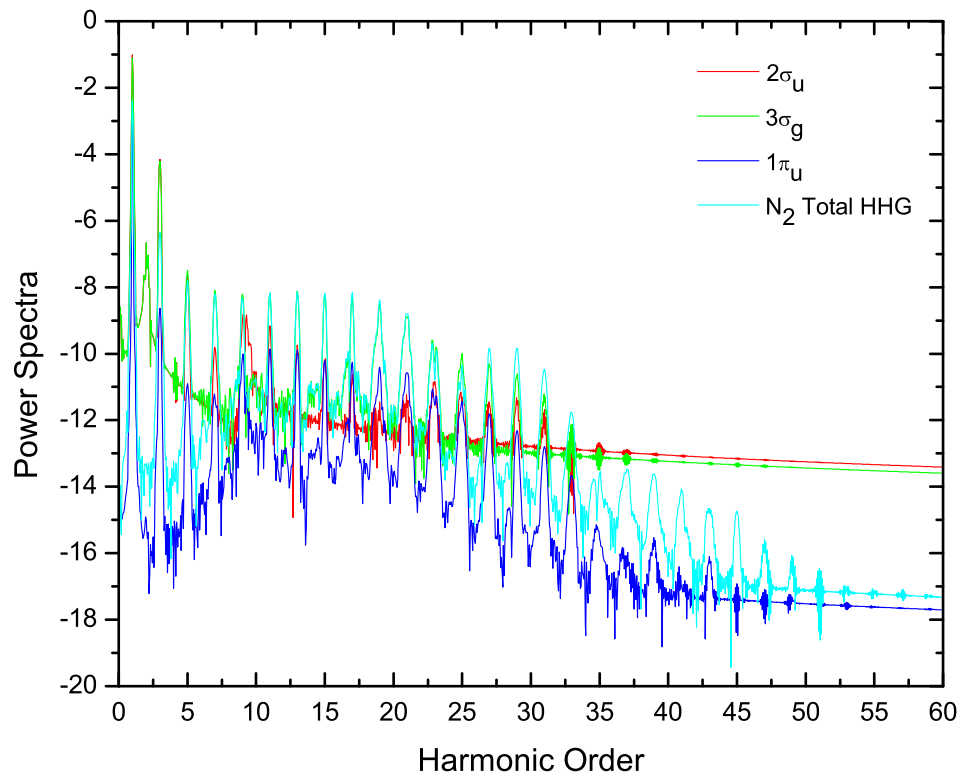


Figure 3.9: Individual and total orbital high-order harmonic generation power spectra of N₂ at the peak intensity 1×10^{14} W/cm² with a laser frequency of 800 nm. .

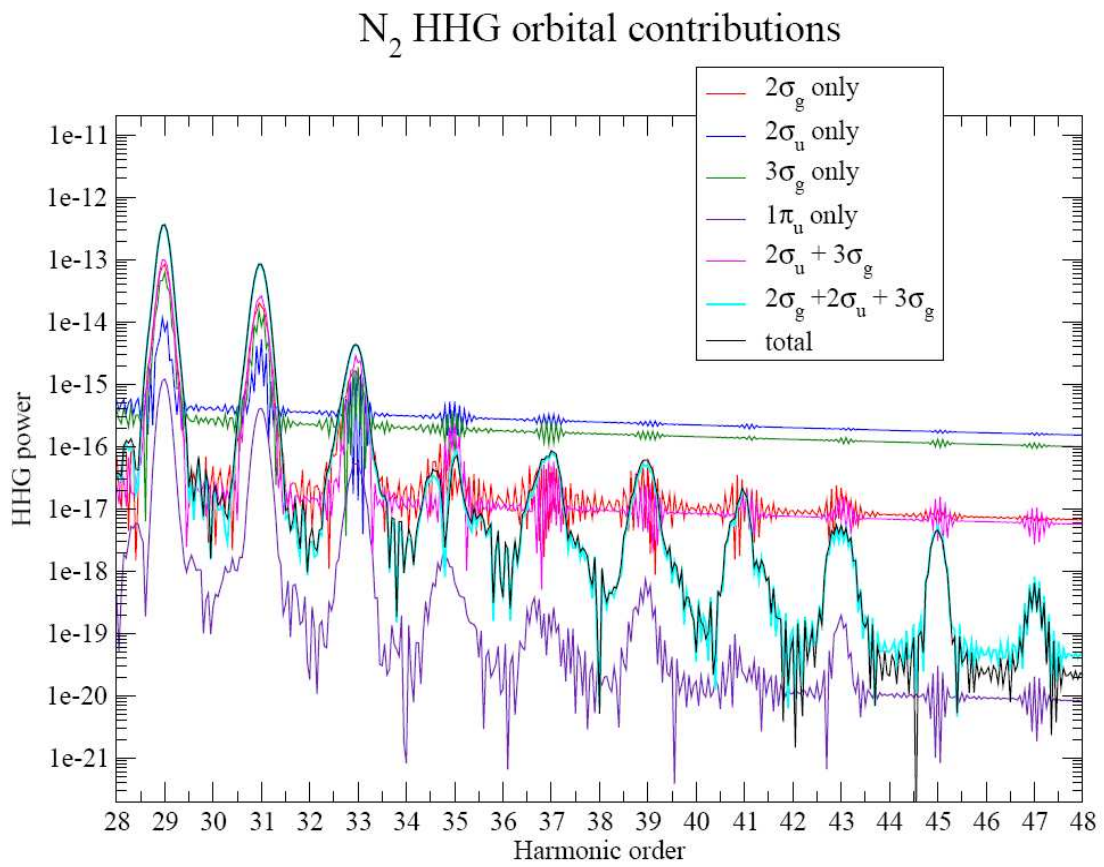


Figure 3.10: Individual and orbital interference power spectra of N_2 at the peak intensity $1 \times 10^{14} \text{ W/cm}^2$ with a laser frequency of 800 nm. .

Chapter 4

Ab Initio Study of High-Lying Doubly Excited States of Helium in Static Electric Fields

4.1 Introduction

The helium atom is the simplest two-electron three-body system that has been studied extensively both theoretically and experimentally since the first experiment by Maden and Codling on doubly excited states in 1963 [42]. From an excitation energy of 57 eV to the $\text{He}^+ N = 2$ threshold at 65.4 eV, the spectrum of helium contains a number of Rydberg series of autoionizing states embedded in the $\text{He}^+ 1s\epsilon l$ continuum. Due to the existence of strong electron-electron correlation, higher members of the Rydberg series cannot be described by the single-configuration or mean field approximation. Numerous theoretical investigations have improved our understanding of the

e-e correlation and the determination of the autoionizing resonances of the double excited states of He in the last few decades [55]. In addition to fundamental interest, the energies, lifetimes, and oscillator strengths of these doubly excited resonance states are also of significance in astrophysics and plasma physics [23]. More recently there is considerable interest in the study of the effect of static electric fields on doubly excited states of helium atoms below $N = 2$ threshold [21, 22, 20, 51, 77, 44].

The first observation of the effect of dc electric field on the photoexcitation spectrum of He doubly excited states was performed by Harries et al [20] who measured the Stark shifts and splittings in strong dc fields (up to 84.4 kV/cm) in the region of the $6a - 8a \ ^1P^o$ resonances below $N = 2$. Most theoretical works in the recent past have dealt with dc fields on this strong field regime [24, 14, 66]. With the exception of the dipole allowed $^1P^o$ states, most predicted doubly excited states of He are not accessible by simple photoabsorption. In the presence of external dc electric fields, these dark states becomes accessible by means of the Stark mixing with the $^1P^o$ states. For example, the even $^1P^e$ series of doubly excited states have been recently observed and measured [21, 22] in weak dc electric fields ($F < 10$ kV/cm). In addition, dramatic electric field effect has been also reported in the fluorescence yield spectrum of the doubly excited states in He in weak electric dc field regime (~ 1 kV/cm) [51] for higher quantum number $n \leq 15$. To our knowledge, however, nonperturbative theoretical investigation of the effect of dc electric field on the high-lying doubly excited

resonance states ($n > 10$) is not yet currently available.

To advance this field, we present in this chapter a new computational method, the complex-scaling generalized pseudospectral (CSGPS) method in hyperspherical coordinates (HSC), for efficient and accurate nonperturbative calculation of high-lying doubly excited states of He ($n = 10 - 20$) in the presence of weak and strong dc electric fields below $N = 2$. Comparison with available experimental data is made. In addition, we also present the energies and widths of field-free doubly excited resonance states of He for n up to 20.

The chapter is organized as follows. First, we present the detailed CS-GPS-HSC procedure for accurate treatment of quantum dynamics in two-electron systems. Next, we present the calculations of the doubly excited states and effects of dc electric field on the high-lying doubly excited resonance states. Exploration of the effects of electron correlation and doubly excited states in dc electric field are discussed in detail.

4.2 Complex-Scaling Generalized Pseudospectral Method in Hyperspherical Coordinates

The complex-scaling generalized pseudospectral (CSGPS) method was first introduced in 1993 for the study of atomic resonance states [76, 73] in grid representation.

It has been later extended and extensively used for the accurate treatment of multi-photon above-threshold ionization (ATI) and high-order harmonic generation (HHG) of atomic [56] and diatomic molecular [56, 12, 10, 11, 57, 58, 30] systems in intense laser fields in the last decade, in conjunction with the development of non-Hermitian Floquet formalisms and self-interaction-free time-dependent density functional theory [9]. The CSGPS approach employs the use of non-uniform and optimal spatial grid discretization of the coordinates and Hamiltonian, allowing high-precision and efficient calculation of complex quasi-energy eigenvalues and eigenfunctions and ATI/HHG rates with the use of only a very modest number of grid points.

In this section, we present the extension of the CSGPS method in the framework of hyperspherical coordinates (HSC) for the ab initio treatment of doubly excited resonance states of the two-electron atomic systems. We note that time-dependent generalized pseudospectral (TD-GPS) method in HSC, without the use of complex scaling transformation, has been recently developed for the treatment of double photoexcitation of He atoms in weak attosecond xuv pulses [67] and the effect of electron correlation on high-order-harmonic generation (HHG) of helium atoms in intense laser fields [26].

We first briefly outline the essence of GPS-HSC formalism [26] without the use of complex scaling transformation. The Schrödinger equation for the field-free He atoms is given by, in atomic units,

$$\left[-\frac{1}{2}\nabla_1^2 - \frac{1}{2}\nabla_2^2 - \frac{2}{r_1} - \frac{2}{r_2} + \frac{1}{|\mathbf{r}_1 - \mathbf{r}_2|} - E \right] \psi(\mathbf{r}_1, \mathbf{r}_2) = 0. \quad (4.2.1)$$

In the HSC, Eq. (4.2.1) can be reduced to the form [26]

$$\left[-\frac{1}{2} \frac{\partial^2}{\partial R^2} - \frac{1}{8R^2} + \frac{1}{2R^2} \left(-\frac{\partial^2}{\partial \alpha^2} + \frac{\hat{l}_1^2}{\cos^2 \alpha} + \frac{\hat{l}_2^2}{\sin^2 \alpha} \right) + \frac{C}{R} \right] \Psi = E\Psi, \quad (4.2.2)$$

where $R = \sqrt{r_1^2 + r_2^2}$ is the hyperradius, and $\alpha = \tan^{-1}(r_2/r_1)$ is the hyperangle, and the potential energy term C is the electron-electron and electron-nucleus potentials, given by

$$C(\alpha, \theta_{12}) = \frac{2Z}{\cos \alpha} + \frac{2Z}{\sin \alpha} - \frac{2}{\sqrt{1 - \sin 2\alpha \cos \theta_{12}}}. \quad (4.2.3)$$

In the HSC, the two vectors $(\mathbf{r}_1, \mathbf{r}_2)$ are replaced by the six coordinates $(R, \alpha, \Omega_1, \Omega_2)$, where $\Omega_i = (\theta_i, \phi_i)$ denotes the spherical angles of electron i .

In the CSGPS approach in HSC, only the hyperradius coordinate R needs to be complex rotated [75], namely,

$$R \rightarrow Re^{i\theta}, \quad (4.2.4)$$

where θ is the rotation angle. We perform next the algebraic mapping from R to x and from α to y :

$$R(x) = L \frac{1+x}{1-x+\gamma} e^{i\theta}, \quad (4.2.5)$$

$$\alpha(y) = \frac{\pi}{4}(1+y), \quad (4.2.6)$$

where $\gamma = 2L/R_{max}$ and $x \in [-1, 1]$, $y \in [-1, 1]$, $R \in [0, R_{max}]$, $\alpha \in [0, \pi/2]$, and L is the mapping parameter. The given space that the two electrons are confined to is determined by the size of R_{max} , and the mapping parameter controls the linear position of the mesh points [76].

Under the complex-scaling transformation, Eq. (4.2.2)

$$\left[-\frac{e^{-i2\theta}}{2} \frac{\partial^2}{\partial R^2} - \frac{e^{-i2\theta}}{8R^2} + \frac{e^{-i2\theta}}{2R^2} \left(-\frac{\partial^2}{\partial \alpha^2} + \frac{\hat{l}_1^2}{\cos^2 \alpha} + \frac{\hat{l}_2^2}{\sin^2 \alpha} \right) + \frac{Ce^{-i\theta}}{R} \right] \Psi(Re^{i\theta}, \alpha, \Omega_1, \Omega_2) = \epsilon \Psi(Re^{i\theta}, \alpha, \Omega_1, \Omega_2), \quad (4.2.7)$$

where ϵ denotes the complex energies of the autoionizing resonance states. We expand the total two-electron wavefunction Ψ in terms of the complex-scaled adiabatic channels μ ,

$$\Psi(Re^{i\theta}, \alpha, \Omega_1, \Omega_2) = \frac{e^{-i\frac{5}{2}\theta}}{R^{\frac{5}{2}} \sin \alpha \cos \alpha} \sum_{\mu} F_{\mu}(Re^{i\theta}) \Phi_{\mu}(Re^{i\theta}, \alpha, \Omega_1, \Omega_2), \quad (4.2.8)$$

where $F_{\mu}(Re^{i\theta})$ is to be solved in the hyperradius space and the adiabatic channel functions $\Phi_{\mu}(Re^{i\theta}, \alpha, \Omega_1, \Omega_2)$ describe the radial correlation between the two electrons [59]. These channel functions are obtained by solving the adiabatic Hamiltonian [26] at a fixed value of R ,

$$H_{ad} \Phi_{\mu}(Re^{i\theta}, \alpha, \Omega_1, \Omega_2) = U_{\mu}(Re^{i\theta}) \Phi_{\mu}(Re^{i\theta}, \alpha, \Omega_1, \Omega_2). \quad (4.2.9)$$

Here the channel functions $\Phi_{\mu}(Re^{i\theta}, \alpha, \Omega_1, \Omega_2)$ can be represented in a way to satisfy

the exchange symmetry $^{2S+1}L^\pi$, either singlet or triplet states, and are expanded in terms of two-particle spherical harmonics. For fixed L , M , S , and π , we have

$$\Phi_\mu^{L,l_1,l_2}(Re^{i\theta}, \alpha, \Omega_1, \Omega_2) = \begin{cases} \frac{1}{\sqrt{2}} \sum_{l_1 l_2} [f_\mu^{L,l_1,l_2}(Re^{i\theta}, \alpha) \mathcal{Y}_{l_1,l_2}^{LM}(\Omega_1, \Omega_2) \\ + (-1)^A f_\mu^{L,l_2,l_1}(Re^{i\theta}, \frac{\pi}{2} - \alpha) \mathcal{Y}_{l_2,l_1}^{LM}(\Omega_1, \Omega_2)] , & l_1 \neq l_2 \\ \sum_{l_1 l_2} f_\mu^{L,l_1,l_2}(Re^{i\theta}, \alpha) \mathcal{Y}_{l_1,l_2}^{LM}(\Omega_1, \Omega_2), & l_1 = l_2, \end{cases} \quad (4.2.10)$$

where we define $A = l_1 + l_2 - L + S$. L and S indicate the total orbital and spin angular momenta respectively. In Eq. (4.2.10) the coefficients $f_\mu(Re^{i\theta}, \alpha)$ are the Gauss-Legendre quadratures.

Once the adiabatic eigenvalue problem is solved we then use these complex-scaled channel functions to compute the coupling terms [59], hence the overlap matrix

$$\mathcal{O}_{i\mu,j\mu'} = \langle \Phi_\mu(R_i e^{i\theta}, \alpha, \Omega_1, \Omega_2) | \Phi_{\mu'}(R_j e^{i\theta}, \alpha, \Omega_1, \Omega_2) \rangle. \quad (4.2.11)$$

After mapping the domain of the total wavefunction Eq. (4.2.8), we obtain the following transformation:

$$\begin{aligned} \Psi(Re^{i\theta}, \alpha, \Omega_1, \Omega_2) &= \sqrt{R'(x)} \sum_{i=1}^{N_R} f_i(xe^{i\theta}) \Psi(x_i e^{i\theta}, y, \Omega_1, \Omega_2) \\ &= \sqrt{R'(x)} \sum_{i\mu}^{N_R N_\mu} f_i(xe^{i\theta}) C_{i\mu} \Phi(x_i e^{i\theta}, y, \Omega_1, \Omega_2) \end{aligned} \quad (4.2.12)$$

Inserting the discretized representation of the complex-scaled wavefunction Eq. (4.2.12) into Eq. (4.2.7), we can rewrite the discretized Schrödinger equation in the form

$$\begin{aligned} \sum_{i'\mu'} [\mathcal{K}(Re^{i\theta})_{ii'} \mathcal{O}_{i\mu, i'\mu'} + \delta_{ii'} U_{\mu'}^L(R_i e^{i\theta}) \mathcal{O}_{i\mu, i'\mu'}] C_{i\mu} \\ = \epsilon \sum_{i'\mu'} \mathcal{O}_{i\mu, i'\mu'} C_{i\mu}, \end{aligned} \quad (4.2.13)$$

where $\mathcal{K}(Re^{i\theta})_{ii'}$ is the complex-scaled kinetic energy matrix elements and $U_{\mu'}^L(R_i e^{i\theta})$ is the eigenenergy at fixed R_i , and corresponding L and μ .

The first advantage in the present CSGPS-HSC procedure is in that the GPS method is a nonlinear grid discretization method. This ensures that the short-range part of the Coulomb interaction is properly represented. Therefore, a dense portion of grid points are concentrated at the origin. The second advantage, is that in the CS-GPS approach the complex-rotated coordinate R is discretized on a set of collocation grid points. The potential matrix elements being diagonal, and equal to the values of the potential at the grid points. The kinetic energy matrix elements $\mathcal{K}(Re^{i\theta})_{ii'}$ in Eq. (4.2.13) have simple explicit analytical expressions.

As an example of the accuracy of the present GPS procedure, Fig. 4.1 shows the first fifteen adiabatic potential curves of helium in the singlet $^1S^e$, $^1P^o$, $^1D^e$, and $^1F^o$ ($L = 0-3$) manifolds converging to the He^+ ionization thresholds. We note that there is a number of avoided crossings even between the low-lying neighboring potential curves. For example, a sharply avoided crossing point in the $1P^o$ manifold occurs around the hyperradius of 7.63 a.u and in the $1D^e$ manifold occurs around the

hyperradius of 5.97 a.u.

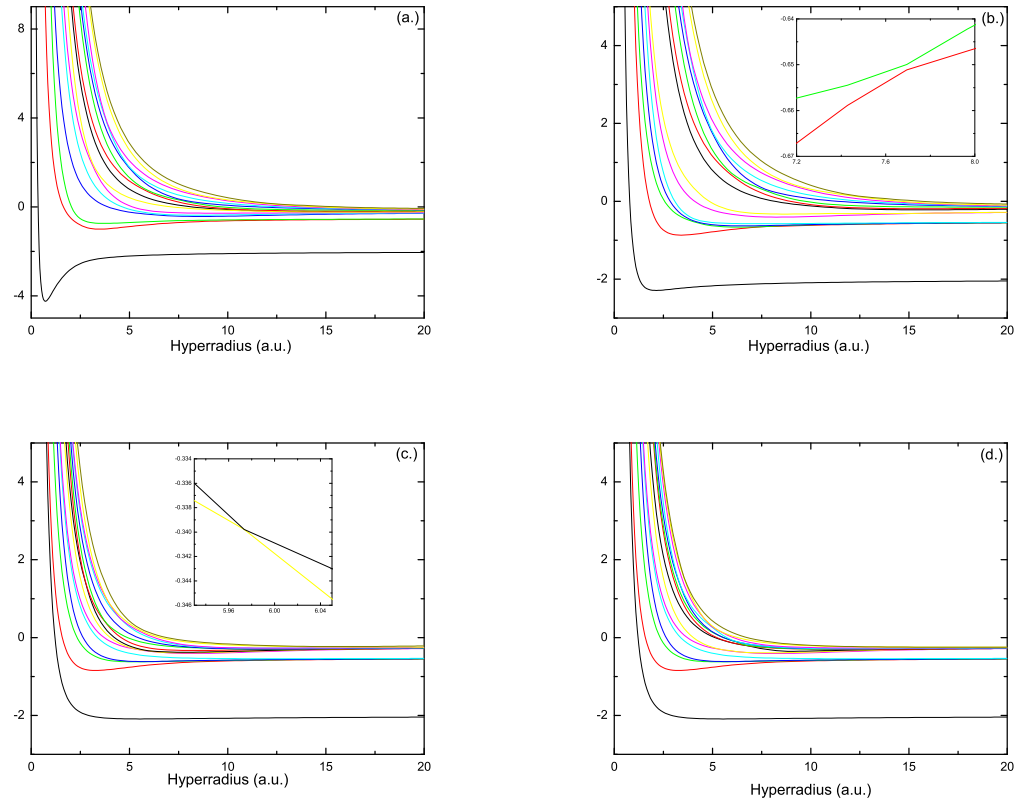


Figure 4.1: Potential curves of the helium atom for (a) $1S^e$, (b) $1P^o$, (c) $1D^e$, and (d) $1F^o$ manifolds.

4.3 Determination of the Doubly Excited Autoionizing Resonances

To illustrate the accuracy of the present method, we list the energies and widths for He doubly excited Rydberg states $n = 10 - 20$ below the $N = 2$ threshold. In Tables 4.1-4.4, we compare our results of $^1S^e$, $^1P^o$, $^1D^e$ and $^1F^o$ with recent theoretical results [43, 3, 35]. The present calculations listed in Tables 4.1-4.4 compared to the previous theoretical results for the doubly excited states where $n = 10 - 15$ which generally agree well. In the present calculation doubly excited Rydberg states are calculated to the $n = 20$ state. Since there is no theoretical or experimental data to our knowledge to compare the high-lying Rydberg states $n = 15 - 20$, we expect experimental measurements of these in the future. Throughout this chapter we use the $(N, n, (a, b, \text{ or } c))$ representation for doubly excited states introduced by Lipsky [41], which is widely used for He.

In Table 4.1 both singlet symmetries of the $^1S^e$ states are calculated, hence $(2, n, a)$ and $(2, n, b)$ where $n = 10 - 20$. In the $^1S^e$ calculation fifteen partial waves are used, (l_1, l_2) , with $R_{max} = 1000$ a.u. In Table 4.2 three singlet symmetries of the $^1P^o$ states are calculated, hence $(2, n, a)$, $(2, n, b)$, and $(2, n, c)$ where $n = 10 - 20$. In the $^1P^o$ calculation twenty partial waves are used, (l_1, l_2) , with $R_{max} = 1200$ a.u. In Table 4.3 three singlet symmetry of the $^1D^e$ state is calculated, hence $(2, n, a)$, $(2, n, b)$, and

$(2, n, c)$ where $n = 10 - 20$. In the $^1D^e$ calculation twenty partial waves are used, (l_1, l_2) , with $R_{max} = 1500$ a.u. In the $^1F^o$ calculation twenty partial waves are used, (l_1, l_2) , with $R_{max} = 2500$ a.u. In all of the previous calculations by use of the highly accurate CSGPS-HSC procedure resonance energies are converged to 10^{-9} a.u. and the widths are converged to 10^{-4} a.u.

Tables 4.1-4.4 shows the resonance energies converging to the He^+ ionization thresholds (-0.5 a.u.). One of the appealing features revealed from Tables 4.1-4.4 is the common trend of the autoionization rates decreasing as a function of the quantum number n increasing (Fig. 4.2), this common trend is shown in all states. This is due to the singlet continuum states $1s\epsilon l$ coupling with the doubly excited states $2snl$. Since the doubly excited states are embedded with the singlet continuum states. The widths are proportional to the coupling strengths between these states (*i.e.*, $\Gamma \propto |\langle \Psi_{1s\epsilon l} | 1/r_{12} | \Psi_{2snl} \rangle|^2$). As the quantum number n is increased the two electrons are getting further and further apart from each other. Therefore, making r_{12} larger, and thus decreasing the autoionization rates. For example, we can look at the widths from the $^1P^o$ states, $10a$ being 4.052×10^{-6} and the high-lying $20a$ being 4.859×10^{-7} .

Such accuracy for Rydberg resonant energies by the CSGPS-HSC procedure cannot be achieved by traditional basis set expansion methods or B-spline functions.

4.4 Determination of the DC Field Effects on the Doubly Excited Resonance States

In the presence of an external electric-field, the Hamiltonian for a two-electron atom is

$$H = H_0 + V = H_0 + \mathbf{F} \cdot (\mathbf{r}_1 + \mathbf{r}_2) \quad (4.4.1)$$

where \mathbf{F} is a uniform external electric-field. H_0 is the field-free Hamiltonian. The matrix elements of Fz_1 and Fz_2 are the same for a given pair of wavefunctions. Here we only present the matrix element of Fz_1 explicitly as follows:

$$\begin{aligned} \langle \Psi_k^L | F(z_1) | \Psi_{k'}^{L'} \rangle &= \frac{1}{2} \cdot F \cdot \sum_{\mu, \mu'} \sum_{l_1, l_2} \sum_{l'_1, l'_2} \left[\sum_i F^L(R_i e^{i\theta}) \cdot R_i e^{i\theta} \cdot F^{L'}(R_i e^{i\theta}) \omega_i \right] \\ &\times \left\{ \sum_j \Phi_\mu^{l_1 l_2 L}(R_i e^{i\theta}, \alpha_j) \cdot \cos \alpha_j \cdot \Phi_{\mu'}^{l'_1 l'_2 L'}(R_i e^{i\theta}, \alpha_j) \lambda_j \Theta_{l_1 l_2 L M}^{l'_1 l'_2 L' M'} \right. \\ &+ (-1)^A \sum_j \Phi_\mu^{l_1 l_2 L}(R_i e^{i\theta}, \pi/2 - \alpha_j) \cdot \cos \alpha_j \\ &\left. \times \Phi_{\mu'}^{l'_1 l'_2 L'}(R_i e^{i\theta}, \alpha_j) \lambda_j \Theta_{l_2 l_1 L M}^{l'_1 l'_2 L' M'} \right\}, \end{aligned} \quad (4.4.2)$$

where

$$\Theta_{l_1 l_2 L M}^{l'_1 l'_2 L' M'} = \langle \mathcal{Y}_{l_1, l_2}^{LM}(\Omega_1, \Omega_2) | \cos \theta_1 | \mathcal{Y}_{l'_1, l'_2}^{L' M'}(\Omega_1, \Omega_2) \rangle. \quad (4.4.3)$$

Here ω_i and λ_j are the corresponding Gauss-Legendre weights to the hyperradial and hyperangle spatial integrals, respectively. For states in dc field along the z -direction, the total magnetic quantum number M is a conserved quantity, while the parity along the z -axis (π_z) is not conserved. We will focus our attention on the $M = 0$ manifolds. Since parity is not conserved, angular momentum states $^1S^e$, $^1P^o$, $^1D^e$, and $^1F^o$ are coupled together in Eq. 4.4.2 by the external electric field. This four-symmetry ($L_{max} = 3$) calculation is sufficient to compute such doubly excited states in electric field. We investigate $^1S^e(2, n, a, b)$, $^1P^o(2, n, a, b, c)$, and $^1D^e(2, n, a, b, c)$ resonance states where $n = 10 - 20$ in the electric field. In the present electric field calculations we have used a mesh of $N_R \times N_\alpha = 400 \times 400$, and twenty adiabatic channels ($\mu = 20$) to compute the field-free wavefunctions Ψ_k^L where $L = 0, 1, 2, 3$. Our calculated widths are converged when the angle θ is varied from 0.1 to 0.3 rad.

In Tables 4.5-4.10 we report electric field effects on resonant energies and widths for doubly excited Rydberg states of He field strengths F are varied from 1 to 84.4 kV/cm. Since the autoionization rates in the states of interest are small to begin with $^1P^o(2, 10a)$ ($\Gamma = 8.104 \times 10^{-6}$ a.u.) even small electric field strengths has effects on these doubly excited states. As the external field increases all resonance energies and widths of the doubly excited states are changed due to Stark mixing.

In the present calculation, Tables 4.5-4.10 has a common trend of the resonant energies being shifted downward as the electric field is increased and widths are decreasing for most of the states. This is mainly due to the Stark effect and energy separation between the states becoming smaller.

In the absence of an electric field only the $^1P^o$ state can be achieved from the $^1S^e$ ground-state by single-photon absorption. When the external field is turned on the nearby $^1D^e$ resonance is induced by the $^1P^o$ state due to Stark mixing of the two resonances. Therefore, the autoionization rates for the $^1P^o$ states are mostly decreasing due to mixing with other singlet-spin states.

4.5 Conclusion

In summary, we have presented a *ab initio* complex-scaling generalized pseudospectral method in hyperspherical coordinates for the accurate treatment of doubly-excited

Rydberg resonance states and dc-field ionization rates of the two-electron atomic systems. Our CSGPS approach in hyperspherical coordinates is shown to be capable of providing accurate resonance energies for $^1S^e$, $^1P^o$, $^1D^e$, and $^1F^o$ Rydberg doubly excited states with the use of only a modest number of grid points. The affects of dc-field ionization rates on the $^1S^e$ ($2, n, a, b$), $^1P^o$ ($2, n, a, b, c$), and $^1D^e$ ($2, n, a, b, c$) states where $n = 10 - 20$ have been identified. The theory is in good agreement with the published theoretical results where He doubly excited states range from $n = 10 - 15$, and predict the outcome in cases where results are not yet available $n = 15 - 20$. This is the first theoretical works to our knowledge for such Rydberg doubly excited states. We hope that our present data and findings stimulate some new experimental activities in the near future.

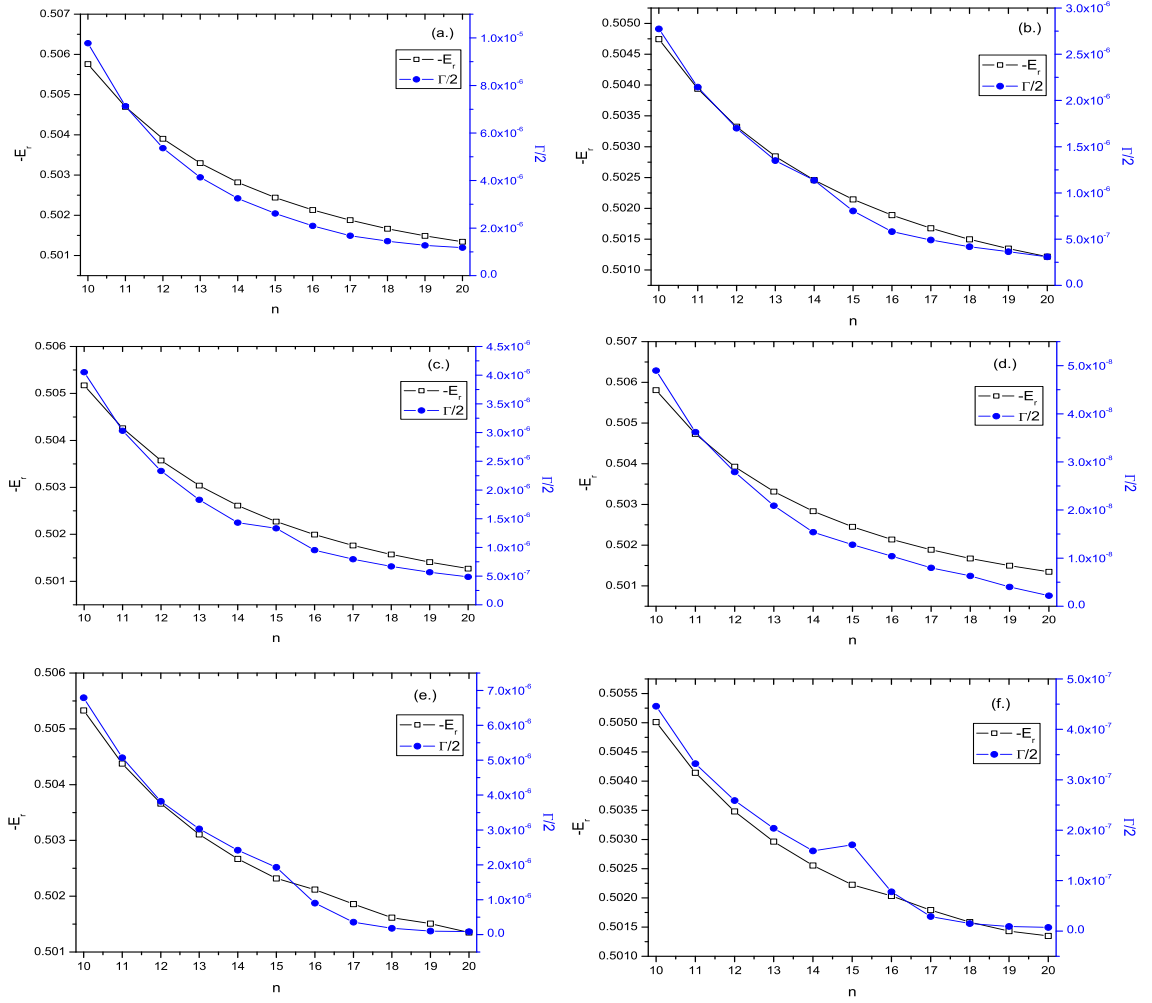


Figure 4.2: Field-free energies and widths of doubly excited Rydberg states as a function of the principle quantum number n , in the energy region below the $N = 2$ threshold for different symmetries: (a) $1S^e(2, na)$, (b) $1S^e(2, nb)$, (c) $1P^o(2, na)$, (d) $1P^o(2, nb)$, (e) $1D^e(2, na)$, and (f) $1D^e(2, nb)$.

Table 4.1: Energies and widths for doubly excited Rydberg states $^1S^e(2, n, (a, b))$ below the $N = 2$ threshold (in a.u.). Numbers in square brackets indicate powers of ten.

	State	$-E_r$	$\Gamma/2$		State	$-E_r$	$\Gamma/2$
Present	10a	0.505759011	9.777[−6]		10b	0.504746220	2.775[−6]
[43]		0.505759052	9.777[−6]			0.504746230	2.776[−6]
[3]		0.505759104	9.790[−6]			0.504746388	2.766[−6]
Present	11a	0.504697225	7.131[−6]		11b	0.503940604	2.145[−6]
[43]		0.504697299	7.131[−6]			0.503940615	2.146[−6]
[35]		0.504697187	7.131[−6]				
Present	12a	0.503904116	5.362[−6]		12b	0.503324068	1.700[−6]
[43]		0.503904132	5.362[−6]			0.503324031	1.690[−6]
[35]		0.503904047	5.360[−6]				
Present	13a	0.503296014	4.134[−6]		13b	0.502841616	1.350[−6]
[43]		0.503296078	4.134[−6]			0.502841626	1.350[−6]
[35]		0.503296011	4.131[−6]				
Present	14a	0.502819664	3.251[−6]		14b	0.502457209	1.137[−6]
[43]		0.502819726	3.253[−6]			0.502457222	1.136[−6]
[35]		0.502819669	3.239[−6]				
Present	15a	0.502439597	2.613[−6]		15b	0.502145509	8.058[−7]
[43]		0.502439676	2.617[−6]			0.502145517	8.06[−7]
[35]		0.502439599	2.689[−6]				
Present	16a	0.502131622	2.090[−6]		16b	0.501889058	5.817[−7]
Present	17a	0.501878528	1.681[−6]		17b	0.501676589	4.910[−7]
Present	18a	0.501666988	1.452[−6]		18b	0.501498052	4.181[−7]
Present	19a	0.501489971	1.274[−6]		19b	0.501346589	3.647[−7]
Present	20a	0.501341721	1.179[−6]		20b	0.501216515	3.082[−7]

Table 4.2: Energies and widths for doubly excited Rydberg states $^1P^o$ ($2, n, (a, b, c)$) below the $N = 2$ threshold (in a.u.). Numbers in square brackets indicate powers of ten.

	State	$-E_r$	$\Gamma/2$	State	$-E_r$	$\Gamma/2$	State	$-E_r$	$\Gamma/2$
Present [43] [19]	10a	0.505174452	4.052[-6]	10b	0.505806734	4.90[-8]	10c	0.504758332	8.1[-11]
		0.505174494	4.054[-6]		0.505806870	4.9[-8]		0.504758391	
		0.505175	4[-6]		0.50580696	1.0[-7]		0.5047590	
Present [43]	11a	0.504259181	3.031[-6]	11b	0.504732042	3.62[-8]	11c	0.503950110	6.0[-11]
		0.504262710	3.038[-6]		0.504732057	3.6[-8]		0.503950219	
Present [43]	12a	0.503572206	2.332[-6]	12b	0.503930196	2.79[-8]	12c	0.503331700	3.3[-11]
		0.503572348	2.335[-6]		0.503930208	2.8[-8]		0.503331706	
Present [43]	13a	0.503037023	1.829[-6]	13b	0.503316098	2.09[-8]	13c	0.502847463	1.5[-11]
		0.503037093	1.834[-6]		0.503316151	2.1[-8]		0.502847834	
Present [43]	14a	0.502613680	1.432[-6]	14b	0.502835501	1.54[-8]	14c	0.502462316	0.7[-11]
		0.502613741	1.434[-6]		0.502835510	1.5[-8]		0.502462325	
Present [43]	15a	0.502273019	1.332[-6]	15b	0.502452286	1.28[-8]	15c	0.502149624	0.1[-11]
		0.502273028	1.335[-6]		0.502452349	3.9[-8]		0.502149666	
Present	16a	0.501993794	9.535[-7]	16b	0.502140336	1.04[-8]	16c	0.501892145	
Present	17a	0.501763954	7.939[-7]	17b	0.501885535	8.0[-9]	17c	0.501679199	
Present	18a	0.501571686	6.680[-7]	18b	0.501673666	6.3[-9]	18c	0.501500276	
Present	19a	0.501409224	5.674[-7]	19b	0.501495600	4.0[-9]	19c	0.501348498	
Present	20a	0.501270711	4.859[-7]	20b	0.5013445104	2.2[-9]	20c	0.501218639	

Table 4.3: Energies and widths for doubly excited Rydberg states $^1D^e(2, n, (a, b, c))$ below the $N = 2$ threshold (in a.u.). Numbers in square brackets indicate powers of ten.

	State	$-E_r$	$\Gamma/2$	State	$-E_r$	$\Gamma/2$	State	$-E_r$	$\Gamma/2$
Present [43]	10a	0.505328768	6.793[-6]	10b	0.505012277	4.46[-7]	10c	0.504874911	1.8[-9]
		0.505328784	6.799[-6]		0.505012580	4.47[-7]		0.504874929	1[-9]
Present [43]	11a	0.504378289	5.069[-6]	11b	0.504141604	3.32[-7]	11c	0.504038182	1.1[-9]
		0.504378303	5.071[-6]		0.504141617	3.38[-7]		0.504038200	1[-9]
Present [43]	12a	0.503661137	3.821[-6]	12b	0.503479422	2.59[-7]	12c	0.503399708	8.3[-10]
		0.503661148	3.882[-6]		0.503479414	2.62[-7]		0.503399748	8[-10]
Present [43]	13a	0.503106758	3.031[-6]	13b	0.502964210	2.04[-7]	13c	0.502901529	7.2[-10]
		0.503106766	3.037[-6]		0.502964214	2.07[-7]		0.502901543	7[-10]
Present [43]	14a	0.502669301	2.419[-6]	14b	0.502555489	1.59[-7]	14c	0.502505310	5.4[-10]
		0.502669381	2.421[-6]		0.502555511	1.62[-7]		0.502505327	
Present [43]	15a	0.502318297	1.931[-6]	15b	0.502225905	1.71[-7]	15c	0.502185026	3.9[-10]
		0.502318305	1.939[-6]		0.502225953	1.76[-7]		0.502185075	
Present	16a	0.502119020	9.04[-7]	16b	0.502032470	7.8[-8]	16c	0.501952454	9.2[-11]
Present	17a	0.501858693	3.54[-7]	17b	0.501792102	2.9[-8]	17c	0.501720766	3.7[-11]
Present	18a	0.501614863	1.80[-7]	18b	0.501586479	1.5[-8]	18c	0.501530058	
Present	19a	0.501507873	1.01[-7]	19b	0.501431527	9.2[-9]	19c	0.501401640	
Present	20a	0.501348770	8.1[-8]	20b	0.501349341	7.2[-9]	20c	0.501218639	

Table 4.4: Energies and widths for doubly excited Rydberg states $^1F^o(2, n, (a, b, c))$ below the $N = 2$ threshold (in a.u.). Numbers in square brackets indicate powers of ten.

	State	$-E_r$	$\Gamma/2$	State	$-E_r$	$\Gamma/2$	State	$-E_r$
Present	10a	0.505058334	2.89[-7]	10b	0.505016412	1.8[-10]	10c	0.504924432
[43]		0.505058342	2.88[-7]		0.505016428	2[-10]		0.504924466
Present	11a	0.504175912	2.20[-7]	11b	0.504144617	1.2[-10]	11c	0.504076210
[43]		0.504175949	2.18[-7]		0.504144611	1[-10]		0.504076225
Present	12a	0.503505796	1.68[-7]	12b	0.503481706	1.0[-10]	12c	0.503429022
[43]		0.503505827	1.69[-7]		0.503481779	1[-10]		0.503429075
Present	13a	0.502984948	1.35[-7]	13b	0.502966093	7.8[-11]	13c	0.502924588
[43]		0.502984969	1.33[-7]		0.502966109	8[-11]		0.502924637
Present	14a	0.502572129	1.09[-7]	14b	0.502557030	5.6[-11]	14c	0.502523827
[43]		0.502572121	1.07[-7]		0.502557054	6[-11]		0.502523838
Present	15a	0.502239306	7.4[-8]	15b	0.502227098	4.3[-11]	15c	0.502200108
[43]		0.502239372	7.5[-8]		0.502227191			0.502200122
Present	16a	0.501840336	5.0[-8]	16b	0.501793794	1.2[-11]	16c	0.501692145
Present	17a	0.501685535	2.0[-8]	17b	0.501563954	0.2[-11]	17c	0.501579199
Present	18a	0.501473666	9.3[-9]	18b	0.501471686		18c	0.501300276
Present	19a	0.501395600	1.2[-9]	19b	0.501209224		19c	0.501248498
Present	20a	0.501244510	6.2[-10]	20b	0.501070711		20c	0.501118639

Table 4.5: Field-perturbed resonant energies E_r and widths (in a.u.) for the $^1S^e$ $n = 10 - 20$ doubly excited Rydberg states below the N=2 threshold. Numbers in square brackets indicate powers of ten.

$F(\text{kV/cm})$	State	$-E_r$	$\Gamma/2$	State	$-E_r$	$\Gamma/2$
1	10a	0.505761021	8.438[-6]	10b	0.504751047	2.022[-6]
2		0.505778231	7.992[-6]		0.504755921	1.521[-6]
3		0.505789074	7.167[-6]		0.504770093	9.889[-7]
4		0.505791002	6.415[-6]		0.504787332	7.375[-7]
5		0.505800284	5.838[-6]		0.504791481	5.563[-7]
6		0.505819926	3.851[-6]		0.504816632	3.662[-7]
1	11a	0.504712391	6.002[-6]	11b	0.503950484	1.221[-6]
2		0.504737532	4.394[-6]		0.503965501	9.111[-7]
3		0.504750094	3.873[-6]		0.503972941	7.031[-7]
4		0.504767427	2.529[-6]		0.503990038	6.109[-7]
5		0.504783724	1.988[-6]		0.504039185	5.118[-7]
6		0.504793821	9.774[-7]		0.504042572	3.107[-7]
1	12a	0.503918813	4.204[-6]	12b	0.503330018	9.889[-7]
2		0.503930052	3.270[-6]		0.503337228	7.001[-7]
3		0.503944385	2.884[-6]		0.503352291	5.032[-7]
4		0.503960296	1.563[-6]		0.503365106	4.664[-7]
5		0.503971031	9.774[-7]		0.503384819	3.914[-7]
6		0.503983888	7.401[-7]		0.503399210	2.011[-7]
1	13a	0.503306014	3.997[-6]	13b	0.502855493	9.001[-7]
2		0.503310039	3.559[-6]		0.502866674	6.424[-7]
3		0.503334429	2.502[-6]		0.502880079	5.000[-7]
4		0.503345301	1.473[-6]		0.502894281	3.105[-7]
5		0.503357358	9.412[-7]		0.502908813	2.871[-7]
6		0.503370074	6.317[-7]		0.502920025	1.167[-7]
1	14a	0.502820095	3.008[-6]	14b	0.502468009	8.999[-7]
2		0.502835229	2.510[-6]		0.502478223	6.199[-7]
3		0.502848830	1.996[-6]		0.502482012	4.130[-7]
4		0.502860028	9.891[-7]		0.502498002	2.910[-7]
5		0.502871994	7.428[-7]		0.502500365	1.224[-7]
6		0.502888912	5.221[-7]		0.502520772	9.887[-8]
1	15a	0.502440492	1.993[-6]	15b	0.502159921	6.050[-7]
2		0.502454783	9.593[-7]		0.502165592	4.992[-7]
3		0.502460081	7.841[-7]		0.502180009	2.889[-7]
4		0.502478009	5.885[-7]		0.502189782	1.023[-7]
5		0.502490000	3.002[-7]		0.502195945	7.80[-8]
6		0.502500243	2.555[-7]		0.502216583	5.52[-8]
1	16a	0.502148819	1.991[-6]	16b	0.501898099	4.557[-7]
2		0.502152014	1.003[-6]		0.501909901	3.339[-7]
3		0.502161998	8.992[-7]		0.501920018	2.732[-7]
4		0.502181831	6.443[-7]		0.501931142	1.150[-7]
5		0.502198824	4.039[-7]		0.501940021	7.10[-8]
6		0.502209998	2.483[-7]		0.501956679	4.00[-8]
1	17a	0.501888291	1.002[-6]	17b	0.501684421	3.784[-7]
2		0.501893353	8.992[-7]		0.501690041	2.885[-7]
3		0.501904968	6.034[-7]		0.501709921	1.685[-7]
4		0.501915399	5.392[-7]		0.501719022	8.14[-8]
5		0.501926622	3.118[-7]		0.501729777	6.05[-8]
6		0.501936771	1.922[-7]		0.501733249	4.23[-8]
1	18a	0.501670081	9.662[-7]	18b	0.501509991	3.992[-7]
2		0.501688933	7.008[-7]		0.501511892	2.797[-7]
3		0.501690029	6.662[-7]		0.501528860	1.528[-7]
4		0.501709921	4.849[-7]		0.501530052	1.001[-7]
5		0.501713386	3.244[-7]		0.501544484	8.90[-8]
6		0.501720053	1.860[-7]		0.501560035	6.04[-8]
1	19a	0.501495865	1.004[-6]	19b	0.501360037	1.485[-7]
2		0.501507693	9.339[-7]		0.501378003	9.92[-8]
3		0.501510034	7.811[-7]		0.501388635	7.23[-8]
4		0.501527482	5.538[-7]		0.501399001	5.60[-8]
5		0.501537849	3.997[-7]		0.501407458	3.46[-8]
6		0.501549933	2.047[-7]		0.501416550	2.21[-8]
1	20a	0.501357382	9.991[-7]	20b	0.501230062	2.887[-7]
2		0.501360019	7.445[-7]		0.501243943	1.442[-7]
3		0.501387422	5.003[-7]		0.501260032	8.33[-8]
4		0.501399018	3.227[-7]		0.501271965	6.73[-8]
5		0.501443911	1.129[-7]		0.501281628	4.19[-8]
6		0.501458890	7.72[-8]		0.501299743	2.66[-8]

Table 4.6: Field-perturbed resonant energies E_r and widths (in a.u.) for the $^1P^o$ $n = 10 - 20$ doubly excited Rydberg states below the N=2 threshold. Numbers in square brackets indicate powers of ten.

$F(\text{kV/cm})$	$-E_r$	$\Gamma/2$	$-E_r$	$\Gamma/2$	$-E_r$	$\Gamma/2$
	10a		10b		10c	
1	0.505180929	3.989[-6]	0.505810092	7.20[-8]	0.504748831	2.12[-8]
2	0.505193123	3.005[-6]	0.505825711	7.80[-8]	0.504730029	3.56[-8]
3	0.505206360	2.557[-6]	0.505835579	8.11[-8]	0.504718814	3.89[-8]
4	0.505218842	1.882[-6]	0.505844214	8.55[-8]	0.504698332	4.67[-8]
5	0.505224428	1.002[-6]	0.505858819	9.27[-8]	0.504631388	5.38[-8]
6	0.505236619	9.40[-7]	0.505862374	9.84[-8]	0.504607431	6.22[-8]
	11a		11b		11c	
1	0.504269921	2.144[-6]	0.504740013	4.12[-8]	0.503942274	2.01[-8]
2	0.504277374	1.882[-6]	0.504757436	4.82[-8]	0.503870024	3.44[-8]
3	0.504280028	1.002[-6]	0.504767991	5.12[-8]	0.503781838	3.79[-8]
4	0.504298813	9.32[-7]	0.504780023	6.49[-8]	0.503719284	4.53[-8]
5	0.504307633	7.03[-7]	0.504791120	7.83[-8]	0.5037004532	5.20[-8]
6	0.504317438	5.20[-7]	0.504802277	8.21[-8]	0.503690481	6.15[-8]
	12a		12b		12c	
1	0.503583386	1.442[-6]	0.503949921	3.23[-8]	0.503324811	1.72[-8]
2	0.503593472	1.001[-6]	0.503950043	4.10[-8]	0.503310024	2.87[-8]
3	0.503600081	8.05[-7]	0.503969191	4.89[-8]	0.503296609	3.12[-8]
4	0.503619921	6.11[-7]	0.503976362	5.23[-8]	0.503268819	3.76[-8]
5	0.503626462	4.92[-7]	0.503984622	6.01[-8]	0.503248211	4.64[-8]
6	0.503630028	2.18[-7]	0.503997311	7.27[-8]	0.503210992	5.32[-8]
	13a		13b		13c	
1	0.503041992	1.001[-6]	0.503322991	3.48[-8]	0.502758811	9.7[-9]
2	0.503059393	8.07[-7]	0.503331382	3.87[-8]	0.502713382	1.26[-8]
3	0.503060011	6.10[-7]	0.503340021	4.11[-8]	0.502690021	2.45[-8]
4	0.503071282	4.33[-7]	0.503352211	4.52[-8]	0.502660119	3.19[-8]
5	0.503082221	3.00[-7]	0.503360219	5.26[-8]	0.502611091	3.99[-8]
6	0.503090033	1.22[-7]	0.503370032	6.17[-8]	0.502560977	4.64[-8]
	14a		14b		14c	
1	0.502620041	9.34[-7]	0.502840282	2.33[-8]	0.502410025	8.5[-9]
2	0.502638832	7.04[-7]	0.502850011	3.99[-8]	0.502382281	9.4[-9]
3	0.502648810	5.10[-7]	0.502860028	4.39[-8]	0.502369008	9.9[-9]
4	0.502650912	3.88[-7]	0.502877821	4.87[-8]	0.502320023	1.56[-8]
5	0.502669083	1.11[-7]	0.502880086	5.26[-8]	0.502291738	2.15[-8]
6	0.502675002	8.03[-8]	0.502894419	6.12[-8]	0.502240033	3.11[-8]
	15a		15b		15c	
1	0.502282249	7.03[-7]	0.502460089	4.10[-8]	0.502001999	8.1[-9]
2	0.502290023	5.51[-7]	0.502473114	4.88[-8]	0.501967719	8.6[-9]
3	0.502300081	3.44[-7]	0.502489292	5.12[-8]	0.501910097	9.3[-9]
4	0.502320289	1.39[-7]	0.502490955	5.97[-8]	0.501889291	9.9[-9]
5	0.502330071	9.22[-8]	0.502503001	6.25[-8]	0.501848884	1.54[-8]
6	0.502352226	7.40[-8]	0.502517355	7.32[-8]	0.501788161	1.97[-8]
	16a		16b		16c	
1	0.502010031	7.28[-7]	0.502150112	2.31[-8]	0.501810063	7.7[-9]
2	0.502030000	5.11[-7]	0.502168991	3.49[-8]	0.501782845	8.0[-9]
3	0.502042248	3.04[-7]	0.502177729	3.87[-8]	0.501703959	8.4[-9]
4	0.502057437	1.05[-7]	0.502188284	4.52[-8]	0.501679911	8.9[-9]
5	0.502062991	8.23[-8]	0.502190477	5.18[-8]	0.501629933	9.3[-9]
6	0.502074433	5.66[-8]	0.502218831	6.64[-8]	0.501566726	9.9[-9]
	17a		17b		17c	
1	0.501770913	5.23[-7]	0.501892919	9.2[-9]	0.501602006	7.1[-9]
2	0.501781091	3.12[-7]	0.501910027	1.33[-8]	0.501574091	7.5[-9]
3	0.501790081	1.40[-7]	0.501929774	1.55[-8]	0.501519911	8.2[-9]
4	0.501810058	8.04[-8]	0.501930944	2.13[-8]	0.501482099	8.7[-9]
5	0.501823911	5.11[-8]	0.501941153	2.92[-8]	0.501424002	9.1[-9]
6	0.501833091	2.40[-8]	0.501950434	3.48[-8]	0.501394933	9.8[-9]
	18a		18b		18c	
1	0.501582091	4.68[-7]	0.501688099	7.2[-9]	0.501460919	6.6[-9]
2	0.501593993	2.09[-7]	0.501698553	7.9[-9]	0.501422999	6.9[-9]
3	0.501610071	8.00[-8]	0.501709004	8.22[-8]	0.501384444	7.3[-9]
4	0.501622977	5.44[-8]	0.501718821	8.98[-8]	0.501325002	7.8[-9]
5	0.501639033	2.11[-8]	0.501724022	9.31[-8]	0.501288137	8.1[-9]
6	0.501644747	9.2[-9]	0.501733441	9.98[-8]	0.501242007	8.7[-9]

Table 4.7: (continued) Field-perturbed resonant energies E_r and widths (in a.u.) for the $^1P^o$ $n = 10 - 20$ doubly excited Rydberg states below the $N=2$ threshold. Numbers in square brackets indicate powers of ten.

$F(\text{kV/cm})$	$-E_r$	$\Gamma/2$	$-E_r$	$\Gamma/2$	$-E_r$	$\Gamma/2$
	19a		19b		19c	
1	0.501413088	3.42[-7]	0.501508881	5.2[-9]	0.501302009	6.3[-9]
2	0.501421332	1.59[-7]	0.501517006	6.0[-9]	0.501266883	6.7[-9]
3	0.501430013	8.94[-8]	0.501522835	6.9[-9]	0.501224995	7.1[-9]
4	0.501450222	4.99[-8]	0.501540065	7.46[-8]	0.501188661	7.7[-9]
5	0.501467121	1.22[-8]	0.501551143	7.94[-8]	0.501150918	8.0[-9]
6	0.501478003	8.4[-9]	0.501566045	8.38[-8]	0.501110454	8.6[-9]
	20a		20b		20c	
1	0.501288991	2.331[-7]	0.501355883	3.1[-9]	0.501182000	6.0[-9]
2	0.501297555	9.34[-8]	0.501367000	3.8[-9]	0.501158099	6.2[-9]
3	0.501316088	6.22[-8]	0.501374442	4.4[-9]	0.501124911	6.7[-9]
4	0.501322809	4.77[-8]	0.501382045	5.1[-9]	0.501086017	7.3[-9]
5	0.501339887	1.03[-8]	0.501395558	5.9[-9]	0.501049444	7.8[-9]
6	0.501344656	7.9[-9]	0.501418831	6.6[-9]	0.501013918	8.1[-9]

Table 4.8: Field-perturbed resonant energies E_r and widths (in a.u.) for the $^1D^e$ $n = 10 - 20$ doubly excited Rydberg states below the N=2 threshold. Numbers in square brackets indicate powers of ten.

$F(\text{kV/cm})$	$-E_r$	$\Gamma/2$	$-E_r$	$\Gamma/2$	$-E_r$	$\Gamma/2$
	10a		10b		10c	
1	0.505330499	4.445[-6]	0.505029981	2.089[-7]	0.504808000	5.8[-9]
2	0.505347991	3.359[-6]	0.505034011	9.12[-8]	0.504697932	6.7[-9]
3	0.505360005	1.995[-6]	0.505047772	7.01[-8]	0.504580931	7.4[-9]
4	0.505372224	8.474[-7]	0.505052998	6.22[-8]	0.504471119	7.9[-9]
5	0.505388184	6.555[-7]	0.505062244	4.05[-8]	0.504336010	8.3[-9]
6	0.505399910	4.228[-7]	0.505077911	2.10[-8]	0.504244057	8.9[-9]
	11a		11b		11c	
1	0.504387009	3.865[-6]	0.504155091	1.08[-7]	0.503942998	4.7[-9]
2	0.504398755	1.711[-6]	0.504167999	7.99[-8]	0.503889919	5.4[-9]
3	0.504416464	8.03[-7]	0.504173088	5.39[-8]	0.503816877	5.9[-9]
4	0.504420021	6.65[-7]	0.504187211	3.44[-8]	0.503778004	6.3[-9]
5	0.504439383	4.42[-7]	0.504192005	1.92[-8]	0.503724662	7.1[-9]
6	0.504444821	2.81[-7]	0.504209111	7.3[-9]	0.503647938	7.8[-9]
	12a		12b		12c	
1	0.503672259	1.023[-6]	0.503488019	9.59[-8]	0.503299101	4.2[-9]
2	0.503680521	8.07[-7]	0.503497714	7.33[-8]	0.503210111	4.9[-9]
3	0.503697811	6.44[-7]	0.503509994	5.03[-8]	0.503179922	5.5[-9]
4	0.503700089	3.08[-7]	0.503518348	3.08[-8]	0.503122818	5.9[-9]
5	0.503719989	1.22[-7]	0.503520081	1.00[-8]	0.503060088	6.4[-9]
6	0.503720098	8.88[-8]	0.503530991	6.2[-9]	0.503014099	7.0[-9]
	13a		13b		13c	
1	0.503118881	9.22[-7]	0.502970891	8.24[-8]	0.502870091	4.0[-9]
2	0.503128839	7.01[-7]	0.502987774	6.33[-8]	0.502808887	4.7[-9]
3	0.503137731	5.88[-7]	0.502993008	4.73[-8]	0.502760421	5.3[-9]
4	0.503140096	2.99[-7]	0.503010621	1.99[-8]	0.502703772	5.7[-9]
5	0.503156993	9.45[-8]	0.503020189	8.1[-9]	0.502669389	6.2[-9]
6	0.503169918	7.02[-8]	0.503038895	5.7[-9]	0.502580088	6.9[-9]
	14a		14b		14c	
1	0.502674991	9.00[-7]	0.502567471	7.99[-8]	0.502417091	3.7[-9]
2	0.502682255	6.88[-7]	0.502570093	5.04[-8]	0.502328009	4.2[-9]
3	0.502690089	4.05[-7]	0.502582277	3.09[-8]	0.502294988	4.8[-9]
4	0.502702225	1.99[-7]	0.502599008	1.00[-8]	0.502216071	5.3[-9]
5	0.502715585	8.22[-8]	0.502601029	7.2[-9]	0.502158899	5.9[-9]
6	0.502726911	6.44[-8]	0.502619081	4.3[-9]	0.502063310	6.1[-9]
	15a		15b		15c	
1	0.502328009	8.33[-7]	0.502239777	7.01[-8]	0.502106114	3.2[-9]
2	0.502331939	6.08[-7]	0.502245989	4.24[-8]	0.502058188	3.9[-9]
3	0.502342241	3.12[-7]	0.502254008	2.05[-8]	0.501983917	4.3[-9]
4	0.502357838	1.10[-7]	0.502268887	9.10[-9]	0.501925949	4.8[-9]
5	0.502370112	7.01[-8]	0.502272941	6.88[-9]	0.501887977	5.6[-9]
6	0.502382095	5.99[-8]	0.502288012	3.43[-9]	0.501845009	6.0[-9]
	16a		16b		16c	
1	0.502129443	7.02[-7]	0.502044557	5.69[-8]	0.501902255	2.8[-9]
2	0.502138029	5.10[-7]	0.502057047	3.48[-8]	0.501876915	3.1[-9]
3	0.502146465	2.04[-7]	0.502066120	1.61[-8]	0.501812156	3.7[-9]
4	0.502155172	9.55[-8]	0.502078795	8.11[-9]	0.501766322	4.2[-9]
5	0.502162881	6.95[-8]	0.502082227	5.97[-9]	0.501723364	4.8[-9]
6	0.502179194	4.43[-8]	0.502096116	2.65[-9]	0.501695506	5.3[-9]
	17a		17b		17c	
1	0.501866142	1.02[-7]	0.501806175	1.22[-8]	0.501653143	2.3[-9]
2	0.501873111	8.94[-8]	0.501817223	9.52[-9]	0.501602159	2.7[-9]
3	0.501885521	7.56[-8]	0.501823609	7.57[-9]	0.501558499	3.4[-9]
4	0.501897490	5.82[-8]	0.501837747	5.22[-9]	0.501516471	3.9[-9]
5	0.501908355	3.06[-8]	0.501848593	4.36[-9]	0.501471104	4.4[-9]
6	0.501919978	1.11[-8]	0.501861678	2.47[-9]	0.501415494	4.9[-9]
	18a		18b		18c	
1	0.501624352	8.99[-8]	0.501595521	9.33[-9]	0.501473833	1.8[-9]
2	0.501636115	6.50[-8]	0.501610017	8.01[-9]	0.501427586	2.2[-9]
3	0.501644103	3.19[-8]	0.501623846	6.71[-9]	0.501389292	2.5[-9]
4	0.501653053	1.17[-8]	0.501635225	4.12[-9]	0.501318503	3.1[-9]
5	0.501667027	8.44[-9]	0.501646493	3.25[-9]	0.501283500	3.7[-9]
6	0.501674821	7.38[-9]	0.501653919	1.03[-9]	0.501195105	4.3[-9]

Table 4.9: (continued) Field-perturbed resonant energies E_r and widths (in a.u.) for the $^1D^e$ $n = 10 - 20$ doubly excited Rydberg states below the $N=2$ threshold. Numbers in square brackets indicate powers of ten.

$F(\text{kV}/\text{cm})$	$-E_r$	$\Gamma/2$	$-E_r$	$\Gamma/2$	$-E_r$	$\Gamma/2$
	19a		19b		19c	
1	0.501518739	7.92[-8]	0.501445114	8.23[-9]	0.501388225	1.3[-9]
2	0.501527331	5.66[-8]	0.501457609	7.02[-9]	0.501329606	1.6[-9]
3	0.501539469	2.95[-8]	0.501468313	5.77[-9]	0.501260917	2.1[-9]
4	0.501551067	9.80[-9]	0.501477737	3.14[-9]	0.501218009	2.4[-9]
5	0.501567737	7.41[-9]	0.501483917	1.50[-9]	0.501174989	2.9[-9]
6	0.501576098	5.02[-9]	0.501496849	8.1[-10]	0.501125152	3.3[-9]
	20a		20b		20c	
1	0.501357129	6.15[-8]	0.501350661	6.11[-9]	0.501173847	1.0[-9]
2	0.501368704	4.63[-8]	0.501362473	4.54[-9]	0.501157163	1.5[-9]
3	0.501372515	2.02[-8]	0.501371930	2.00[-9]	0.501114938	2.0[-9]
4	0.501384277	9.22[-9]	0.501380184	8.9[-10]	0.501099593	2.3[-9]
5	0.501392287	6.06[-9]	0.501391653	7.1[-10]	0.5010567919	2.7[-9]
6	0.501406680	4.11[-9]	0.501404262	5.6[-10]	0.501005811	3.1[-9]

Table 4.10: Given are resonant energies E_r and widths (in a.u.) for the $n = 10 - 20$ doubly excited Rydberg states below the $N=2$ threshold in a dc field of 84.4 kV/cm . Numbers in square brackets indicate powers of ten. $n(a, b)^*$ indicates the comparison with Mihelić and Žitnik [44].

State	$-E_r$	$\Gamma/2$	State	$-E_r$	$\Gamma/2$	State	$-E_r$	$\Gamma/2$
$6a \ ^1S^e$	0.517409310	3.58[-5]	$12b \ ^1P^o$	0.504100999	2.79[-6]	$16c \ ^1P^o$	0.501305276	8.27[-7]
$6a^* \ ^1S^e$	0.517409314	3.58[-5]	$12b \ ^1D^e$	0.503622509	1.31[-7]	$16c \ ^1D^e$	0.500943288	8.02[-8]
$6a \ ^1P^o$	0.514925658	2.84[-5]	$12c \ ^1P^o$	0.502921101	9.13[-6]	$17a \ ^1S^e$	0.502088342	5.99[-8]
$6a^* \ ^1P^o$	0.514925667	2.84[-5]	$12c \ ^1D^e$	0.502700813	9.34[-8]	$17a \ ^1P^o$	0.501939811	8.91[-9]
$6a \ ^1D^e$	0.515412563	6.47[-5]	$13a \ ^1S^e$	0.503522901	2.39[-7]	$17a \ ^1D^e$	0.502035355	8.77[-9]
$6b \ ^1S^e$	0.512779312	7.23[-6]	$13a \ ^1P^o$	0.503229219	8.11[-8]	$17b \ ^1S^e$	0.501800911	9.55[-9]
$6b \ ^1P^o$	0.518215577	1.16[-5]	$13a \ ^1D^e$	0.503309887	3.01[-8]	$17b \ ^1P^o$	0.502059991	8.01[-7]
$6b^* \ ^1P^o$	0.518215592	1.16[-5]	$13b \ ^1S^e$	0.503037528	8.00[-8]	$17b \ ^1D^e$	0.502034894	1.93[-8]
$6b \ ^1D^e$	0.515551648	5.71[-5]	$13b \ ^1P^o$	0.503589292	2.09[-6]	$17c \ ^1P^o$	0.501250981	8.12[-7]
$6b^* \ ^1D^e$	0.515551667	5.71[-5]	$13b \ ^1D^e$	0.503100877	1.01[-7]	$17c \ ^1D^e$	0.500821971	7.96[-8]
$6c \ ^1P^o$	0.512274088	1.74[-5]	$13c \ ^1P^o$	0.502391982	8.99[-7]	$18a \ ^1S^e$	0.501855299	5.50[-8]
$6c^* \ ^1P^o$	0.512274095	1.74[-5]	$13c \ ^1D^e$	0.501394831	8.76[-8]	$18a \ ^1P^o$	0.501747771	6.54[-9]
$6c \ ^1D^e$	0.512957138	8.92[-7]	$14a \ ^1S^e$	0.503000852	1.00[-7]	$18a \ ^1D^e$	0.501832134	4.03[-9]
$6c^* \ ^1D^e$	0.512957142	8.92[-7]	$14a \ ^1P^o$	0.502820915	4.55[-8]	$18b \ ^1S^e$	0.501623239	8.91[-9]
$10a \ ^1S^e$	0.505921049	8.33[-7]	$14a \ ^1D^e$	0.502840088	2.35[-8]	$18b \ ^1P^o$	0.501848888	6.33[-7]
$10a \ ^1P^o$	0.505322941	6.22[-7]	$14b \ ^1S^e$	0.502634442	6.03[-8]	$18b \ ^1D^e$	0.501763682	9.55[-9]
$10a \ ^1D^e$	0.505530061	8.45[-8]	$14b \ ^1P^o$	0.503009771	1.54[-6]	$18c \ ^1P^o$	0.501148181	7.97[-8]
$10b \ ^1S^e$	0.504957384	7.09[-8]	$14b \ ^1D^e$	0.502774469	9.80[-8]	$18c \ ^1D^e$	0.500639271	7.61[-8]
$10b \ ^1P^o$	0.506038439	4.90[-6]	$14c \ ^1P^o$	0.501988231	8.65[-7]	$19a \ ^1S^e$	0.501699956	5.33[-8]
$10b \ ^1D^e$	0.505260917	3.22[-7]	$14c \ ^1D^e$	0.501143329	8.31[-8]	$19a \ ^1P^o$	0.501626566	5.32[-9]
$10c \ ^1P^o$	0.504299313	9.44[-6]	$15a \ ^1S^e$	0.502688001	8.79[-8]	$19a \ ^1D^e$	0.501735460	2.42[-9]
$10c \ ^1D^e$	0.503881002	2.13[-7]	$15a \ ^1P^o$	0.502471231	2.11[-8]	$19b \ ^1S^e$	0.501549984	7.48[-9]
$11a \ ^1S^e$	0.504900134	4.34[-7]	$15a \ ^1D^e$	0.502500999	1.55[-8]	$19b \ ^1P^o$	0.501799184	4.02[-7]
$11a \ ^1P^o$	0.504477811	2.88[-7]	$15b \ ^1S^e$	0.502304622	1.01[-8]	$19b \ ^1D^e$	0.501633447	9.01[-9]
$11a \ ^1D^e$	0.504562020	7.22[-8]	$15b \ ^1P^o$	0.502688181	3.28[-6]	$19c \ ^1P^o$	0.500860255	7.84[-8]
$11b \ ^1S^e$	0.504119513	8.50[-8]	$15b \ ^1D^e$	0.502491120	9.77[-8]	$19c \ ^1D^e$	0.500544645	7.36[-8]
$11b \ ^1P^o$	0.504976353	3.63[-6]	$15c \ ^1P^o$	0.501600912	8.41[-7]	$20a \ ^1S^e$	0.501599589	3.87[-8]
$11b \ ^1D^e$	0.504383822	2.38[-7]	$15c \ ^1D^e$	0.501005710	8.17[-8]	$20a \ ^1P^o$	0.501439183	3.06[-9]
$11c \ ^1P^o$	0.503546267	9.30[-6]	$16a \ ^1S^e$	0.502304627	7.03[-8]	$20a \ ^1D^e$	0.500419308	7.22[-8]
$11c \ ^1D^e$	0.503338182	1.83[-7]	$16a \ ^1P^o$	0.502297223	1.88[-8]	$20b \ ^1S^e$	0.501423276	6.41[-9]
$12a \ ^1S^e$	0.504102114	3.22[-7]	$16a \ ^1D^e$	0.502309254	9.89[-9]	$20b \ ^1P^o$	0.501540484	2.24[-7]
$12a \ ^1P^o$	0.503750991	1.00[-7]	$16b \ ^1S^e$	0.502100382	1.00[-8]	$20b \ ^1D^e$	0.501511179	6.92[-9]
$12a \ ^1D^e$	0.503845571	5.35[-8]	$16b \ ^1P^o$	0.502344174	1.05[-6]	$20c \ ^1P^o$	0.500755592	7.66[-8]
$12b \ ^1S^e$	0.503688876	8.10[-8]	$16b \ ^1D^e$	0.502256425	6.83[-8]	$20c \ ^1D^e$	0.500431213	7.07[-8]

Chapter 5

Ab Initio 6D Treatment of the Time-Evolution Dynamics for Two-Electron Systems in Few-Cycle XUV Laser Pulses

5.1 Introduction

Recent experimental progress in the generation of ultrashort xuv laser pulses has made possible exploration of completely breakup problems of atoms and molecules in a smaller time scale [50, 2, 72]. Using the xuv pulse in the time level of sub-attosecond (as) allows us to peer into the exciting processes related to atomic inner-shell spectroscopy. Complete photon-induced breakup problem of many-electron atoms presents great challenges not found in single ionization process to theorists.

It is worthwhile to mention the recent theoretical effects to refine *ab initio* approaches to achieve the accurate and reliable results of the multiphoton, single, and

double ionization of two-electron systems. Understanding the role of the correlation effect in the $(\gamma, 2e)$ and $(2\gamma, 2e)$ process is the key to describing the helium ionization mechanism. For the $(\gamma, 2e)$ reaction, in the conventional independent-particle approaches, only one electron is allowed to absorb a dose of the single photon energy. To depict the dynamics behind the photoionization by absorbing a single photon, we need to describe the process in a fully correlated picture at the outset. In addition to the initial ground state, the correlation effect also enters into play for the final double continuum states. As a consequence, the whole process shows a typical strongly correlated characteristic and requires more comprehensive account for the correlation effect. This sets up an obstacle to explain the experimental observations from an *ab initio* point of view. Also, due to the short time duration of the xuv pulses, the detailed theoretical description for this ionization process requires us to develop a fully *ab initio* time-dependent approach. Describing the system in asymptotic region in terms of the hyperspherical coordinates partially stimulates us to develop a fully correlated hyperspherical coordinates (HSC) approach to deal with the photon-induced photoionization in xuv pulses. In this picture, the two electrons are treated on equal footing either for the ground state and also the double continuum state. Here it is interesting to point out that other approaches either the time-independent or time-dependent theory, are limited in the so-called "weak field" approximation. Neglecting the coupling with other manifolds, only the scattering state with the $^1P^o$ symmetry

is retained in the "weak field" approximation for other approaches. Here we have developed the whole configuration space spanned by the spherical radius r_1 and r_2 is discretized on the non-uniform spaced two-dimensional (2D) mesh.

In this work, we will develop a time-dependent generalized pseudospectral (TDGPS) representation of the hyperspherical coordinates (HSC) technique, in which the physics in the multiphoton, single and double photoionization can be effectively recaptured. In the present work, the dynamics processes of the system under consideration will be described in the hyperspherical coordinates system defined by the hyperradius

$$R = \sqrt{r_1^2 + r_2^2} \quad (5.1.1)$$

and hyperangle

$$\alpha = \tan^{-1}(r_2/r_1). \quad (5.1.2)$$

The radial correlation is depicted by the hyperangle variable, while the angular correlation is described by the coupled spherical harmonic functions. In the conventional hyperspherical coordinates theory, the concept of adiabatic eigenchannel plays a commanding role on the description of the three-body correlated Coulomb problems. More recently, we have developed its time-dependent version in energy representation to explore the fine-structure in the emitted spectrum of high-harmonics generation of the laser-driven helium atom [26]. However, as we noted, only limited numbers of the adiabatic eigenchannels, which are converging to the different He^+ ionization thresholds, can be incorporated in a practical calculation. Without combining other

techniques, this limits us from handling the higher energy regime ($E \geq 0$) in which the double photoionization takes place. This indicates that the double photoionization of two-electron systems in hyperspherical coordinates can be coped only if the new idea is introduced.

Mapping technique we have used for the HHG calculations [26] is also applicable for the present photoionization processes in the Coulomb potential, in which most of the dynamics processes dominates in the near nuclear region rather than the region far from the nucleus. The former region can be effectively addressed by imposing a denser grid distribution in the numerical calculations. The denser mesh near the nuclear region provides a proper representation for the photoionization process, even for the multiphoton ionization process. As one of the appealing features, the present strategy allows to employ only the smaller numbers of mesh to discretize the configuration space. This leads the practical calculates more manageable.

5.2 Generalized Pseudospectral Method in Hyperspherical Coordinates

In the conventional hyperspherical coordinates theory, the concept of the adiabatic eigenchannel plays a commanding role on the description of the three-body correlated Coulomb problems. More recently, we have developed its time-dependent version in

energy representation to explore the fine-structure in the emitted spectrum of high-harmonic generation of the laser-driven helium atom [26]. However, as we noted, only limited numbers of the adiabatic eigenchannels, which are converging to the different He^+ ionization thresholds, can be incorporated in a practical calculation. Without combining other techniques, this limits us from handling the higher energy regime ($E \geq 0$) in which the double photoionization takes place. This indicates that the double photoionization of the helium atom in hyperspherical coordinates can be coped only if the new idea is introduced.

Some clues to overpass the above difficulty can be gleaned by recasting conventional wave function in hyperspherical coordinates. After mapping the hyperradius and hyperangle into the working space through $R = R(x)$ and $\alpha = \alpha(y)$, the wave function is not a function of the adiabatic channels. Because no adiabatic channels are referred in the practical calculations, it allows us to effectively consider the physics in the higher energy region, for example $E \geq 0$.

We map the hyperradius R in a finite box $[0, R_{max}]$ into the domain $[-1, 1]$ by

$$R(x) = L \frac{1+x}{1-x+\gamma}, \quad -1 \leq x \leq 1, \quad (5.2.1)$$

where $\gamma = 2L/R_{max}$, and hyperangle α in a finite angle $[0, \pi/2]$ into the domain $[-1, 1]$ by

$$\alpha(y) = \frac{\pi}{4}(1+y), \quad -1 \leq y \leq 1. \quad (5.2.2)$$

Mapping technique we have used for the HHG calculations [26] is also applicable for the present double photoionization process in the Coulomb potential, in which most of the dynamics processes dominates in the near nuclear region rather than the region far from the nucleus. The former region can be affectively addressed by imposing a denser grid distribution in the numerical calculations. The denser mesh near the nuclear region provides a proper representation for the photoionization process, even for multiphoton ionization process. As one of the appealing features, the present strategy allows to employ only the smaller numbers of mesh to discretize the configuration space. This leads the practical calculations more manageable.

In the HSC formulism, the Schrödinger equation of the helium atom in field-free case can be written as

$$\left[-\frac{1}{2} \frac{\partial^2}{\partial R^2} - \frac{1}{8R^2} + \frac{1}{2R^2} \left(-\frac{\partial^2}{\partial \alpha^2} + \frac{\hat{l}_1^2}{\cos^2 \alpha} + \frac{\hat{l}_2^2}{\sin^2 \alpha} \right) + \frac{1}{R} \left(-\frac{Z}{\cos \alpha} - \frac{Z}{\sin \alpha} + \frac{1}{\sqrt{1 - \sin(2\alpha) \cos \theta_{12}}} \right) \right] \tilde{\Phi}(R, \alpha, \Omega_1, \Omega_2) = E \tilde{\Phi}(R, \alpha, \Omega_1, \Omega_2), \quad (5.2.3)$$

where here the wave function is (physical space to model space) $\tilde{\Phi}(R, \alpha, \Omega_1, \Omega_2) = \sqrt{R'(x)} \Phi(x, y, \Omega_1, \Omega_2)$. Inserting the following equations (physical to model space) into Eq. (5.2.3):

$$\frac{\partial}{\partial \alpha} = \frac{\partial}{\partial y} \frac{\partial y}{\partial \alpha} = \frac{4}{\pi} \frac{\partial}{\partial y}, \quad (5.2.4)$$

$$\frac{\partial^2}{\partial \alpha^2} = \frac{16}{\pi^2} \frac{\partial^2}{\partial y^2}. \quad (5.2.5)$$

Changing Eq. (5.2.3) from physical space $(R, \alpha, \Omega_1, \Omega_2)$ to model space $(x, y, \Omega_1, \Omega_2)$

we have the following form:

$$\begin{aligned} & \left[-\frac{1}{2} \frac{1}{R'(x)} \sqrt{R'(x)} \frac{\partial^2}{\partial x^2} + \frac{15\sqrt{R'(x)}}{8R^2(x)} + \frac{2R'(x)R'''(x) - 3R''(x)R''(x)}{4R'(x)\sqrt{R'(x)}} \right] \Phi(x, y, \Omega_1, \Omega_2) \\ & + \sqrt{R'(x)} \left[\frac{1}{2R^2(x)} \left(-\frac{\partial^2}{\partial \alpha(y)^2} + \frac{\hat{l}_1^2}{\cos^2 \alpha(y)} + \frac{\hat{l}_2^2}{\sin^2 \alpha(y)} \right) \right. \\ & \left. + \frac{1}{R(x)} \left(-\frac{Z}{\cos \alpha(y)} - \frac{Z}{\sin \alpha(y)} + \frac{1}{\sqrt{1 - \sin(2\alpha(y)) \cos \theta_{12}}} \right) \right] \Phi(x, y, \Omega_1, \Omega_2) \\ & = E \sqrt{R'(x)} \Phi(x, y, \Omega_1, \Omega_2). \end{aligned} \quad (5.2.6)$$

The hyperradial derivative term $2R'(x)R'''(x) - 3R''(x)R''(x) = 0$. Then we insert

the hyperangle part of the second derivative which leads to the form:

$$\begin{aligned} & \left[-\frac{1}{2} \frac{1}{R'^2(x)} \frac{\partial^2}{\partial x^2} - \frac{1}{8R^2(x)} + \frac{1}{2R^2(x)} \left(-\frac{16}{\pi^2} \frac{\partial^2}{\partial y^2} + \frac{\hat{l}_1^2}{\cos^2 \alpha(y)} + \frac{\hat{l}_2^2}{\sin^2 \alpha(y)} \right) \right. \\ & \left. + \frac{1}{R(x)} \left(-\frac{Z}{\cos \alpha(y)} - \frac{Z}{\sin \alpha(y)} + \frac{1}{\sqrt{1 - \sin(2\alpha(y)) \cos \theta_{12}}} \right) \right] \Phi(x, y, \Omega_1, \Omega_2) \quad (5.2.7) \\ & = E \Phi(x, y, \Omega_1, \Omega_2). \end{aligned}$$

After the projection out of the spherical harmonics $\mathcal{Y}_{l_1, m_1}(\Omega_1) \mathcal{Y}_{l_2, m_2}(\Omega_2)$, in the model space spanned by $(x, y, \Omega_1, \Omega_2)$, the total wave function takes the form

$$\Phi(x, y, \Omega_1, \Omega_2) = \sum_{l_1 l_2} \sum_i \sum_k f_i(x) f_k(y) F_{l_1 l_2}^{ik, N}(x, y) \mathcal{Y}_{l_1, m_1}(\Omega_1) \mathcal{Y}_{l_2, m_2}(\Omega_2), \quad (5.2.8)$$

and the Schrödinger equation in terms of the hyperspherical variables takes the form

$$\begin{aligned}
& \left[-\frac{1}{2} \frac{1}{R'^2(x)} \frac{\partial^2}{\partial x^2} - \frac{1}{8R^2(x)} + \frac{1}{2R^2(x)} \left(-\frac{16}{\pi^2} \frac{\partial^2}{\partial y^2} + \frac{\hat{l}_1^2}{\cos^2 \alpha(y)} + \frac{\hat{l}_2^2}{\sin^2 \alpha(y)} \right) \right. \\
& \left. + \frac{1}{R(x)} \left(-\frac{Z}{\cos \alpha(y)} - \frac{Z}{\sin \alpha(y)} + \frac{1}{\sqrt{1 - \sin(2\alpha(y)) \cos \theta_{12}}} \right) \right] \\
& \times \left[\sum_{l'_1 l'_2} \sum_{i' k'} f_{i'}(x) f_{k'}(y) F_{l'_1 l'_2}^{i' k', N'} \mathcal{Y}_{l_1, m_1}(\Omega_1) \mathcal{Y}_{l_2, m_2}(\Omega_2) \right] \\
& = E \left[\sum_{l'_1 l'_2} \sum_{i' k'} f_{i'}(x) f_{k'}(y) F_{l'_1 l'_2}^{i' k', N'} \mathcal{Y}_{l_1, m_1}(\Omega_1) \mathcal{Y}_{l_2, m_2}(\Omega_2) \right].
\end{aligned} \tag{5.2.9}$$

The discretized Schrödinger equation in terms of the hyperspherical variables takes

the form

$$\begin{aligned}
& \sum_{l'_1 l'_2} \sum_{i' k'} \left[-\frac{1}{2R'^2(x_i)} \mathcal{K}_{ii'}^x \delta_{kk'} \mathcal{O}_{l_1 l_2}^{l'_1 l'_2} F_{l'_1 l'_2}^{i' k', N'} - \frac{1}{8R^2(x_i)} \delta_{ii'} \delta_{kk'} \mathcal{O}_{l_1 l_2}^{l'_1 l'_2} F_{l'_1 l'_2}^{i' k', N'} \right. \\
& - \frac{8}{\pi^2 R^2(x_i)} \delta_{ii'} K_{kk'}^y \mathcal{O}_{l_1 l_2}^{l'_1 l'_2} F_{l'_1 l'_2}^{i' k', N'} + \frac{1}{2R^2(x_i)} \frac{\hat{l}_1^2}{\cos^2 \alpha(y_k)} \delta_{ii'} \delta_{kk'} \mathcal{O}_{l_1 l_2}^{l'_1 l'_2} (1) F_{l'_1 l'_2}^{i' k', N'} \\
& + \frac{1}{2R^2(x_i)} \frac{\hat{l}_1^2}{\sin^2 \alpha(y_k)} \delta_{ii'} \delta_{kk'} \mathcal{O}_{l_1 l_2}^{l'_1 l'_2} (2) F_{l'_1 l'_2}^{i' k', N'} + \frac{1}{R(x_i)} \left(-\frac{Z}{\cos \alpha(y_k)} - \frac{Z}{\sin \alpha(y_k)} \right) \\
& \times \delta_{ii'} \delta_{kk'} \mathcal{O}_{l_1 l_2}^{l'_1 l'_2} F_{l'_1 l'_2}^{i' k', N'} + \frac{1}{R(x_i)} \delta_{ii'} \delta_{kk'} \\
& \times \left\langle \mathcal{Y}_{l_1, m_1}(\Omega_1) \mathcal{Y}_{l_2, m_2}(\Omega_2) \left| \frac{1}{\sqrt{1 - \sin(2\alpha(y_k)) \cos \theta_{12}}} \right| \right. \\
& \left. \times \mathcal{Y}_{l'_1, m'_1}(\Omega_1) \mathcal{Y}_{l'_2, m'_2}(\Omega_2) \right\rangle F_{l'_1 l'_2}^{i' k', N'} \Big] = E \left[\sum_{l'_1 l'_2} \sum_{i' k'} \delta_{ii'} \delta_{kk'} \mathcal{O}_{l_1 l_2}^{l'_1 l'_2} F_{l'_1 l'_2}^{i' k', N'} \right],
\end{aligned} \tag{5.2.10}$$

where the matrix element of the kinetic energy, $K_{ii'}^x$, in the hyperradius direction and

$K_{kk'}^y$, in the hyperangular direction is defined by

$$K_{ii'}^x = \frac{\partial^2 f_{i'}(x)}{\partial x^2} \Big|_{x=x_i}, \quad (5.2.11)$$

$$K_{kk'}^y = \frac{\partial^2 f_{k'}(y)}{\partial y^2} \Big|_{y=y_k}. \quad (5.2.12)$$

Here, $\mathcal{O}_{l_1 l_2}^{l'_1 l'_2} = \langle \mathcal{Y}_{l_1, m_1}(\Omega_1) | \mathcal{Y}_{l'_1, m'_1}(\Omega_1) \rangle \langle \mathcal{Y}_{l_2, m_2}(\Omega_2) | \mathcal{Y}_{l'_2, m'_2}(\Omega_2) \rangle = \delta_{l_1 l'_1} \delta_{l_2 l'_2} \delta_{m_1 m'_1} \delta_{m_2 m'_2}$ is the overlap matrix. Throughout the angular momentum M is conserved $M = 0$, so therefore we can exclude all angular momentum quantum number M . In Eq. (5.2.9), we define the angular integrals as follows

$$\ominus_{l_1 l_2}^{l'_1 l'_2}(1) = \left\langle \mathcal{Y}_{l_1, m_1}(\Omega_1) \mathcal{Y}_{l_2, m_2}(\Omega_2) \left| \hat{l}_1^2 \right| \mathcal{Y}_{l'_1, m'_1}(\Omega_1) \mathcal{Y}_{l'_2, m'_2}(\Omega_2) \right\rangle = l'_1(l'_1 + 1) \delta_{l_2 l'_2} \delta_{l_1 l'_1} \quad (5.2.13)$$

$$\ominus_{l_1 l_2}^{l'_1 l'_2}(2) = \left\langle \mathcal{Y}_{l_1, m_1}(\Omega_1) \mathcal{Y}_{l_2, m_2}(\Omega_2) \left| \hat{l}_2^2 \right| \mathcal{Y}_{l'_1, m'_1}(\Omega_1) \mathcal{Y}_{l'_2, m'_2}(\Omega_2) \right\rangle = l'_2(l'_2 + 1) \delta_{l_1 l'_1} \delta_{l_2 l'_2}. \quad (5.2.14)$$

The separation of the total Hamiltonian, $H_{l_1 l_2 ik}^{l'_1 l'_2 i' k'}$, into the kinetic energy, $T_{l_1 l_2 ik}^{l'_1 l'_2 i' k'}$, and the potential energy, $V_{l_1 l_2 ik}^{l'_1 l'_2 i' k'}$, matrices takes the form

$$T_{l_1 l_2 ik}^{l'_1 l'_2 i' k'} = -\frac{1}{2R'^2(x_i)} \mathcal{K}_{ii'}^x \delta_{kk'} - \frac{1}{8R^2(x_i)} \delta_{ii'} K_{kk'}^y \delta_{l_1 l'_1} \delta_{l_2 l'_2}, \quad (5.2.15)$$

and

$$\begin{aligned}
V_{l_1 l_2 i k}^{l'_1 l'_2 i' k'} = & -\frac{1}{8R^2(x_i)} \delta_{ii'} \delta_{kk'} \delta_{l_1 l'_1} \delta_{l_2 l'_2} + \frac{1}{2R^2(x_i)} \frac{l_1(l_1+1)}{\cos^2 \alpha(y_k)} \delta_{ii'} \delta_{kk'} \delta_{l_1 l'_1} \delta_{l_2 l'_2} \\
& + \frac{1}{2R^2(x_i)} \frac{l_2(l_2+1)}{\sin^2 \alpha(y_k)} \delta_{ii'} \delta_{kk'} \delta_{l_1 l'_1} \delta_{l_2 l'_2} + \frac{1}{R(x_i)} \left(-\frac{Z}{\cos \alpha(y_k)} - \frac{Z}{\sin \alpha(y_k)} \right) \\
& \times \delta_{ii'} \delta_{kk'} \delta_{l_1 l'_1} \delta_{l_2 l'_2} + \delta_{ii'} \delta_{kk'} \sum_{l=0}^{\infty} \frac{r_{<}^l(y_k)}{r_{>}^{l+1}(y_k)} L_{l_1 l_2}^{l'_1 l'_2}(l),
\end{aligned} \tag{5.2.16}$$

where the angular quantity $L_{l_1 l_2}^{l'_1 l'_2}(l)$ is given in terms of the angles of the vectors \mathbf{r}_1 , and \mathbf{r}_2 by the spherical harmonic addition theorem:

$$\begin{aligned}
L_{l_1 l_2}^{l'_1 l'_2}(l) = & \left\langle \mathcal{Y}_{l_1, m_1}(\Omega_1) \mathcal{Y}_{l_2, m_2}(\Omega_2) \left| \sum_{m=-l}^l \frac{4\pi}{2l+1} \mathcal{Y}_{l, m}^* \mathcal{Y}_{l, m} \right| \mathcal{Y}_{l'_1, m'_1}(\Omega_1) \mathcal{Y}_{l'_2, m'_2}(\Omega_2) \right\rangle \\
= & \sum_{m=-l}^l \frac{4\pi}{2l+1} \sqrt{\frac{(2l_1+1)(2l+1)(2l'_1+1)}{4\pi}} \sqrt{\frac{(2l_2+1)(2l+1)(2l'_2+1)}{4\pi}} \\
& \times \begin{pmatrix} l_1 & l & l'_1 \\ 0 & 0 & 0 \end{pmatrix} \begin{pmatrix} l_1 & l & l'_1 \\ 0 & -m & 0 \end{pmatrix} \begin{pmatrix} l_2 & l & l'_2 \\ 0 & 0 & 0 \end{pmatrix} \begin{pmatrix} l_2 & l & l'_2 \\ 0 & m & 0 \end{pmatrix}.
\end{aligned} \tag{5.2.17}$$

The discretized second derivatives in x , and y for the hyperradius and hyperangle for the Gauss-Lobatto quadrature is defined by:

$$K_{ii'}^x = \frac{\partial^2 f_{i'}(x)}{\partial x^2} \Big|_{x=x_i} = \begin{cases} i = i'; & \frac{N(N+1)}{3(x_i^2-1)} \\ i \neq i'; & (-2) \frac{(-1)^{i+1}}{(x_i-x_{i'})^2} \sqrt{\omega_{i'}/\omega_i} \end{cases}, \tag{5.2.18}$$

$$K_{jj'}^y = \frac{\partial^2 f_{j'}(y)}{\partial y^2} \Big|_{y=y_j} = \begin{cases} j = j'; & \frac{N(N+1)}{3(y_j^2-1)} \\ j \neq j'; & (-2) \frac{(-1)^{j+1}}{(y_j-y_{j'})^2} \sqrt{\omega_{j'}/\omega_j} \end{cases}. \tag{5.2.19}$$

Another advantage of the present GPS technique is that it does not require to calculate the complicated and time-consuming matrix elements of the Coulomb repulsion

interaction, since only the values of the Coulomb potentials in the spatial mesh are needed. Furthermore both the hyperradius R and hyperangle α are discretized in an optimal and nonuniform fashion, namely, more grid points are placed nearby the nucleus and sparser grid structure outward, with the use of only a modest number of grid points. This speeds up considerably the numerical calculation and at the same time provides an accurate wave function at the grid points.

Once the total wave function is obtained we can use this to determine the radial expectation values $\langle r \rangle$, for the bound states of helium:

$$\langle \Psi(\mathbf{r}_1, \mathbf{r}_2) | 1/2(r_1 + r_2) | \Psi(\mathbf{r}_1, \mathbf{r}_2) \rangle . \quad (5.2.20)$$

In Hyperspherical coordinates, Eq. (5.2.20) is recasted into the following form:

$$\begin{aligned} & \langle \Psi(R, \alpha, \Omega_1, \Omega_2) | 1/2(R \cos \alpha + R \sin \alpha) | \Psi(R, \alpha, \Omega_1, \Omega_2) \rangle \\ &= \sum_{ik} \sum_{l_1 l_2} F_{l_1 l_2}^{ik}(x, y) \cdot 1/2(R(x_i) \cos \alpha(y_k) + R(x_i) \sin \alpha(y_k)) \cdot F_{l_1 l_2}^{ik}(x, y). \end{aligned} \quad (5.2.21)$$

The accuracy of the present HSC technique has been demonstrated through comparisons with benchmark energy values of the helium atom. Table 5.1 list the energy of the ground and low-lying states of helium in the field-free case. Only a modest number of grid points, for example $N_R \times N_\alpha = 100 \times 40$, and only a few partial waves ($l_1 = l_2 = 5$), is employed to yield the the results listed in Table 5.1. In most cases, the present results are accurate up to at least six digits, which accuracy are sufficient

to explore the dynamical response of the two-electron atoms in the time-dependent laser pulses.

Table 5.1: Energies of the ground and low-lying excited states of the helium atom. No effect of finite nuclear mass is included in the present and literature values. All energies are given in a.u.

States	This work	Ref. [17]
Singlet state		
1s ² ¹ S ^e	-2.903722	-2.903724
1s2s ¹ S ^e	-2.145974	-2.145974
1s2p ¹ P ^o	-2.123841	-2.123843
1s3s ¹ S ^e	-2.061270	-2.061271
1s3p ¹ P ^o	-2.055145	-2.055146
1s3d ¹ D ^e	-2.055620	-2.055620
1s4d ¹ D ^e	-2.031280	-2.031279
Triplet state		
1s2s ³ S ^e	-2.175229	-2.175229
1s3s ³ S ^e	-2.068693	-2.068698
1s2p ³ P ^o	-2.133163	-2.133164
1s3p ³ P ^o	-2.058080	-2.058081
1s3d ³ D ^e	-2.055636	-2.055636
1s4d ³ D ^e	-2.031285	-2.031288

The oscillator strength of helium is defined in the dipole-length formula as,

$$f_l = 2(E_f - E_i) | \langle \Psi_f(\mathbf{r}_1, \mathbf{r}_2) | z_1 + z_2 | \Psi_i(\mathbf{r}_1, \mathbf{r}_2) \rangle |^2. \quad (5.2.22)$$

In Hyperspherical coordinates, Eq. (5.2.22) is recasted into the following form:

$$f_l = 2(E_f - E_i) | \langle \Psi_f(R, \alpha, \Omega_1, \Omega_2) | R \sin \alpha \cos \theta_1 + R \cos \alpha \cos \theta_2 | \Psi_i(R, \alpha, \Omega_1, \Omega_2) \rangle |^2. \quad (5.2.23)$$

While selected radial distributions and oscillator strengths between low-lying states are listed in Table 5.2. Such an accuracy reported here cannot be achieved by means of commonly used equal-spacing discretization methods without the use of many-orders-of-magnitude larger grid points.

Table 5.2: Comparison of the radial expectation and oscillator strengths of the helium atom. No effect of finite nuclear mass is included. All energies are given in a.u.

States	This work	Ref. [15]
Radial expectation		
1 $^1S^e$	0.929451	0.929452
2 $^1S^e$	2.973276	2.973276
2 $^1P^o$	2.911075	2.911076
3 $^1D^e$	5.615657	5.615658
Oscillator strengths		
$1^1S \rightarrow 2^1P$	0.2721	0.2721
$2^1S \rightarrow 2^1P$	0.3761	0.3761
$2^1P \rightarrow 3^1D$	0.7098	0.7098

5.3 Time-Dependent Generalized Pseudospectral Approach in Hyperspherical Coordinates

Application of hyperspherical coordinates technique to a few-electron atomic systems in the field-free case is far from new, however, its time-dependent version is still under development. Numerical stable and accurate algorithms are required for treatment of the interaction of the atomic system with intense laser fields and the physical quantities of interest can be then extracted from time-dependent wave functions. Having obtained the the eigenstates and in the field-free case, the solution of the time-dependent Schrödinger equation in the linearly polarized laser-driven fields can be expanded in terms of the field-free eigenstates. The time propagation of the wave functions in the laser fields can be obtained by the well-known second-order split-operator technique in *energy* representation.

We generalize the TDGPS techniques to the hyperspherical coordinates for *nonuniform* spatial discretization of the Hamiltonian and for performing the time propagation of the wave function by means second-order split-operator technique in *energy* representation. The time-dependent wave function, namely

$$\Phi(x, y, \Omega_1, \Omega_2, t) = \sum_{l_1 l_2} \sum_i \sum_k f_i(x) f_k(y) F_{l_1 l_2}^{ik, N}(x, y, t) \mathcal{Y}_{l_1, m_1}(\Omega_1) \mathcal{Y}_{l_2, m_2}(\Omega_2). \quad (5.3.1)$$

Equation (5.3.1) is used to propagate the two-electron wave packet in time by the

second-order split-operator technique in the *energy* representation. The time evolution equation

$$\Phi(R, \alpha, \Omega_1, \Omega_2, t + \Delta t) = e^{-iH_0\Delta t/2} e^{-iV(t+\Delta t/2)\Delta t} e^{-iH_0\Delta t/2} \Phi(R, \alpha, \Omega_1, \Omega_2, t) + \mathcal{O}(\Delta t^3), \quad (5.3.2)$$

where H_0 stands for the field-free Hamiltonian and $V(t)$ is the interaction of the helium atom with laser pulses. Here the electric field $\mathbf{E}(t)$ has a \sin^2 envelope function $f(t)$ and is linear polarized along the z axis. In the energy representation, we obtain the so called **S** matrix in hyperspherical space, which indicates the effect of the exponential operator $e^{-iH_0\Delta t/2}$ on the wave function $\Phi(R, \alpha, \Omega_1, \Omega_2, t)$ in Eq. (5.3.2). Here the **S**-matrix elements reads

$$S_{i'k'l'_1l'_2}^{ikl_1l_2}(\Delta t) = \sum_j e^{-i\varepsilon_j\Delta t/2} F_{l_1l_2}^{ik,j}(x, y) F_{l'_1l'_2}^{i'k',j}(x, y), \quad (5.3.3)$$

where ε_N denotes the energy spectra of the helium atom in the field free case. If we choose the initial state $F_{l'_1l'_2}^{i'k'(0)}$ as the ground state of He ($1s^2$) and propagate with the split operator, therefore, the time propagation can be obtained on the mesh through the following three successive time steps

$$\begin{aligned} F_{l_1l_2}^{ik(1)}(x, y, t) &= \sum_{i'k'} \sum_{l'_1l'_2} S_{i'k'l'_1l'_2}^{ikl_1l_2}(\Delta t) F_{l'_1l'_2}^{i'k'(0)}(x, y, t); \\ F_{l'_1l'_2}^{ik(2)}(x, y, t) &= \sum_{l_1l_2} \sum_{l''_1l''_2} \mathcal{Z}_{l_1l_2, l'_1l'_2}^{l''_1l''_2, ik}(x, y, \Delta t) F_{l'_1l'_2}^{ik(1)}(x, y, t); \\ F_{l_1l_2}^{ik(3)}(x, y, t + \Delta t) &= \sum_{i''k''} \sum_{l''_1l''_2} S_{i''k''l''_1l''_2}^{ikl_1l_2}(\Delta t) F_{l''_1l''_2}^{i''k''(2)}(x, y, t). \end{aligned} \quad (5.3.4)$$

For our present case, the \mathbf{Z} matrix caused by the external laser fields is dependent on time, while the \mathbf{S} -matrix is independent of time and only needs to be constructed once. The external laser field propagator matrix \mathbf{Z} , namely

$$\begin{aligned}
Z &= e^{-iV(t+\Delta t/2)\Delta t} = e^{-iE(t+\Delta t/2)\Delta t(z_1+z_2)} = e^{-iE(t+\Delta t/2)\Delta t(R\cos\alpha\cos\theta_1+R\sin\alpha\cos\theta_2)} \\
&= \sum_{l_1 l_2}^{\infty} (2l_1+1)(2l_2+1)(-i)^{l_1+l_2} j_{l_1}(-E(t+\Delta t/2)R\cos\alpha) \\
&\quad \times j_{l_2}(-E(t+\Delta t/2)R\sin\alpha) P_{l_1}(\cos\theta_1) P_{l_2}(\cos\theta_2) \\
&= \sum_{l_1 l_2}^{\infty} (2l_1+1)(2l_2+1)(-i)^{l_1+l_2} j_{l_1}(-E(t+\Delta t/2)R\cos\alpha) \\
&\quad \times j_{l_2}(-E(t+\Delta t/2)R\sin\alpha) \sqrt{\frac{4\pi}{2l_1+1}} \mathcal{Y}_{l_1,0}(\Omega_1) \sqrt{\frac{4\pi}{2l_2+1}} \mathcal{Y}_{l_2,0}(\Omega_2),
\end{aligned} \tag{5.3.5}$$

where j is the spherical bessel functions and P are Legendre polynomials which are expressed as spherical harmonics \mathcal{Y} , hence, $P_l(\cos\theta) = \sqrt{4\pi/(2l+1)} \mathcal{Y}_{l,0}(\theta, \varphi)$. Here, we will explain one time propagation of the wave function by the laser field, namely Eq. (5.3.5) multiplied to the time-dependent wave function defined by

$$\begin{aligned}
& e^{-iE(t+\Delta t/2)\Delta t(R(x)\cos\alpha(y)\cos\theta_1+R(x)\sin\alpha(y)\cos\theta_2)}\Phi(x,y,\Omega_1,\Omega_2) \\
&= \sum_{l_1 l_2}^{\infty} (2l_1+1)(2l_2+1)(-i)^{l_1+l_2} \\
&\times j_{l_1}(-E(t+\Delta t/2)R(x)\cos\alpha(y))j_{l_2}(-E(t+\Delta t/2)R(x)\sin\alpha(y))\sqrt{\frac{4\pi}{2l_1+1}}\mathcal{Y}_{l_1,0}(\Omega_1) \\
&\times \sqrt{\frac{4\pi}{2l_2+1}}\mathcal{Y}_{l_2,0}(\Omega_2)\sum_{l'_1 l'_2}^{\infty} F_{l'_1 l'_2}^{ik}(x,y,t)\mathcal{Y}_{l'_1,m'_1}(\Omega_1)\mathcal{Y}_{l'_2,m'_2}(\Omega_2) \\
&= \sum_{l_1 l_2}^{\infty} \sum_{l'_1 l'_2}^{\infty} (2l_1+1)(2l_2+1)(-i)^{l_1+l_2} j_{l_1}(-E(t+\Delta t/2)R(x)\cos\alpha(y)) \\
&\times j_{l_2}(-E(t+\Delta t/2)R(x)\sin\alpha(y))F_{l'_1 l'_2}^{ik}(x,y,t) \\
&\times \sqrt{\frac{4\pi}{2l_1+1}}\int \mathcal{Y}_{L_1,m_1}^*(\Omega_1)\mathcal{Y}_{l_1,0}(\Omega_1)\mathcal{Y}_{l'_1,m'_1}(\Omega_1)d\Omega_1 \\
&\times \sqrt{\frac{4\pi}{2l_2+1}}\int \mathcal{Y}_{L_2,m_2}^*(\Omega_2)\mathcal{Y}_{l_2,0}(\Omega_2)\mathcal{Y}_{l'_2,m'_2}(\Omega_2)d\Omega_2 \\
&= \sum_{l_1 l_2}^{\infty} \sum_{l'_1 l'_2}^{\infty} (2l_1+1)(2l_2+1)(-i)^{l_1+l_2} j_{l_1}(-E(t+\Delta t/2)R(x)\cos\alpha(y)) \\
&\times j_{l_2}(-E(t+\Delta t/2)R(x)\sin\alpha(y))F_{l'_1 l'_2}^{ik}(x,y,t)\sqrt{\frac{4\pi}{2l_1+1}}\sqrt{\frac{(2L_1+1)(2l_1+1)(2l'_1+1)}{4\pi}} \\
&\times \begin{pmatrix} L_1 & l_1 & l'_1 \\ 0 & 0 & 0 \end{pmatrix} \begin{pmatrix} L_1 & l_1 & l'_1 \\ -m'_1 & 0 & m'_1 \end{pmatrix} \delta_{m_1 m'_1} \sqrt{\frac{4\pi}{2l_2+1}}\sqrt{\frac{(2L_2+1)(2l_2+1)(2l'_2+1)}{4\pi}} \\
&\times \begin{pmatrix} L_2 & l_2 & l'_2 \\ 0 & 0 & 0 \end{pmatrix} \begin{pmatrix} L_2 & l_2 & l'_2 \\ -m'_2 & 0 & m'_2 \end{pmatrix} \delta_{m_2 m'_2}.
\end{aligned} \tag{5.3.6}$$

Based on the equation above we can accurately propagate the time-dependent wave function by the external laser field, which explicitly depends on time. Once the time-dependent wave functions are calculated, we can calculate the time-dependent ionization probability

$$P = 1 - N(t), \quad (5.3.7)$$

where

$$N(t) = \langle \Phi(t) | \Phi(t) \rangle, \quad (5.3.8)$$

and the time-dependent survival probability of the $1s^2$ ground-state orbital

$$S(t) = \langle \Phi_{1s^2}(0) | \Phi(t) \rangle. \quad (5.3.9)$$

Figure 5.1 presents the time-dependent population of the helium atom, as defined in Eq. (5.3.8). The slope of the decay of the electron population in time describes the ionization rate. Figure 5.2 presents the time-dependent survival probability of the helium atoms ground-state orbital ($1s^2$), as defined in Eq. (5.3.9).

Once the time-dependent wave function is obtained the induced dipole moment (Fig. 5.3) and dipole acceleration can now be expressed in hyperspherical coordinates on the mesh, respectfully, as

$$\begin{aligned} d_L(t) &= \left\langle \Phi(t) \left| \sum_{i=1}^2 z_i \right| \Phi(t) \right\rangle \\ &= \langle \Phi(x, y, \Omega_1, \Omega_2, t) | R(x) \cos \alpha(y) \cos \theta_1 + R(x) \cos \alpha(y) \cos \theta_2 | \Phi(x, y, \Omega_1, \Omega_2, t) \rangle \\ &= \sum_{ik} \sum_{l_1 l_2} \sum_{l'_1 l'_2} \left[(R(x_i) \cos \alpha(y_k)) F_{l_1 l_2}^{*ik}(x, y, t) F_{l'_1 l'_2}^{ik}(x, y, t) \right. \\ &\quad \times \langle \mathcal{Y}_{l_1, m_1}(\Omega_1) | \cos \theta_1 | \mathcal{Y}_{l'_1, m'_1}(\Omega_1) \rangle \\ &\quad \left. + (R(x_i) \sin \alpha(y_k)) F_{l_1 l_2}^{*ik}(x, y, t) F_{l'_1 l'_2}^{ik}(x, y, t) \langle \mathcal{Y}_{l_2, m_2}(\Omega_2) | \cos \theta_2 | \mathcal{Y}_{l'_2, m'_2}(\Omega_2) \rangle \right], \end{aligned} \quad (5.3.10)$$

where the angular integration over electron-one, hence, $\cos \theta_1$ is the following

$$\begin{aligned} \langle \mathcal{Y}_{l_1, m_1}(\Omega_1) | \cos \theta_1 | \mathcal{Y}_{l'_1, m'_1}(\Omega_1) \rangle = & \left(\frac{l'_1 + 1}{[(2l'_1 + 1)(2l'_1 + 3)]^{1/2}} \delta_{l_1, l'_1 + 1} \delta_{m_1, m'_1} \right. \\ & \left. + \frac{l'_1}{[(2l'_1 - 1)(2l'_1 + 1)]^{1/2}} \delta_{l_1, l'_1 - 1} \delta_{m_1, m'_1} \right), \end{aligned} \quad (5.3.11)$$

and

$$d_A(t) = \left\langle \Phi(t) \left| \sum_{i=1}^2 \left[-\frac{z_i}{r_i^3} + E_0 f(t) \sin(\omega_0 t) \right] \right| \Phi(t) \right\rangle \quad (5.3.12)$$

where $\nabla_z(1/r) = -z/r^3$, which is the first derivative of the potential with respect to z .

The corresponding HHG power spectrum (Fig. 5.4) can now be obtained by the Fourier transformation of the respective time-dependent dipole moment or dipole acceleration:

$$P_L(\omega) = \left| \frac{1}{t_f - t_i} \int_{t_i}^{t_f} d_L(t) e^{-i\omega t} dt \right|^2 = |d_L(\omega)|^2, \quad (5.3.13)$$

and

$$P_A(\omega) = \left| \frac{1}{t_f - t_i} \frac{1}{\omega^2} \int_{t_i}^{t_f} d_L(t) e^{-i\omega t} dt \right|^2 = |d_A(\omega)|^2. \quad (5.3.14)$$

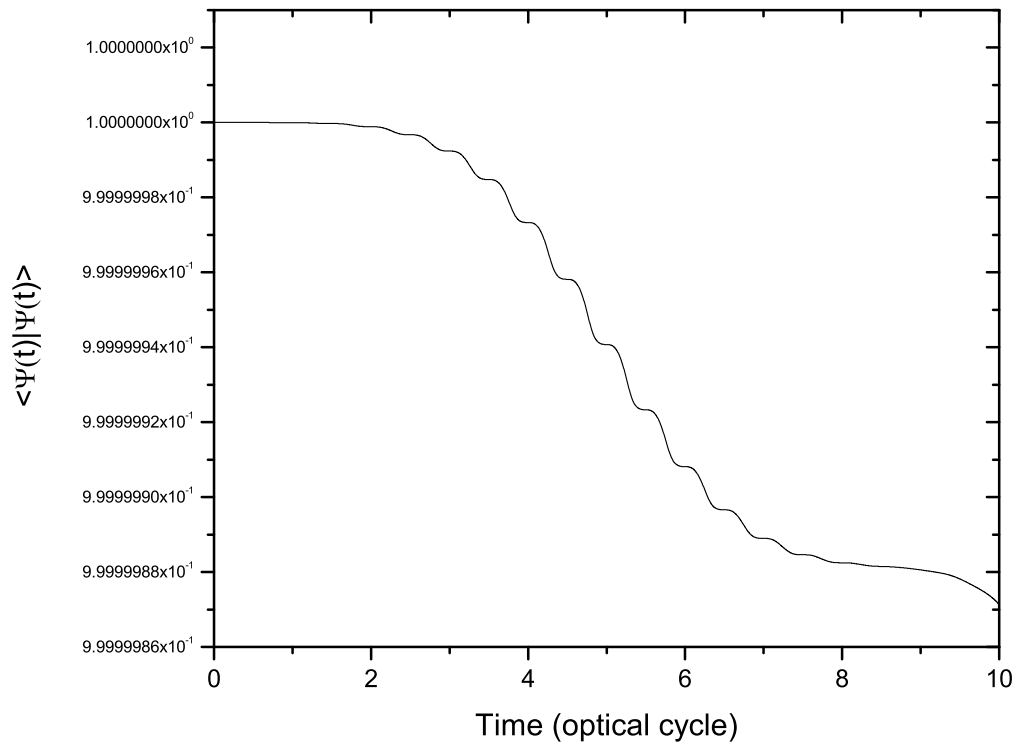


Figure 5.1: The time-dependent population of He in 800 nm, 1×10^{14} W/cm² sin² pulse laser field with 10 optical cycles in pulse duration.

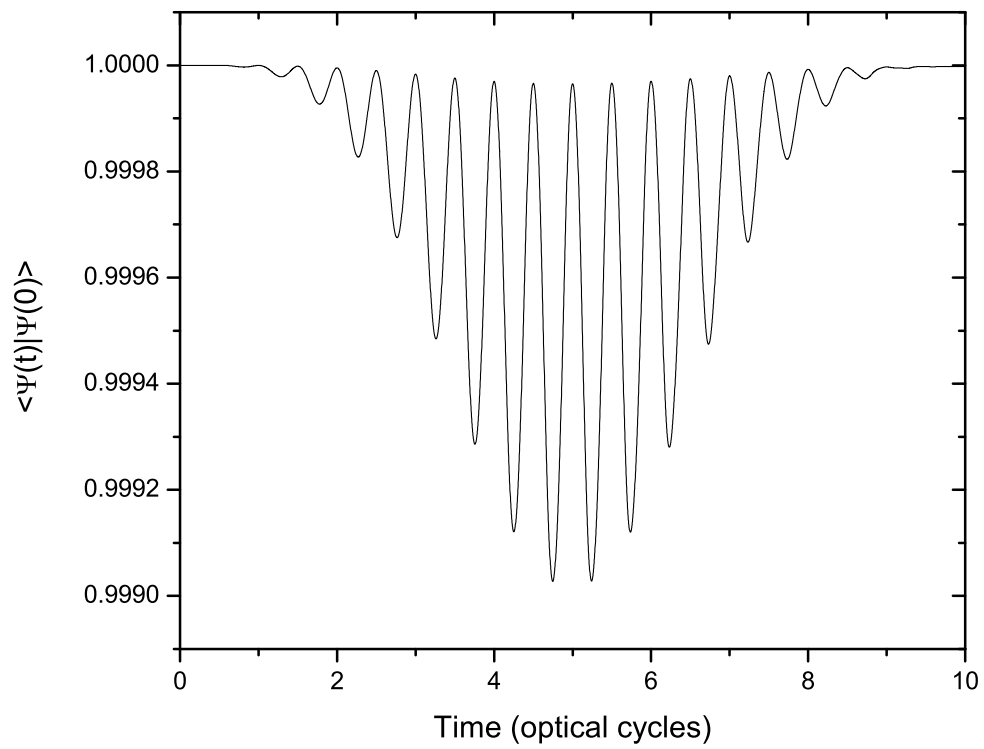


Figure 5.2: The time-dependent survival probability of He (ground-state $1s^2$) in 800 nm, 1×10^{14} W/cm² sin² pulse laser field with 10 optical cycles in pulse duration.

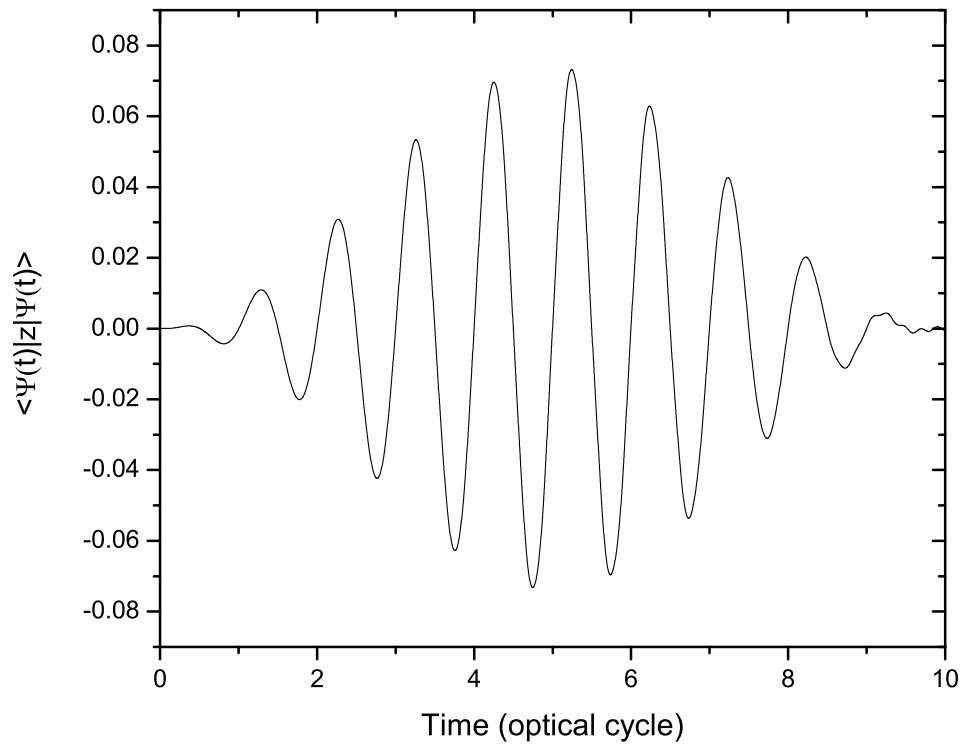


Figure 5.3: The induced dipole moment of He in 800 nm, 1×10^{14} W/cm² sin² pulse laser field with 10 optical cycles in pulse duration.

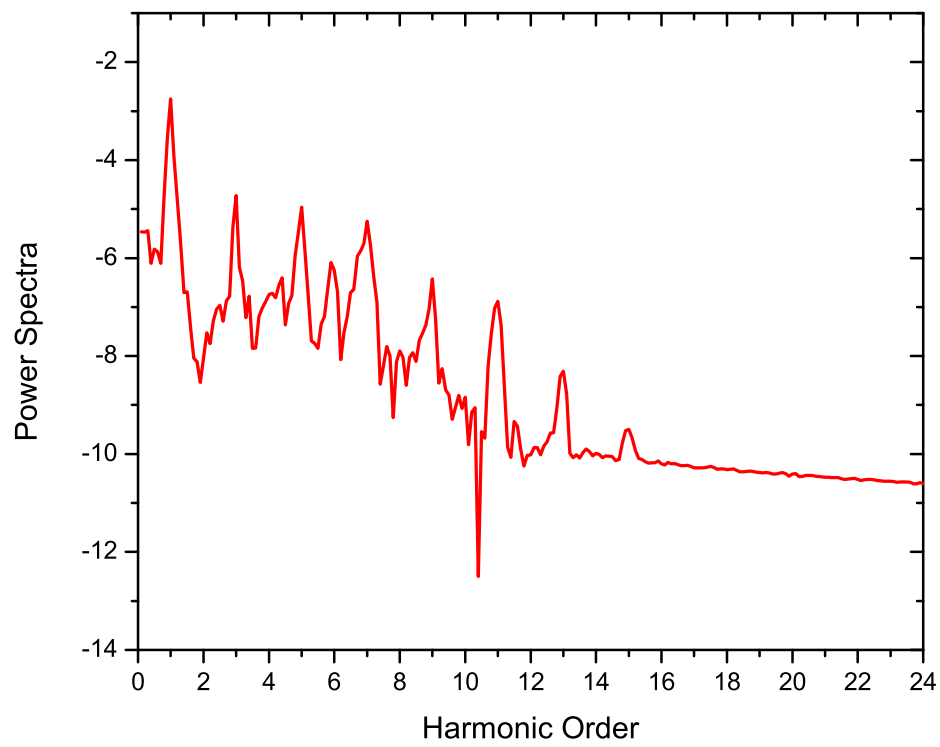


Figure 5.4: Harmonic generation of He in 800 nm, $1 \times 10^{14} \text{ W/cm}^2 \sin^2$ pulse laser field with 10 optical cycles in pulse duration.

5.4 Conclusion

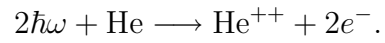
In summary, we have presented a nonperturbative *ab initio* time-dependent hyperspherical coordinates approach for the exploration of the correlated quantum dynamics and the emitted HHG power spectra of the two-electron atomic systems in intense laser pulses. The current TDGPS approach developed in hyperspherical coordinates is shown to be capable of providing accurate time-dependent wave function with only the use of moderate number of grid points. Extension of the present work for the treatment of the doubly ionization process is in progress. This will be based on the competition between the different mechanisms leading to the breakup of the system. The two channels leading to double ionization are open by adsorption of two photons with frequency ($\omega = 57$ eV.). One is sequential

$$\hbar\omega + \text{He} \longrightarrow \text{He}^+ + e^-,$$

and

$$\hbar\omega + \text{He}^+ \longrightarrow \text{He}^{++} + e^-.$$

And another is nonsequential



Regarding the mechanisms leading to double photoionization, there are many aspects which are worthwhile to be explored in detail, since experimental progress in the generation of ultrashort xuv laser pulses has made it possible for exploration of complete breakup problems of atoms and molecules in a smaller time scale.

Bibliography

- [1] A. Baltuška, Th. Udem, M. Uiberacker, M. Hentschel, E. Goulielmakis, Ch. Gohle, R. Holzwarth, V. S. Yakovlev, A. Scrinzi, T. W. Hansch, and F. Krausz, *Nature (London)* **421** (2003), 611.
- [2] T. Brabec and F. Krausz, *Rev. Mod. Phys.* **72** (2000), 545.
- [3] A. Burgers, D. Wintgen, and J. M. Rost, *J. Phys. B* **28** (1995), 3163.
- [4] J. J. Carrera and S. I. Chu, *Phys. Rev. A* **75** (2007), 033807.
- [5] J. J. Carrera and S. I. Chu, *J. Phys. Chem. A* **111** (2007), 9320.
- [6] J. J. Carrera, S. I. Chu, and X. M. Tong, *Phys. Rev. A* **71** (2005), 063813.
- [7] J. J. Carrera, S. K. Son, and S. I. Chu, *Phys. Rev. A* **77** (2008), 031401(R).
- [8] J. J. Carrera, X. M. Tong, and S. I. Chu, *Phys. Rev. A* **74** (2006), 023404.
- [9] S. I. Chu, *J. Chem. Phys.* **123** (2005), 062207.
- [10] X. Chu and S. I. Chu, *Phys. Rev. A* **63** (2001), 023411.
- [11] X. Chu and S. I. Chu, *Phys. Rev. A* **64** (2001), 063404.
- [12] X. Chu and S. I. Chu, *Phys. Rev. A* **63** (2001), 013414.

- [13] X. Chu and S. I. Chu, Phys. Rev. A **70** (2004), 061402.
- [14] K. T. Chung, T. K. Fang, and Y. K. Ho, J. Phys. B **34** (2001), 165.
- [15] B. F. Davis and K. T. Chung, Phys. Rev. A **25** (1982), 1328.
- [16] M. J. DeWitt, E. Wells, and R. R. Jones, Phys. Rev. Lett. **87** (2001), 153001.
- [17] G. W. F. Drake, *Atomic, molecular, and optical physics handbook*, AIP Press, New York, 1996.
- [18] R. M. Dreizler and E. K. U. Gross, *Density functional theory, an approach to quantum many-body problem*, Springer: Berlin, 1990.
- [19] J. M. Rost *et al.*, J. Phys. B **30** (1997), 4663.
- [20] J. R. Harries *et al.*, Phys. Rev. Lett. **90** (2003), 133002.
- [21] K. C. Prince *et al.*, Phys. Rev. Lett. **96** (2006), 093001.
- [22] M. Zitnik *et al.*, Phys. Rev. A **74** (2006), 051404(R).
- [23] O. Marchuk *et al.*, Phys. Rev. Lett. **B37** (2004), 1951.
- [24] T. K. Fang and K. T. Chung, J. Phys. B **34** (2001), 1245.
- [25] Ch. Gohle, Th. Udem, M. Herrmann, J. Rauschenberger, R. Holzwarth, H. A. Schuessler, F. Krausz, and T. W. Hansch, Nature (London) **436** (2005), 234.
- [26] X. Guan, X. M. Tong, and S. I. Chu, Phys. Rev. A **73** (2006).
- [27] H. Hamnett, W. Stoll, and C. E. Brion, J. Electron Spectrosc. Relat. Phenom. **8** (1976), 367.
- [28] M. Hentschel, R. Kienberger, Ch. Spielmann, G. A. Reider, N. Milosevic, T. Brabec, P. Corkum, U. Heinzmann, M. Drescher, and F. Krausz, Nature (London) **414** (2001), 509.

- [29] M. R. Hermann and J. A. Fleck Jr., Phys. Rev. A **38** (1988), 6000.
- [30] J. Heslar, J. J. Carrera, D. A. Telnov, and S. I. Chu, Int. J. Quantum Chem. **107** (2007), 3159.
- [31] P. Hohenberg and W. Kohn, Phys. Rev. **136** (1964), B864.
- [32] T. F. Jiang and S. I. Chu, Phys. Rev. A **46** (1992), 7322.
- [33] G. Johansson, J. Hedman, A. Berndtsson, M. Klasson, and R. Nilsson, J. Electron Spectrosc. Relat. Phenom. **2** (1973), 295.
- [34] R. J. Jones, K. D. Moll, M. J. Thorpe, and J. Ye, Phys. Rev. Lett. **94** (2005), 193201.
- [35] G. L. Kamta, B. Piraux, and A. Scrinzi, Phys. Rev. A **63** (2001), 040502.
- [36] W. Kohn and L. J. Sham, Phys. Rev. **140** (1965), A1133.
- [37] J. L. Krause, K. J. Schafer, and K. C. Kulander, Phys. Rev. A **45** (1992), 4998.
- [38] T. Kreibich, M. Lein, V. Engel, and E. K. U. Gross, Phys. Rev. Lett. **87** (2001), 103901.
- [39] K. Kulander, Ed. Comput. Phys. Commun. **63** (1991), 1.
- [40] M. Leibscher, I. S. Averbukh, and H. Rabitz, Phys. Rev. A **69** (2004), 013402.
- [41] L. Lipsky and M. J. Conneely, Phys. Rev. A **14** (1976), 2193.
- [42] R. P. Madden and K. Codling, Phys. Rev. Lett. **10** (1963), 516.
- [43] A. Mehelic, Ph.D. thesis, Faculty of Mathematics and Physics, University of Ljubljana, <http://www.rcp.ijs.si/amihelic/phd/thesis.pdf>, 2006.
- [44] A. Mehelic and M. Zitnik, Phys. Rev. Lett. **98** (2007), 243002.

- [45] J. Muth-Bohm, A. Becker, and F. H. M. Faisal, Phys. Rev. Lett. **85** (2000), 2280.
- [46] R. D. Nelson Jr., D. R. Lide, and A. A. Maryott, Circ. No. 10, National Standard Reference Data Series Natl. Bur. Stand. (U.S.), US GPO Washington DC, 1967.
- [47] R. G. Parr and W. T. Yang, *Density-functional theory of atoms and molecules*, Oxford University Press, New York, 1989.
- [48] D. Pinkham and R. R. Jones, Phys. Rev. A **72** (2005), 023418.
- [49] D. Pinkham, K. E. Mooney, and R. R. Jones, Phys. Rev. A **75** (2007), 013422.
- [50] P. Salieres, A. L’huillier, P. Antoine, and M. Lewenstein, Adv. At. Mol. Phys. **41** (1999), 83.
- [51] C. Sathe, M. Strom, M. Agaker, J. Soderstrom J. E. Rubensson, R. Richter, M. Alagia, S. Stranges, T.W. Gorczyca, and F. Robicheaux, Phys. Rev. Lett. **96** (2006), 043002.
- [52] P. R. T. Schipper, O. V. Gritsenko, S. J. A. Van Gisbergen, and E. J. J. Baerends, Chem. Phys. **112** (2000), 1344.
- [53] K. Siegbahn, J. Electron Spectrosc. Relat. Phenom. **5** (1974), 3.
- [54] H. Stapelfeldt and T. Seideman, Rev. Mod. Phys. **75** (2003), 543.
- [55] G. Tanner, K. Richter, and J. M. Rost, Rev. Mod. Phys. **72** (2000), 497.
- [56] D. A. Telnov and S. I. Chu, Phys. Rep. **390** (2004), 1.
- [57] D. A. Telnov and S. I. Chu, Phys. Rev. A **71** (2005), 013408.
- [58] D. A. Telnov and S. I. Chu, Phys. Rev. A **76** (2007), 043412.
- [59] O. I. Tolstikhin, S. Watanabe, and M. Matsuzawa, J. Phys. B **29** (1996), L389.

- [60] X. M. Tong and S. I. Chu, Chem. Phys. **217** (1997), 119.
- [61] X. M. Tong and S. I. Chu, Phys. Rev. A **55** (1997), 3406.
- [62] X. M. Tong and S. I. Chu, Phys. Rev. A **57** (1998), 452.
- [63] X. M. Tong and S. I. Chu, Int. J. Quantum Chem. **69** (1998), 293.
- [64] X. M. Tong and S. I. Chu, Phys. Rev. A **61** (2000), 021802(R).
- [65] X. M. Tong and S. I. Chu, Phys. Rev. A **64** (2001), 013417.
- [66] X. M. Tong and C. D. Lin, Phys. Rev. Lett. **92** (2004), 223003.
- [67] X. M. Tong and C. D. Lin, Phys. Rev. A **71** (2005), 033406.
- [68] X. M. Tong, Z. X. Zhao, and C. D. Lin, Phys. Rev. A **66** (2002), 033402.
- [69] D. W. Turner, C. Baker, A. D. Baker, and C. R. Brundle, *Molecular photoelectron spectroscopy*, Wiley-Interscience, London, 1970.
- [70] Th. Udem, R. Holzwarth, and T. W. Hansch, Nature (London) **416** (2002), 233.
- [71] C. A. Ullrich, U. J. Gossmann, and E. K. U. Gross, Phys. Rev. Lett. **74** (1995), 872.
- [72] H. Wabnitz, Nature (London) **420** (2002), 482.
- [73] J. Y. Wang, S. I. Chu, and C. Laughlin, Phys. Rev. A **50** (1994), 3208.
- [74] E. Wells, M. J. DeWitt, and R. R. Jones, Phys. Rev. A **66** (2002), 013409.
- [75] G. Yao and S. I. Chu, Phys. Rev. A **45** (1992), 6735.
- [76] G. Yao and S. I. Chu, Chem. Phys. Lett. **204** (1993), 381.
- [77] M. Zitnik and A. Mihelic, J. Phys. B **39** (2006), L167.